Summer 2017

Probing the Secondary Coordination Sphere of Zn(II) and Fe(II) Pyridinediimine (PDI) Complexes

Mayra Delgado
Western Washington University, dvrgs.mayra@gmail.com

Probing the Secondary Coordination Sphere of Zn(II) and Fe(II) Pyridinediimine (PDI) Complexes

By

Mayra Delgado

Accepted in Partial Completion

of the Requirements for the Degree

Master of Science

Kathleen L. Kitto, Dean of the Graduate School

ADVISORY COMMITTEE

Chair, Dr. John Gilbertson

Dr. Margaret Scheuermann

Dr. David Rider

MASTER'S THESIS

In presenting this thesis in partial fulfillment of the requirements for a master's degree at Western Washington University, I grant to Western Washington University the non-exclusive royalty-free right to archive, reproduce, distribute, and display the thesis in any and all forms, including electronic format, via any digital library mechanisms maintained by WWU.

I represent and warrant this is my original work, and does not infringe or violate the rights of others. I warrant that I have obtained written permissions from the owner of any third party copyrighted material included in these files. I acknowledge that I retain ownership rights to the copyright of this work, including but not limited to the right to use all or part of this work in future works, such as articles or books.

Library users are granted permission for individual, research and non-commercial reproduction of this work for educational purposes only. Any further digital posting of this document requires specific permission from the author.

Any copying or publication of this thesis for commercial purposes, or gain financial need, is not allowed without my written permission.

Mayra Delgado

June 24, 2017

Probing the Secondary Coordination Sphere of Zn(II) and Fe(II) Pyridinediimine (PDI) Complexes

A Thesis

Presented to

The Faculty of

Western Washington University

In Partial Fulfillment

of the Requirements for the Degree

Master of Science

By

Mayra Delgado

June 2017

Abstract

The transformation of many small, abundant molecules is necessary both in a biological setting and in the chemical industry. In Nature, the activation of small molecules is promoted by metalloenzymes. However, many of these chemical transformations are thermodynamically demanding and consist of multi-electron redox processes. Understanding the secondary coordination sphere has played an integral role in determining the catalytic activity and selectivity of such transformations and has led to the development of bioinspired catalysts in order to mimic the native active site of the metalloenzyme. Due to its extensive modularity, the utilization of the pyridinediimine (PDI) metal complexes was targeted in this work to study the secondary coordination sphere and its relationship to the reactivity at the metal active site. The redox-active PDI ligand scaffold containing a pendant base was used to synthesize a series of Fe(II) and Zn(II) complexes consisting of H-bond acceptors/donors in the secondary coordination sphere. The Zn(II) complexes are able to be protonated in the secondary coordination sphere, forming metal halogen hydrogen bonds (MHHBs). The use of these intramolecular H-bonds in the Zn complexes also serve to provide stabilization of the hydrosulfide (HS^-) ligand, forming a six-coordinate Zn complex. The Fe(II) complexes were reduced under CO atmosphere, followed by protonation in the secondary coordination sphere. This resulted in stable, doubly reduced protonated species, capable of moving protons and electrons in and out of the system. The protonated Fe(II) complex was poised to deliver protons and electrons necessary to investigate nitrite (NO_2^-) reduction for the formation a dinitrosyl iron complex (DNIC). The reduction of nitrate (NO_3^-) for the synthesis of the DNIC was also explored and used to further investigate products of the reaction. Fe(II) PDI complexes with an incorporation of Lewis acids in the secondary coordination sphere were also synthesized and characterized in order to provide a better understanding of how redox inactive metals in the secondary coordination sphere of the PDI scaffold of alters the redox activity of the complex.

ACKNOWLEDGMENTS

Research Advisor: Dr. John D. Gilbertson

Thesis Committee Members: Dr. David Rider, Dr. Margaret Scheuermann

Research Group Members: Yubin Kwon, Audrey Cheung, Kyle Burns

Instrument Technicians: Dr. Hla Win-Piazza and Charles Wandler

Mössbauer: Dr. Takele Seda

X-ray Crystallographer: Dr. Lev Zakharov

Financial Support: National Science Foundation

Western Washington University, Department of Chemistry

Table of Contents

List of Figures & Tables

List of Equations

List of Abbreviations

Syngas	synthesis gas
DRM	dry CO_2 reforming of methane
atm	atmosphere
PDI	Pyridinediimine
Å	Angstrom
NBu_4SH	tetrabutlyammonium hydrogen sulfide
NMe_4OH	tetrabutylammonium hydroxide
CH_3CN	Acetonitrile
CV	Cyclic voltammetry
DCM	Dichloromethane
DNIC	Dinitrosyl iron complex
FTIR	Fourier Transform Infrared
MeOH	Methanol
NMR	Nuclear Magnetic Resonance
nm	nanometer
ORTEP	Oak Ridge Thermal Ellipsoid Plot
ppm	Parts-per-million
TEA	Triethylamine
THF	Tetrahydrofuran
UV-Vis	Ultraviolet-Visible
δ	Isomer Shift
ΔE_Q	Quadrupole Splitting

μ_{eff}	Effective magnetic moment
$NaNO_2$	Sodium nitrite
$TBANO_3$	Tetrabutylammonium nitrate

Chapter 1. Introduction

1.1 Small Molecule Activation

The transformation of small molecules into useful chemicals and fuels typically involves relatively unreactive abundant small molecules such as H_2, CO_2, CH_4, NH_3, O_2, NO, N_2O, etc. Several of these chemical transformations play an important role in both physiological and industrial applications.[1-6] Industrially, these molecules are transformed into more usable chemical feedstocks and energy resources, contributing to the renewable energy process.[7-10] For example, the hydrocarbons used for fuels, as well as methanol used as a feedstock, can be catalytically produced from syngas (a mixture of H_2 and CO) via the Fischer-Tropsch synthesis route.[11] The production of syngas can be accomplished from many sources such as dry CO_2 reforming of methane (DRM) (Eq. 1.1), consisting of two greenhouse gases, which makes this an attractive route for the formation of syngas.[12, 13]

$$CO_2 + CH_4 \rightarrow 2CO + 2H_2 \quad \Delta H_{298} = +247 \text{ kJ/mol} \quad (1.1)$$

Similarly, the Haber-Bosch process (Eq. 1. 2) makes use of N_2 and H_2 to produce NH_3, used in fertilizers. This process is especially important due to the major role it plays in contributing to the nitrogen source available for global agriculture.[14]

$$N_2 + 3H_2 \rightarrow 2NH_3 \quad \Delta H_{298} = +247 \text{ kJ/mol}; \Delta G = -33 \text{kJ/mol} \quad (1.2)$$

Unlike the biological transformation of N_2 to ammonia (nitrogen fixation) which occurs under ambient conditions, the Haber-Bosch process proceeds under high temperatures (500 ˚C) and pressures (~200 atm).[15] Among the many small molecule activation processes that are targeted, these two examples provide insight into the industrial aspect of small molecule activation. In both examples provided, a metal catalyst is needed to overcome the large kinetic barrier that these thermodynamically stable transformations have. In nature, metalloenzymes are used to overcome these barriers as they have the capability to mediate an extensive range of chemical transformations.[16]

1.2 Metalloenzymes

As described above, the catalytic transformations of these small, inert molecules into fuels such as CO, methanol, ammonia, or H_2 are important in the chemical industry. In nature these conversions are facilitated by metalloenzymes containing inorganic active sites. The metal ion cofactors in metalloenzyme active sites play a role in catalytic biological reactions, such as electron transfer reactions.[17] Examples of metal cofactors in the active sites (Figure 1.1) illustrate the fundamental need for use of transition metals such as zinc and iron. For example, the zinc dependent metalloenzyme, Carbonic Anhydrase II (CA) (Figure 1.2), is associated with catalyzing the rapid conversion of CO_2 and water to carbonic acid (Eq. 1.3). The very high turnover numbers associated with the carbonic anhydrase catalyzed hydration of carbon dioxide make this one of the most rapid enzyme reactions known, with values up at $10^6\ s^{-1}$.[18,19]

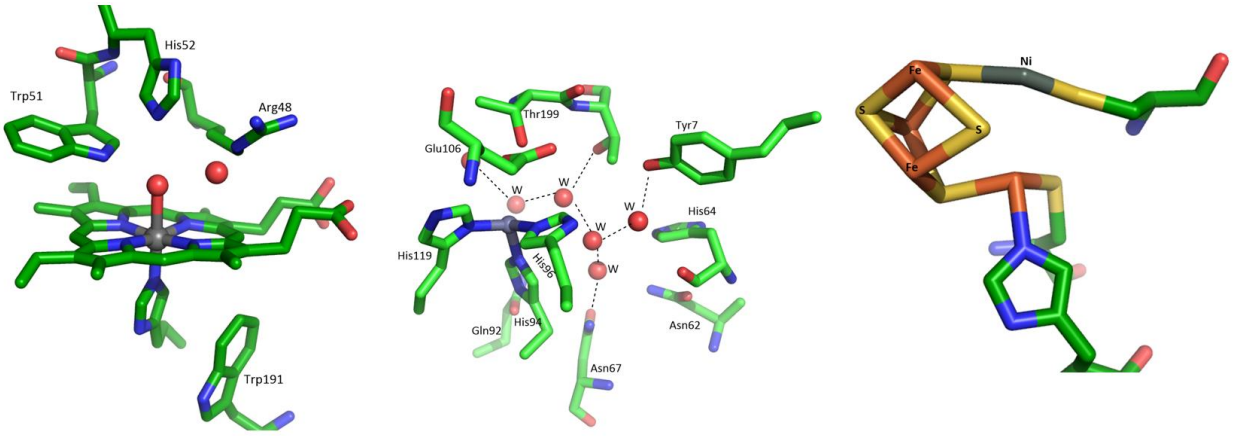

Figure 1.1. Metal cofactors in proteins: iron in cytochrome c peroxidase[20] (left), zinc in carbonic anhydrase[18,19] (middle), and iron in CO dehydrogenase[19] (right). (Figures made in PyMOL).

Metalloenzyme active sites have two main components: the primary coordination sphere and the secondary coordination sphere. The ligands directly bound to the metal ion, such as the amino acid residues, make up the primary coordination sphere. The secondary coordination sphere is composed of groups not directly bound to the metal center, but still within a close proximity to the environment of

the metal cofactor (Figure 1.2). The active site of CA II also illustrates the presence of water molecules in the secondary coordination sphere, which are capable of forming hydrogen bonds that can play a role in modulating proton transfers.[18]

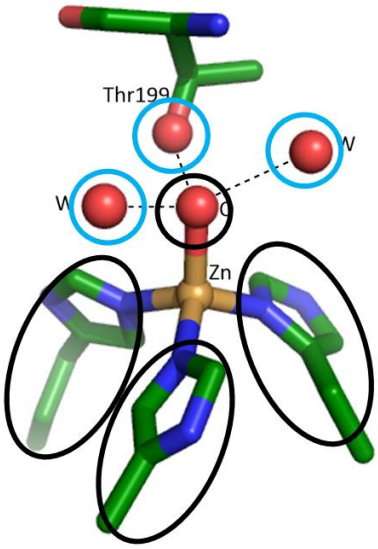

$$CO_2 + H_2O \rightleftharpoons HCO_3^- + H^+ \qquad (1.3)$$

Figure 1.2. Zinc coordination active site of Carbonic Anhydrase II illustrating the primary coordination sphere (black) and the secondary coordination sphere (blue).[21] (Figure made in PyMOL).

Other secondary coordination sphere interactions include hydrogen bond acceptors, and amino acid residues which can participate in controlling the redox properties of the primary sphere as well as aid in the coordination of substrates.[18b] For example, the redox potential of iron-sulfur centers of metalloproteins, have been observed to be affected by hydrogen bonds. It has also been observed that the active site of hemoglobin I is selective for H_2S (Figure 1.3) where the presence of a hydrogen bond donor in heme proteins helps to stabilize bound hydrosulfide (HS^-) ligand.[22] Comparatively, the presence of a hydrogen bond acceptor destabilizes the ferric state in the heme pocket of Hemoglobin I.

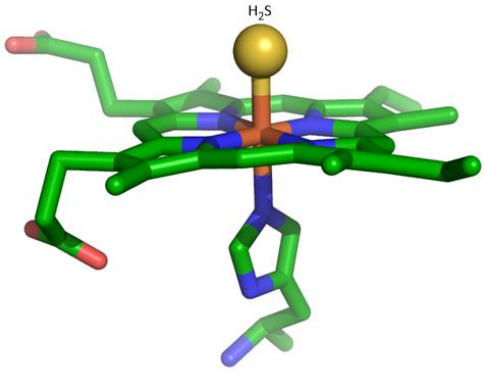

Figure 1.3. Coordination of sulfide to a Fe^{II} heme complex (Figure made in PyMOL).[23]

Other major enzymes participating in key small molecule activation include hydrogenase ($H_2 \leftrightarrow 2H^+ + 2e^-$), alcohol dehydrogenase, carbon monoxide dehydrogenase ($CO_2 + 2e^- + 2H^+ \leftrightarrow CO + H_2O$), nitrogenase, nitrite reductase ($NO_2^- + 2e^- \leftrightarrow NO + H_2O$), and nitrate reductase ($NO_3^- + 3e^- \leftrightarrow NO + H_2O$), among many more. In order to study these significantly important biological systems at the molecular level, model complexes that share features parallel to that of the native enzymes are synthesized and characterized.

1.3 Hydrogen Sulfide

As discussed above, a sulfur-based ligand can be stabilized by the presence of hydrogen bonds in the secondary coordination sphere. For this reason, an area of research that has become of great interest is to explore H_2S complexes. Similar to NO and CO, H_2S has emerged as another gaseotransmitter in the regulatory system.[22b,c, 24] However, H_2S is also seen as an environmental pollutant found from the decomposition of bacterial and organic matters. Inorganic sources of H_2S pollutant are also found in areas such as volcanic sediment, natural gas and sulfur deposits.[25]

Toxicity of H_2S in the body comes from the fact that it can prevent cellular respiration by binding to iron from the mitochondrial cytochrome enzymes. Interaction with heme proteins such as cytochrome c oxidase, hemoglobin, and myoglobin is a common feature observed with H_2S. The H_2S level is balanced by reduction and oxidation of sulfur performed by two types of bacteria.[25] In mammalian cells, H_2S is generated by enzymatic and non-enzymatic pathways. Reverse transsulfuration involves the synthesis of cysteine from methionine using CBS as the catalyzing enzyme. Cystathionine β-synthase (CBS) is the enzyme responsible for catalyzing the condensation of cysteine with homocysteine to form cystathionine and H_2S (Figure 1.4). The second step of reverse transsulfuration is catalyzed by Cystahionine γ-lyase (CSE) (Figure 1.4). CSE is the main H_2S forming enzyme in the kidney, liver and the uterus.

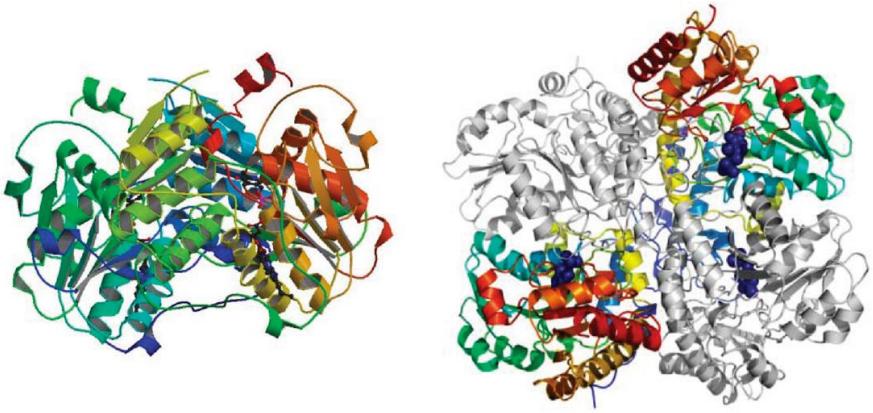

Figure 1.4. Cystathionine β-synthase and Cystahionine γ-lyase (CSE) (Figures made in PyMOL).[25]

Despite its importance, efforts to synthesize metal-based H_2S and HS^- complexes in order to study the physiological reactivity remain sparse. Metal-sulfur interactions are significant in enzymes such as nitrogenases and hydrogenases. H_2S exists in different protonation states at physiological pH. Reactivity with transition metal centers are complicated due to the variation of protonation state affecting the redox potential, nucleophilicity, and tendency to form insoluble metal salts.[22c, 26] Ruthenium and iron based complexes have been reported, but stable Zn hydrosulfido complexes remain rare due to the lack of stability for the labile Zn-SH. In other systems, the hydrosulfide is stabilized and protected by the

sterics offered by the ligand platform. An example of these zinc hydrosulfide complexes is that of the highly encapsulating pyrozolylborate ligand which allows for stabilization of the developed hydrosulfide complex of zinc through its binding pocket (Figure 1.5).[27]

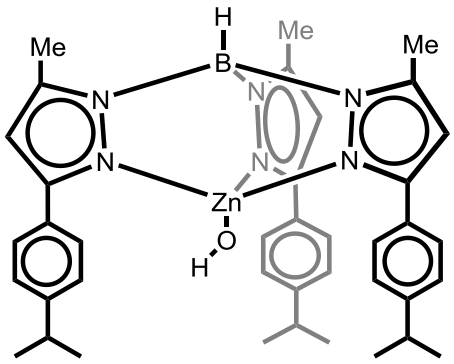

L·Zn-OH

Figure 1.5. Pyrozolylborate ligand illustrating the stability of Zn-OH.

In some iron systems, it has been observed that the metal sulfide species is stabilized by secondary coordination sphere interactions.[29] For example, the active site of hemoglobin (I) in *Lucina pectinata* binds H_2S as seen above in Figure 1.3. In this case, the polarity plays a major role the stability of H_2S bound to the iron center. High polar active sites can stabilize H_2S, while non-polar sites cause a metal-H_2S dissociation. This means that the stereoelectronics of the heme site determine whether the H_2S can stay bound or dissociate from the iron center, illustrating the importance of the secondary coordination sphere.

1.4 Nitrate Reductase

The chemical transformation of nitrate to nitrite is catalyzed biologically by an enzyme called nitrate reductase. This conversion of NO_3^- to NO_2^- plays a vital role in the nitrogen cycle as it is the first step in the denitrification process (Figure 1.6). The nitrogen cycle allows for interconversions of nitrogen compounds, with the help of various enzymes, to yield either ammonia or dinitrogen. The nitrogen

cycle can be broken down into four main components: Nitrogen fixation, Nitrification, Nitrate Assimilation, and Denitrification.[30]

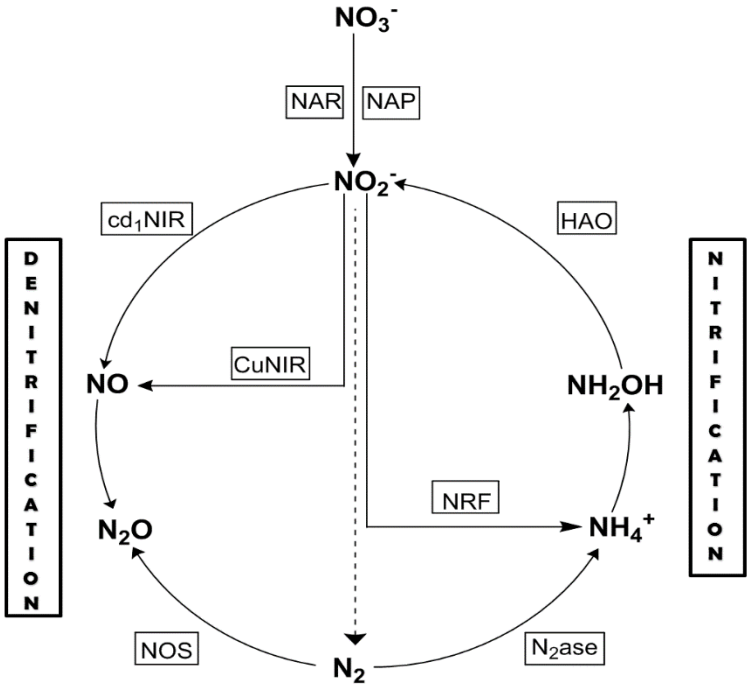

Figure 1.6. The nitrogen cycle displaying the respective enzymes responsible catalyzing each step of the cycle.[30]

Sources of nitrogen typically end up as water pollutants as nitrate and nitrite and must therefore be reduced to a more useful source. The research presented here will focus on the nitrate and nitrite reduction aspect of the nitrogen cycle. Nitrate reductases (NRs) catalyze the reduction of nitrate to nitrite ($NO_3^- + 2H^+ + 2e^- \rightarrow NO_2^- + H_2O$; $E^\circ = 0.420$ V).[31] Nitrate reductases can be categorized as Eukaryotic Nitrate Reductases (Euk-NR), Assimilatory nitrate reductases (Nas), Respiratory Nitrate Reductase (Nar) and Periplasmic Nitrate Reductases (Nap).[32] Each of these enzymes are fundamental nitrate reduction. The majority of nitrate reductases are mononuclear molybdenum enzymes where the molybdenum atom is coordinated by sulfur donors (Figure 1.7).

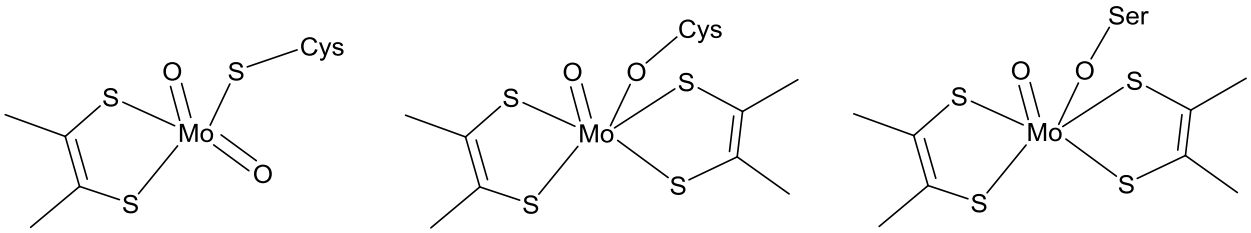

Figure 1.7. Active sites of Nitrate reductases (Euk-NR, periplasmic, and membrane bound)[32b]

Reduction of nitrate to nitrite the first step of denitrification. Denitrification is an important process used by bacteria for energy generation and it plays central role in helping environmental problems such as nitrate accumulation and release of NO in the atmosphere.[32b] The biological process of denitrification consists of the reduction of nitrate (NO_3^-) to nitrogen gas. Intermediate steps involved in denitrification include reduction of nitrate to nitrite followed by further reduction to nitric acid and then to nitrous oxide with a final reduction to dinitrogen. At this stage, N_2 can be further reduced to ammonia (nitrogen fixation) by nitrogenase.

Biologically, organisms use nitrate reductases for reducing nitrate to nitrite in order to generate energy for cellular function, to incorporate nitrogen into biomolecules, and to eliminate energy excess generated by cell metabolism.[30] Nitrate reductases can also be subdivided as either assimilatory or dissimilatory. Direct conversion of nitrate to ammonia can occur via dissimilatory nitrate reduction. The initial reduction of NO_3^- to NO_2^- is achieved by the membrane-bound nitrate reductase.[30] The catalytic nitrate reductase cycle (Figure 1.8) illustrates the five coordinate Mo^{IV} which can coordinate a nitrate ion, followed by the oxidation of Mo^{IV} to Mo^{VI} where NO_2^- is then released.[31, 32a]

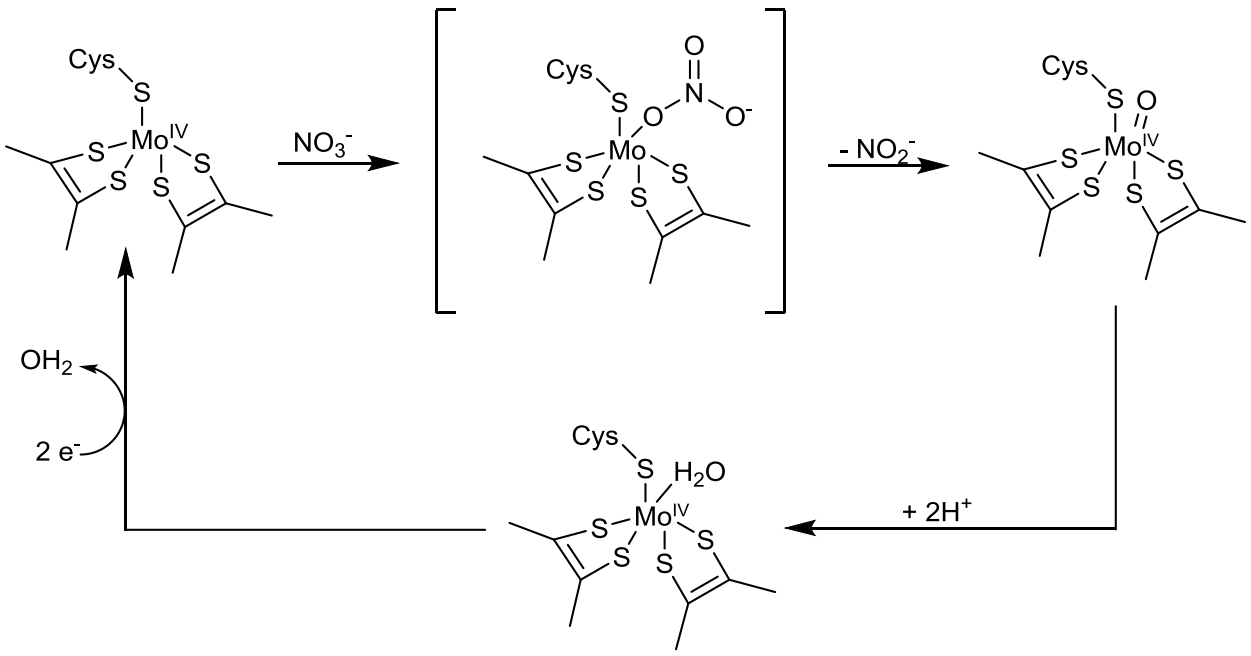

Figure 1.8. Nitrate reductase catalytic mechanism.[31]

The oxidation of Mo^{IV} to Mo^{VI} was then followed with a further reduction by pentaheme cytochrome *c* nitrite reductase via a six electron/eight proton reduction of nitrite to ammonia (NO_2^-+ $8H^+$+$6e^-$ →NH_4^++ $2H_2O$; E˚= 0.34 V).[32a, 33]

Assimilatory nitrate occurs in plants, algae, and bacteria. This process takes place either via eukaryotic or prokaryotic pathways. The eukaryotic path consists of reduction of nitrate to nitrate via the eukaryotic nitrate reductase, and then reduction by the heme nitrite reductase to ammonia. In the prokaryotic system, the pathway involves reduction of nitrate via cytoplasmic nitrate reductase followed by heme nitrite reductase.[30] Following the reduction of nitrate to nitrite is the reduction of nitrite to NO catalyzed by the cytochrome cd_1 or the copper-containing nitrite reductase.

1.5 Nitrite Reductase

Nitric oxide (NO) plays a key role in biological systems as a messenger molecule for regulating immune function, serving as a neurotransmitter in the brain, and for activating iron regulatory factors in macrophages.[24] Nitrite reductase (Figure 1.9) is the metalloenzyme responsible for efficiently reducing

NO_2^- to NO. Nitrite reduction to NO ($NO_2^- + e^- + 2H^+ \rightarrow NO + H_2O$ $E^\circ = 0.35$ V) is a viable route for the investigation of complexes capable of mimicking the biological production of NO. NO targets metal containing proteins which can lead to the formation of dinitrosyl iron complexes (DNICs), as observed in iron sulfur proteins.[3] Iron complexes capable of binding NO play an important role in many physiological and industrial applications.[34]

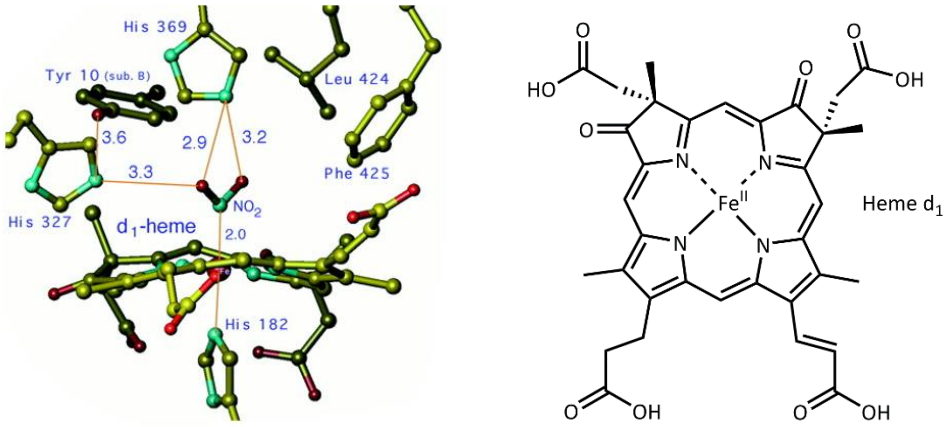

Figure 1.9. Nitrite Reductase: Cytochrome-cd_1.[35, 36]

1.5 The Oxygen Evolving Complex

In many biological electron-transfer reactions, the use of redox inactive metals plays a key role in promoting the reactivity of the system. In nature, the four electron/four proton the photosplitting of water into O_2 occurs during photosynthesis and is essential for human life. The water oxidation process is catalyzed within photosystem II (PSII) which contains a bridging oxo $CaMn_4$ Cluster known as the oxygen evolving complex (OEC) (Figure 1.10).[37]

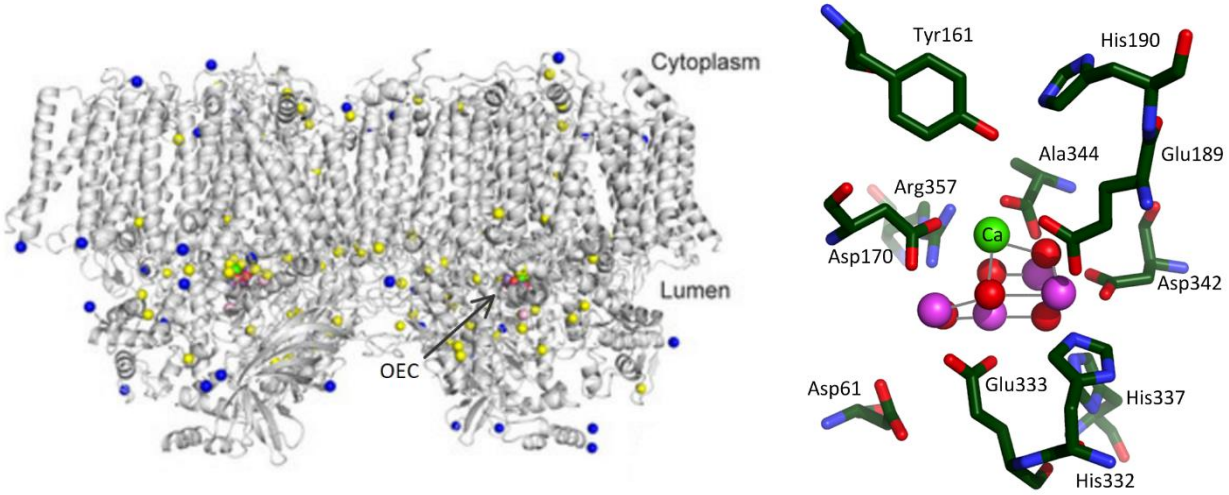

Figure 1.10. Overall structure of the Photosystem II dimer[36b] (left) and the structure of the oxygen evolving complex (OEC) (right).[36e]

The OEC undergoes four e^- transfer events for the oxidation of H_2O to O_2 ($2H_2O \rightarrow O_2 + 4H^+ + 4e^-$). The redox-inactive calcium ion is associated with three of the Manganese centers in a cubane motif (Figure 1.11). The presence of calcium ion is vital for function since the OEC is known to be virtually inactive if Ca^{2+} is removed from its structure.

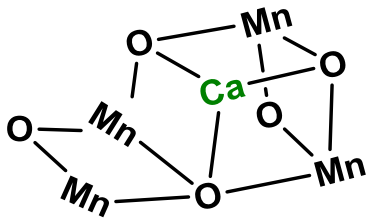

Figure 1.11. ChemDraw representation found within Photosystem II, illustrating the use of the redox-inactive Ca^{2+} (green).

Each oxidation state of the OEC is known as an S-State as seen in the S-State cycle (Figure 1.12) where S_0 is the most reduced state and S_4 is the most oxidized state.[36] The OEC is repeatedly oxidized (one e^- at a time) until it is oxidized four times leading to a high oxidation state of the manganese. The manganese

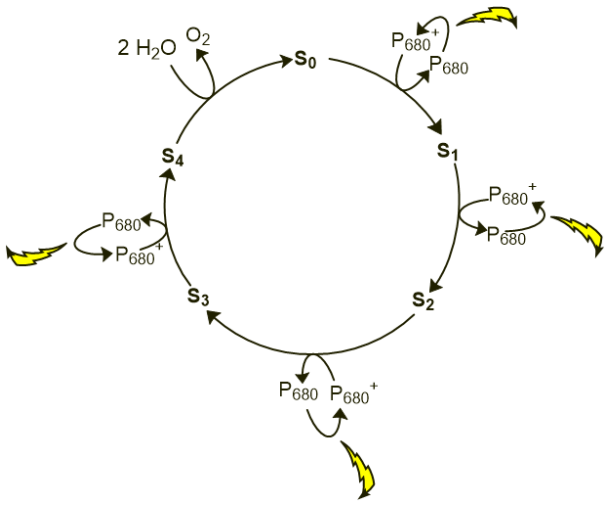

Figure 1.12. The simplified S-state cycle of the OEC in PSII.[36]

Many manganese complexes have been synthesized as possible mimics of the OEC, some of which contain a Mn_4Ca cluster resembling closely the cubane part of the native OEC. However, it is seen from the OEC that the redox inactive metal is a critical component in catalyzing the reaction. Agapie and coworkers have developed synthetic analogues that target the OEC structure in order to study and understand the role of the redox inactive metal (Figure 1.13).[37] Replacement of the calcium various redox-inactive metals in these complexes have allowed for the systematic investigation of the effect each metal has on the system. The designs contain redox inactive metals such as Na^+, Ca^{2+}, Sr^{2+}, Zn^{2+}, and Y^{2+} ions which have that aid in the studying of the importance of these redox inactive metals. Figure 1.13 illustrates two different complexes, a tri Mn oxo bridged cluster with a sodium metal rather than calcium and a tri-iron oxo bridged cluster.

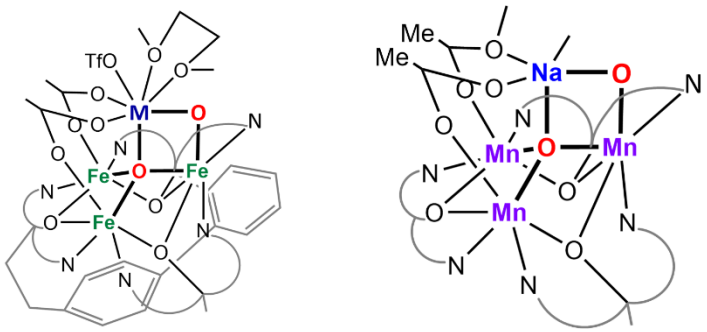

Figure 1.13. Synthetic models of the OEC featuring the cubane motif of the native OEC: Tri Iron Cluster (left)[37a] and Tri manganese cluster (right).[37b]

The results of the study, illustrated by the cyclic voltammetry of these compounds, demonstrated a linear dependence between reduction potential and the pK_a of the metal. The model of the Mn_3 cluster with Y^{3+} resulted in a more positive potential than the Na^+ which showed the least positive potential, suggesting that there is a correlation between reduction potentials and the charge of the redox inactive metals. This means that with the Y^{3+} ion, the Mn centers are easier to reduce due to the more highly charged Lewis acid metal ions withdrawing more e^- density from the Mn centers. Another outcome of these experiments displayed of a linear correlation between the reduction potential of the Mn_3 clusters and the pK_a of the H_2O molecule in the aqueous complex of the redox-inactive metal (Figure 1.14).

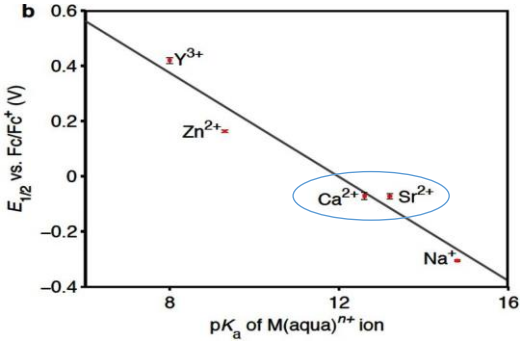

Figure 1.14. The linear dependence shown by the graph of the $E_{1/2}$ vs pK_a of M(aqua)$^{n+}$ ion.[37b]

These results showed that having Sr^{2+} in the system has the same effect on the reduction potential of the manganese clusters as introduction of a calcium metal ion. This suggests that the OEC would still be active if Ca^{2+} were to be replaced with Sr^{2+}. With this work, Agapie and coworkers have shown that

incorporation of a redox inactive metal affects the redox potential of the system. Similar to Agapie, we wanted to investigate the effect of the reduction potentials in our PDI ligand platform after encapsulation of redox inactive metals in the secondary coordination sphere.

1.7 Ligand Design

As described above, some transformations are quite complex and require multielectron redox processes which can be difficult to address when it comes to ligand design. For this reason, it is crucial to design a ligand in which both electrons and protons are able to flow in and out of the system. To address this need, the incorporation of redox activity into metal-ligand scaffolds that mimic relevant metalloenzymes have been utilized. This has further opened up new avenues to explore a variety of chemical transformations. Groups such as Borovik, Szymczak, and Fout have synthesized ligand platforms that can stabilize substrates through H-bond acceptors/donors (Figure 1.15).[38]

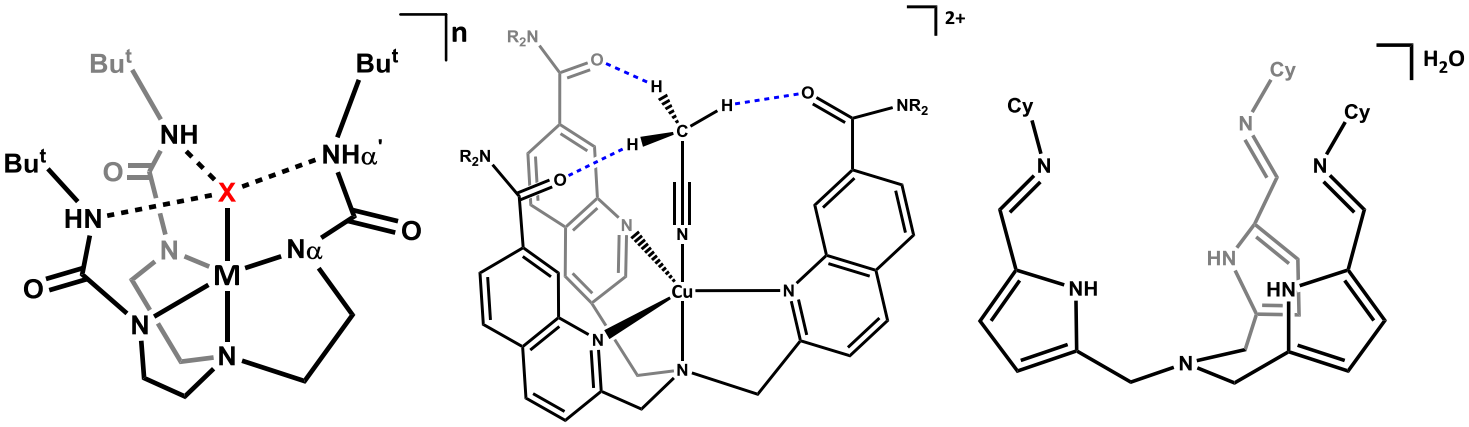

Figure 1.15. MH_3buea complex synthesized by Borovik and coworkers displaying H-bond donors in the secondary coordination sphere (left),[38a] tripodal system by Szymczak illustrating H-bond acceptors in the secondary coordination sphere (middle),[38b] and Fout's ligand framework with H-bond acceptors in the secondary coordination sphere (right).[38c]

The redox-active PDI ligand scaffold has the capability to be protonated while in a highly reduced state, allowing for the transfer of both protons and electrons to substrate.[39,40] For this reason, the synthetically feasible PDI ligand makes the ideal candidate to use since they are redox-active, non -innocent ligands.

This means they are capable of both storing and releasing electrons, allowing access to redox states not typically available to the metal.[39,40] This is particularly useful for facilitating multi-electron transfer reactions. The modular nature of the imine pendant arms also allows for potentially tuning chemical activity of the secondary coordination sphere. These highly modular pendant groups can serve as H bond directors, proton shuttles, or nucleophiles. This allows for the study of two institutions merged into one: the secondary sphere (H-bonding interactions) and getting electrons in the system to carry out useful multi-electron transformations. The secondary sphere allows us to control the reactivity and behavior of the compounds. Given the modularity that the PDI scaffold provides, facile modifications in the secondary coordination sphere yields moieties containing H-bond acceptors/ donors, Lewis acids and bases, and crown ethers capable of chelating redox inactive metals (Figure 1.16).

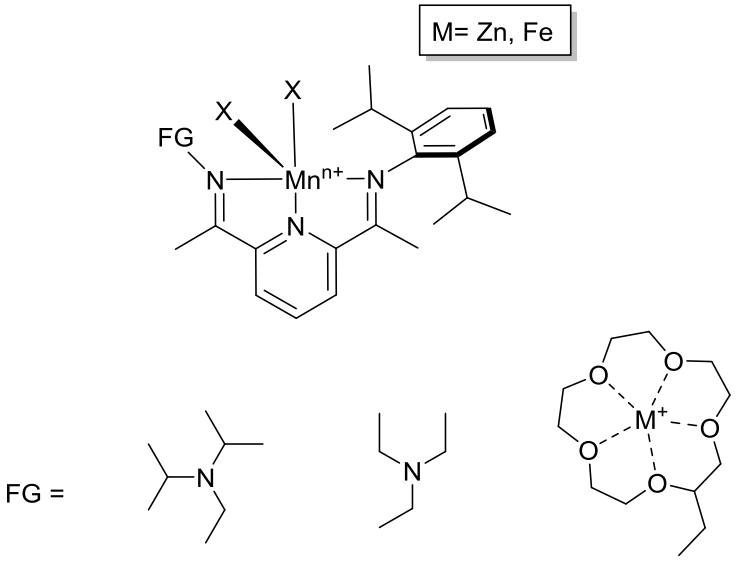

Figure 1.16. Pyridinediimine (PDI) ligand scaffold illustrating the components that can be varied.

1.8 Research Objectives

The research presented here targets the development of small inorganic complexes, consisting of a PDI ligand scaffold and studying the role of the secondary coordination sphere in these complexes. The secondary coordination sphere plays a key role in how these bioinspired ligands tune their reactivities toward performing various chemical transformations. The metal dihalide PDI complexes ($ZnCl_2$, $ZnBr_2$ $FeCl_2$ and $FeBr_2$) were synthesized with varying pK_a of the pendant bases in the secondary coordination sphere according to existing procedures and were characterized through infrared (IR) spectrometry, Mössbauer spectroscopy (if applicable), NMR spectroscopy, and X-ray crystallography. The diispropylamine PDI (didpa) complexes are able to form metal halogen hydrogen bonds (MHHBs) both in solid state and in solution. The protonation state of secondary coordination sphere was probed in order to determine the H-bond strength. DFT analysis was performed on the $ZnCl_2$ and the $ZnBr_2$ species for determination of the intramolecular H-bond. In solution, these complexes were introduced various H-bond accepting solvents and analyzed through their ^1H NMR spectra. Additionally, the iron PDI complexes were reduced under CO atmosphere in order to study their reduction potentials and how altering the protonation state of the coordination sphere would affect the redox-active sites within the ligand scaffold. Furthermore, the reduced species were also used to measure how the pK_a of the pendant amine is altered upon being incorporated into the PDI ligand. This complex can be used reduce nitrate and nitrite to nitric oxide.

In order to investigate the effect that introducing a redox inactive metal would have on the redox potential of the PDI complexes, a 15-crown-5 ether capable of chelating redox inactive metals was appended to our system. Incorporation of Na^+ and Li^+ allowed us to investigate the selectivity of the crown to the different alkali metals, as well as to explore the change incorporation of these metals would have on the redox potential of the PDI system.

Chapter 2. Synthesis of Metal Dihalide PDI Complexes: Zn^{II} and Fe^{II}

The microenvironment around the metal ion(s) of metalloprotein active site(s) is important in determining its structure, function, and reactivity.[41] A key interaction in the primary and secondary coordination sphere of biological systems is hydrogen bonding.[41-43] The non-covalent hydrogen bonding network(s) that form around the metal ion are capable of tuning the redox potentials, orienting substrate, and aiding in proton transfer reactions.[41] Many of these chemical transformations in Nature consist of multi-electron processes. Therefore, model systems which incorporate redox-activity along with the ability to modify the secondary coordination sphere by providing H-bond donors/ acceptors is a feature that many aim for in developing ligand scaffolds.

The importance of H-bonding in biological systems is observed in enzymes such as Myoglobin and Hemoglobin, both responsible for the reversible binding of dioxygen. The active site of myoglobin consists of a heme cofactor with a histidine residue coordinated to the iron center and a second histidine residue that sits in close proximity to the iron center. The framework of this enzyme provides an open coordination site to the iron center, allowing O_2 to bind (Figure 2.1). Hydrogen bonds play a key role in O_2 binding and its stabilization, as observed with the H-bonding of bound O_2 to the distal histidine in Myoglobin. It has been observed that altering the H-bonding networks significantly affects O_2 binding affinity.[42]

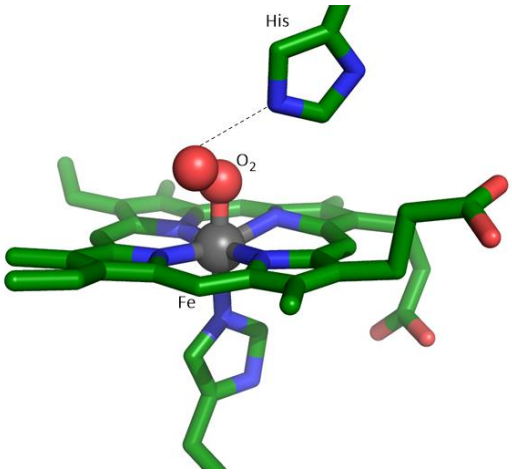

Figure 2.1. Structure of the active site of myoglobin illustrating the intramolecular H-bonding interaction to bound O_2 (Figure made in PyMOL).[43]

In order to study the effects that H-bond interactions play in biological systems, synthetic models have been developed that portray features of the native active sites. Synthetic systems such as those developed by Borovik and coworkers[21,44] have focused on examining the H- bonding networks necessary for dioxygen binding and activation by metal complexes. The system contains three urea groups which can provide anionic donors and intramolecular hydrogen bonding. The secondary coordination sphere of their bioinspired design closely resembles that of the native active site in hemoglobin, making it an ideal candidate for the binding of O_2 (Figure 2.2).[21,44]

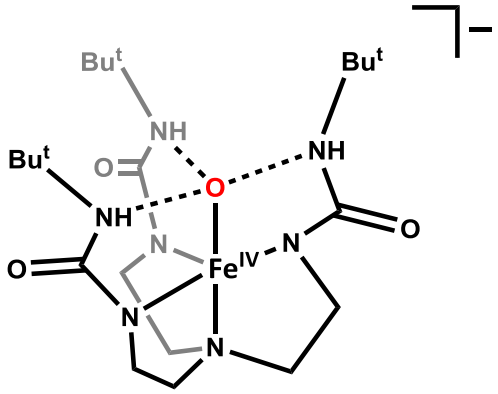

Figure 2.2. The $[Fe(IV)H_3buea(O)]^-$ complex illustrating intramolecular H-bonds formed with Fe-O.[21,44]

In a similar study, H-bonding networks within the secondary coordination sphere are suggested to assist in the binding of O_2, leading to activation of O_2 and formation of the Fe^{III}-OH and Co^{III}-OH complexes.[45] Differences in the reactivity with dioxygen were observed throughout the series of these varied H-bond donor complexes (Figure 2.3).

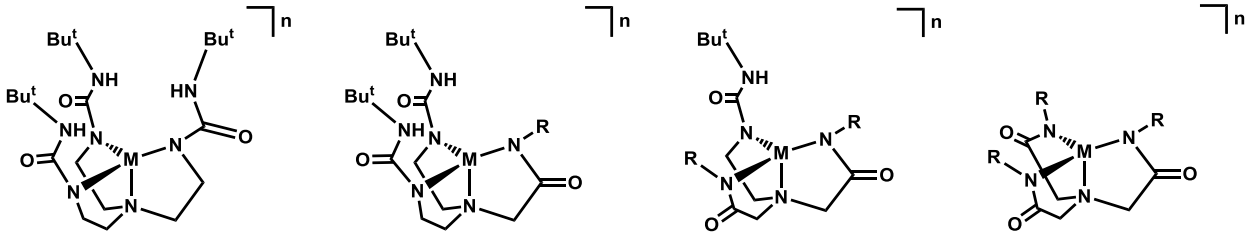

Figure 2.3. Urea-based tripodal complexes with varied intramolecular H-bond networks.[45]

The complex providing a higher number of intramolecular H-bonds showed reactivity with O_2 whereas the one with no H-bonding network showed no reaction. These results further illustrate that altering the secondary coordination sphere can influence the reactivity of the primary sphere.

Another example of the importance of hydrogen bonding comes from the production and oxidation of H_2 (Eq. 2.1). Hydrogenase enzymes used to catalyze the production and oxidation of H_2 are Fe-Fe hydrogenase and NiFe Hydrogenase (Figure 2.4). The amine in Fe-Fe hydrogenase facilitates the heterolytic cleavage of H_2, yielding turnover frequencies of over 9000 s^{-1}.[46] Ni and Co functional models of these hydrogenase enzymes have been synthesized to catalyze the production and oxidation of H_2.

$$H_2 \rightleftharpoons 2H^+ + 2e^- \qquad \textbf{(2.1)}$$

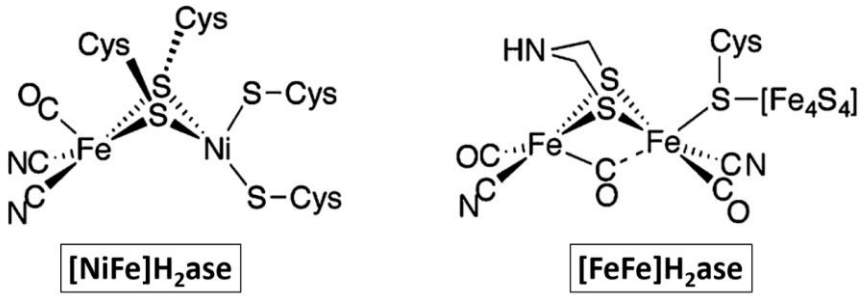

Figure 2.4. Structures of the [NiFe] hydrogenase (left) and [FeFe] hydrogenase (left) responsible for the production and oxidation of H_2.[47]

Dubois and coworkers have synthesized diphosphine ligand systems with the incorporation of pendant amines.[48] These pendant amines can serve as proton relays that help accelerate intra and intermolecular proton mobility, overall facilitating the heterolytic cleavage of H_2. The ability to promote fast proton transfer between mental and amine enables the proton relays to enhance the rates of catalytic reactions. Proton relays minimize the barriers for the movement of protons through use of pendant amines as illustrated in Figure 2.5.[49] The stabilization of H_2 binding is observed by the interaction between the two positioned pendant bases in the ligand platform.

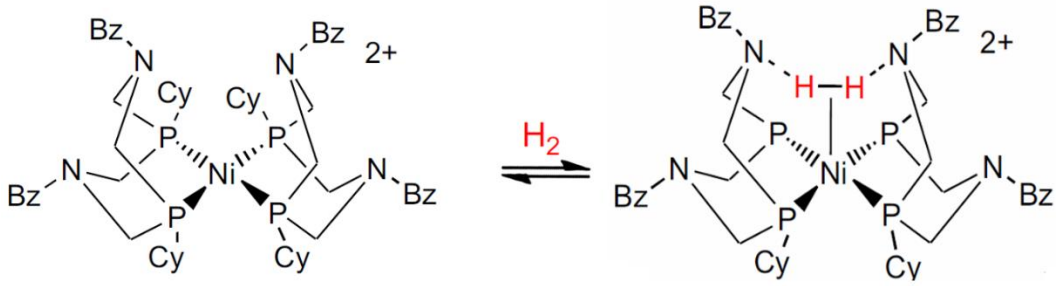

Figure 2.5. $[Ni(PCy_2\ NBz_2)_2]^{2+}$ synthetic model of Ni-Fe Hydrogenase for the oxidation of H_2, illustrating how pendant amines can serve as proton relays to stabilize the H_2 intermediate.[50]

Parson's and coworkers have developed tripodal tetradentate tris(pyridyl-2-methyl)amine-based (TPA) ligands with hydrogen bond donors in the secondary coordination sphere (Figure 2.6). When providing hydrogen bond donors to the CuCl $NHCO^tBu$ pivaloylamido ($L^{Piv-1,2,3}$) TPA complex, a change in redox behavior of the metal center is observed due to the metal halogen hydrogen bonds (MHHBs). In this system there is a change ranging from 0.025 - 0.500 V of the $Cu^{II/I}$ couple.[51,52]

Similarly, Mayer's work demonstrates a change in the reduction potential of ~500 mV upon protonation of the iron complex of tetraphenylporphyrin (TPP) and the ruthenium complex of 4-methylimidazole (imH) (Figure 2.6).[53] Likewise, a 350 mV shift is observed upon protonation of the pyridine–imidazole ligand in ruthenium bis(β-diketonato) complexes.[49]

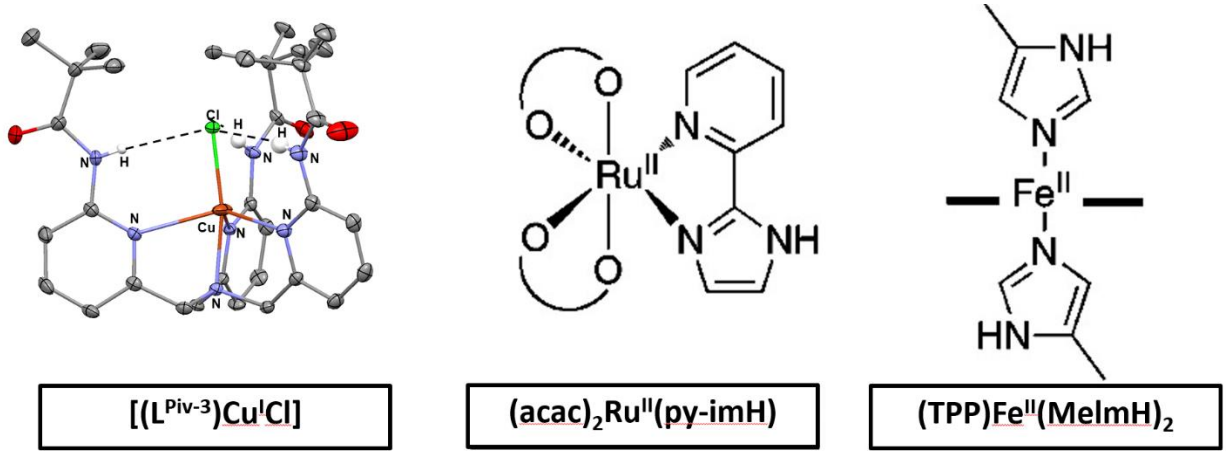

Figure 2.6. Left: [(LPiv-3)CuICl] complex illustrating the internal N–H · · · Cl–Cu (MHHB) hydrogen bonding-shifts in reduction potential range from $\Delta E_{1/2}$ ~0.025 - 0.500 V; middle: $(acac)_2Ru^{II}(py\text{-}imH)$ complex upon protonation with $\Delta E_{1/2}$ ~0.5 V; right: $(TPP)Fe^{II}(MeImH)_2$ complex which exhibits a shift in reduction potential of $\Delta E_{1/2}$ ~ 0.350 V.

These complex models, however, rely on the metal center to perform redox chemistry.[54,55] The work focused here utilizes the pyridinediimine (PDI) ligand scaffold which allows more than one coordination site to be accessible. The PDI system is highly modular and many functional groups can be appended which also allows for secondary coordination sphere tuning (Figure 2.7).

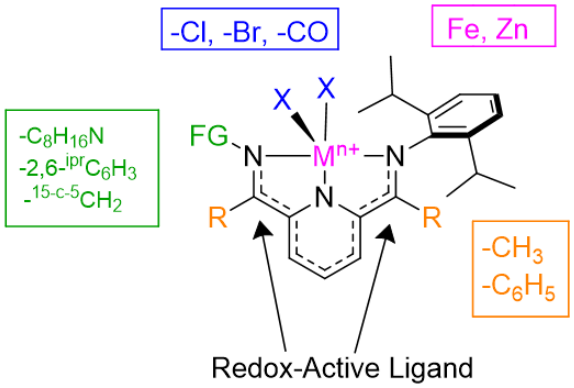

Figure 2.7. Redox-active PDI ligand scaffold illustrating the modularity in the primary and secondary coordination sphere.

The PDI ligand backbone has been shown to be redox active and can access four oxidation states, and can store up to three electrons.[56-58] The storage of two electrons in the system can be observed in (Eq. 2.2). For this reason, multi-electron chemistry can be achieved, allowing electrons from the ligand to be stored, and flow in and out of the system. A redox active ligand, such as the PDI scaffold, allows for multi-electron redox process to be performed. Furthermore, we are able to use a redox active metal like zinc as the active metal site since the PDI ligand can provide the electrons necessary for chemical transformations.

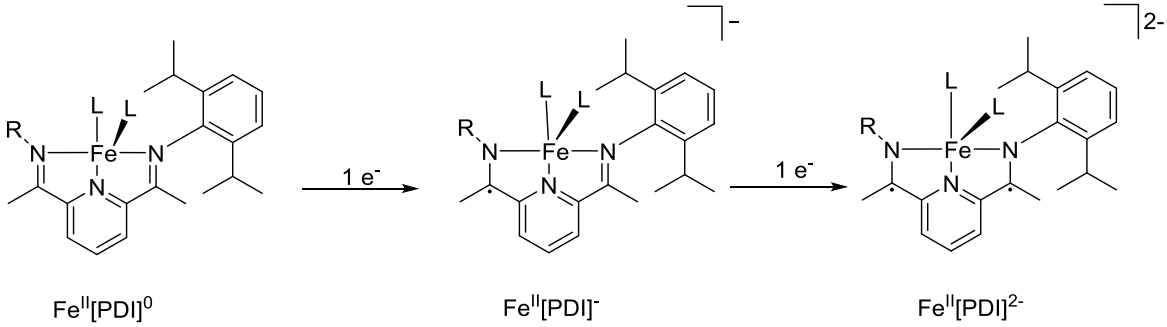

(2.2)

In this study, we use the 2,6-diisopropylamine pendant group to synthesize zinc(II) and iron(II) PDI complexes in order to study the secondary coordination sphere and redox activity of these complexes. It has been previously observed that Fe(II) [(2,6-^{i}PrC$_6$H$_3$)N=CMe)(N(^{i}Pr)$_2$C$_2$H$_4$)N=CMe)C$_5$H$_3$N] (didpa) complexes are able to form H-bond interactions in the secondary coordination sphere. The protonated pendant amine of these didpa complexes provides intramolecular H-bonding to the Fe-X (X= Br^- or OH^-), allowing for the stabilization of complexes like the Fe(II) hydroxo ligand.[39] A desire to further probe the secondary coordination sphere interactions and its potential to tune the redox activity of the primary coordination sphere came about from these results.

2.1 Synthesis of the Didpa Ligand

The ligand [(2,6-^{i}PrC$_6$H$_3$)N=CMe)(N(^{i}Pr)$_2$C$_2$H$_4$)N=CMe)C$_5$H$_3$N] (didpa, **2**) was synthesized via a Schiff base condensation with starting materials [(2,6-^{i}PrC$_6$H$_3$)N=CMe)(O=CMe)C$_5$H$_3$N] (**1**) and an excess of N,N-diispropylethylenediamine in a 20 mL pressure vial. After 2 days at 90°C, the solution changed from a pale yellow to a clear, dark yellow solution of **2** (Eq. 2.3).[39] The solution was moved to the freezer after the addition of 10 mL of methanol. The solution remained in the freezer for 1 day to yield an off-white solid, which was filtered through a Buchner funnel to obtain a 90% yield.

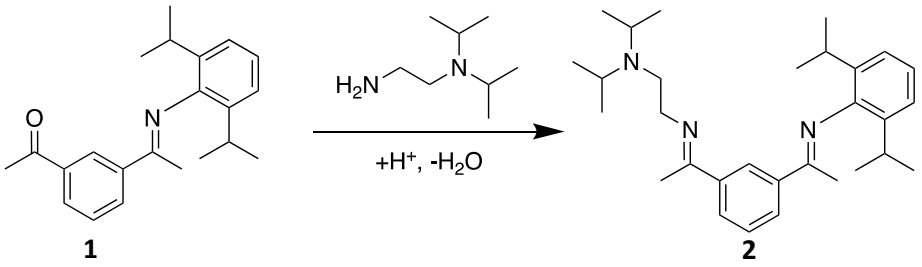

1 **2** **(2.3)**

Fourier transform infrared (FTIR) and nuclear magnetic resonance (NMR) analysis confirm the identity of the didpa ligand. The IR shows lack of a carbonyl (C=O) stretch at 1698 cm^{-1} from the monoimine, verifying

that no starting material is present (Figure 2.8).[39] The FTIR also displays the imine (C=N) stretches at 1642 cm^{-1} and 1581 cm^{-1}, expected from the product.

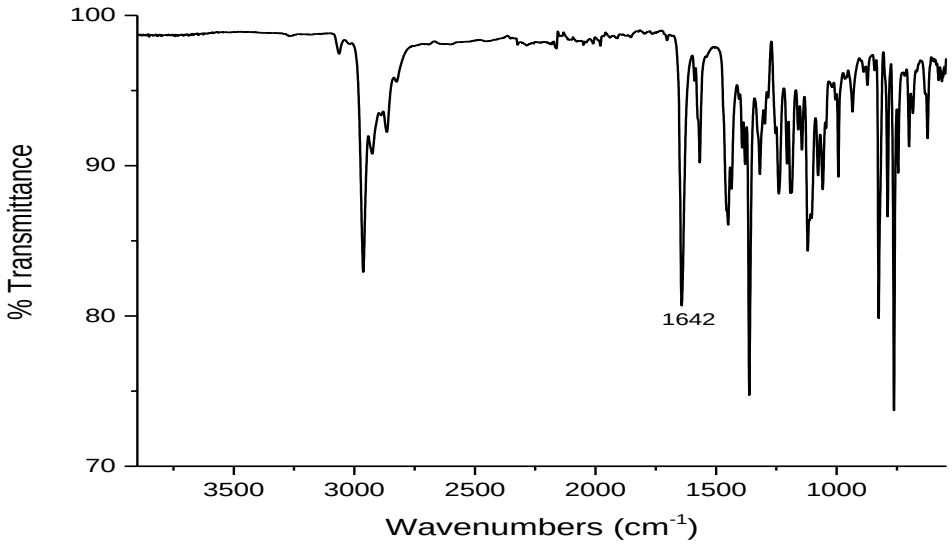

Figure 2.8. Solid-state FTIR spectrum of the didpa ligand.

The ^{1}H NMR spectrum of **2** reveals two septets at 3.79 ppm and 2.79 ppm, each integrating for two protons (Figure 2.9). The septet at 3.79 ppm is a result of the protons from the isopropyl group of the 2,6-diisopropyl aryl group, while the one at 2.79 ppm is representative of the diisopropyl from the pendant amine. The ethylene bridge protons of the pendant arm can also be observed at 2.87 ppm and 3.60 ppm as two triplets.

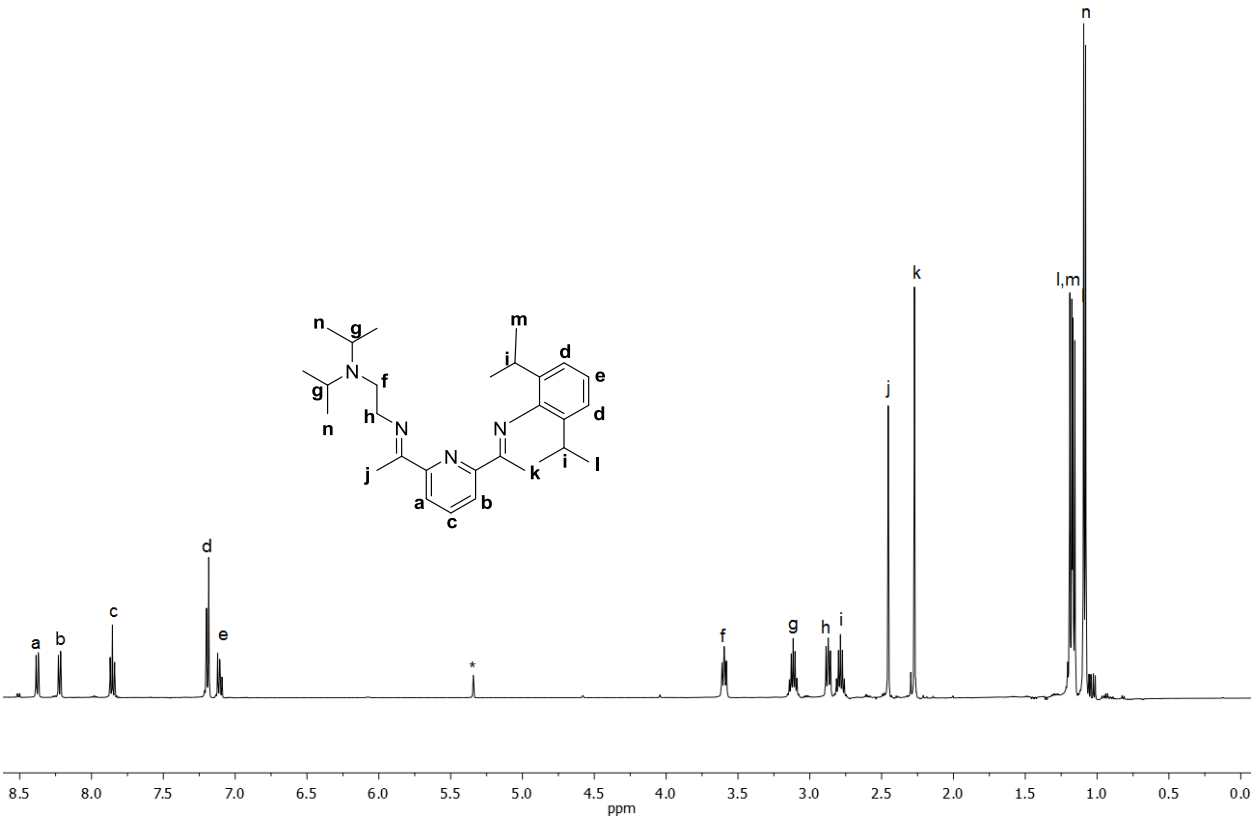

Figure 2.9. ^{1}H NMR spectrum of didpa (**2**) (500 MHz, CD_2Cl_2) (*represents solvent).

2.2 Metallation with Zinc and Iron

The zinc(II) complex was synthesized using [(2,6-^{i}PrC_6H_3)N=CMe)(N(^{i}Pr)$_2C_2H_4$)N=CMe)C_5H_3N] (didpa) in order to study the secondary coordination sphere interactions. The addition of $ZnCl_2$ in THF to the methylene chloride solution of the free ligand, didpa, produced a color change from pale yellow to dark orange (Eq. 2.4). The solution stirred overnight, then filtered through a Celite plug. The filtered solution was layered with diethyl ether and placed in a -10°C freezer, yielding bright yellow crystals identified as Zn(didpa)Cl_2 (**3**).

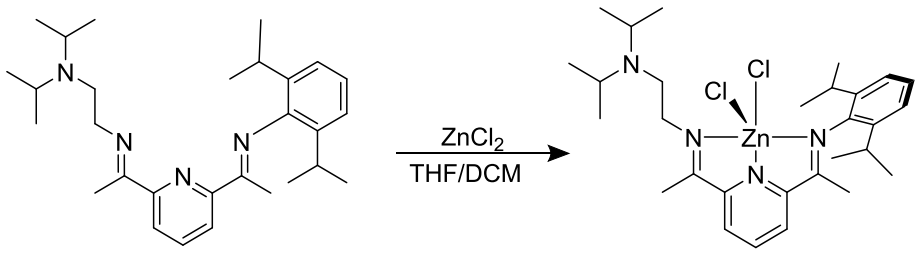

(2.4)

2 **3**

The solid-state IR spectrum of the zinc complex displays a stretch at 1639 cm^{-1} similar to that of the free ligand, from the C=N amine bond (Figure 2.10). The 1585 cm^{-1} is also observed, corresponding to the C=N bond from coordination of the diisopropyl pendant amine arm.

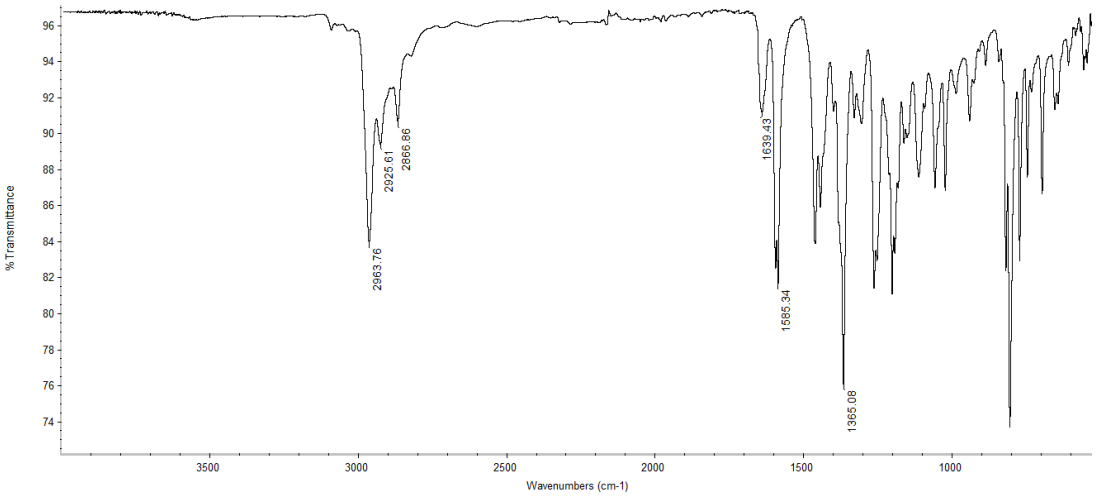

Figure 2.10. Solid-state FTIR spectrum of Zn(didpa)Cl_2 (**3**).

Upon inspection of the ^{1}H NMR spectrum, slight changes are observed from that of the free ligand (Figure 2.11). The two septets are not fully visible as in the case of the free ligand. Instead, there is one septet at 2.97 ppm and one multiplet at 3.06 ppm. The septet represents the didpa diisopropyl protons and the multiplet is comprised of the protons from the diisopropyl group of the aryl ring, as well as two protons from the ethylene bridge. The aromatic region has also changed. There are only three resonances observed corresponding to the six protons from the aromatic rings, whereas the free ligand contains five

well defined resonances present. The environment of the surrounding protons is now altered due to the introduction of the metal in the complex.

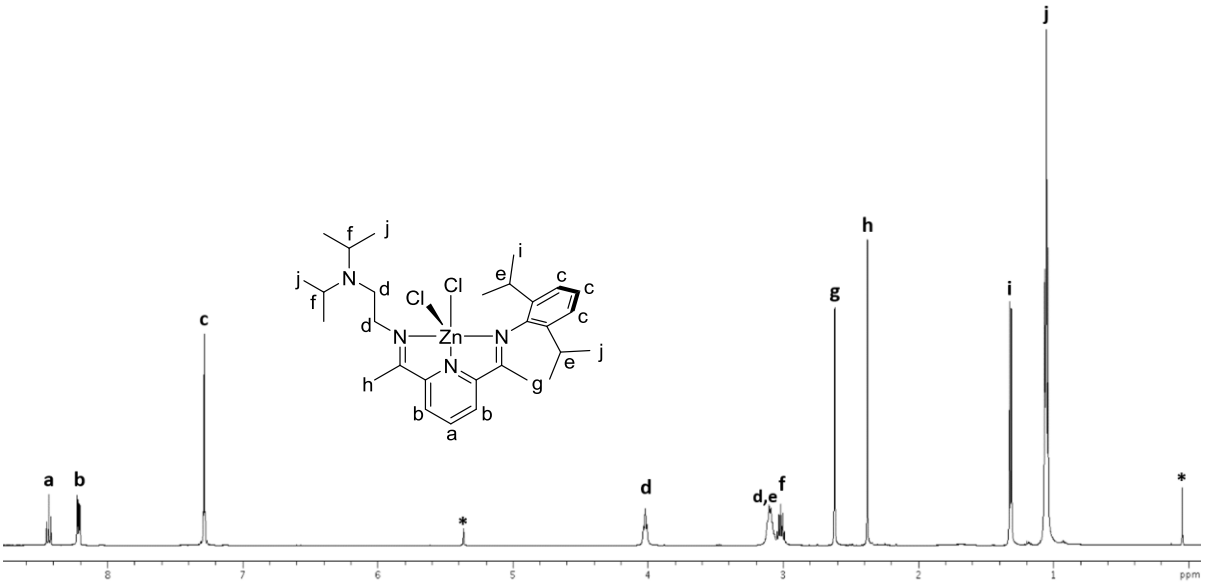

Figure 2.11. ^{1}H NMR spectrum of Zn(didpa)Cl_2 (**3**) (500 MHz, CD_2Cl_2) (*represents solvent).

The X-ray crystallographic analysis of the crystals formed from this product allowed us to observe the pincer ligand in which the zinc(II) sits in the N-N-N binding pocket of the complex. The geometry of a five-coordinate zinc system can be determined by using a structural index parameter (τ) defined by (β-α)/ 60, where β is the largest angle around the metal center and α is the second largest angle around the metal center. A τ value of zero represents a perfectly square pyramidal geometry, whereas a τ value of 1 displays a trigonal bipyramidal geometry.[59] The solid-state structure obtained of this five-coordinate complex (Figure 2.12) gives a τ value of 0.34, suggesting it has distorted square pyramidal geometry.

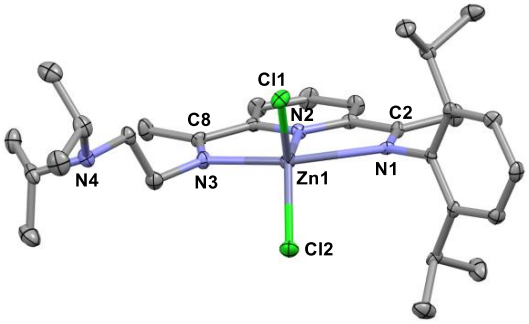

Figure 2.12. Solid-state structure of Zn(didpa)Cl_2 (**3**)**;** Selected bond lengths (Å) and angles (deg): Zn(1)−Cl(1) 2.251(2), Zn(1)−Cl(2) 2.243(2), Zn(1)−N(1) 2.423(6), Zn(1)−N(2), 2.084(6), Zn(1)−N(3) 2.210(6), C(2)−N(1) 1.278(9), C(8)−N(3) 1.292(9), and Cl(1)Zn(1)Cl(2) 113.89(9), N(2)Zn(1)Cl(1) 127.74(18), and N(1)Zn(1)N(3) 147.9(2).

The Zn(didpa)Br_2 was synthesized in a similar manner as complex **3**. A CH_2Cl_2 solution of the didpa ligand and a solution of $ZnBr_2$ in THF were mixed together, resulting in an orange solution (Eq. 2.5). The solution stirred overnight before being filtered through a Celite plug and layered with Et_2O. The resulting orange crystals were isolated and characterized to confirm the synthesis of Zn(didpa)Br_2 (**4**).

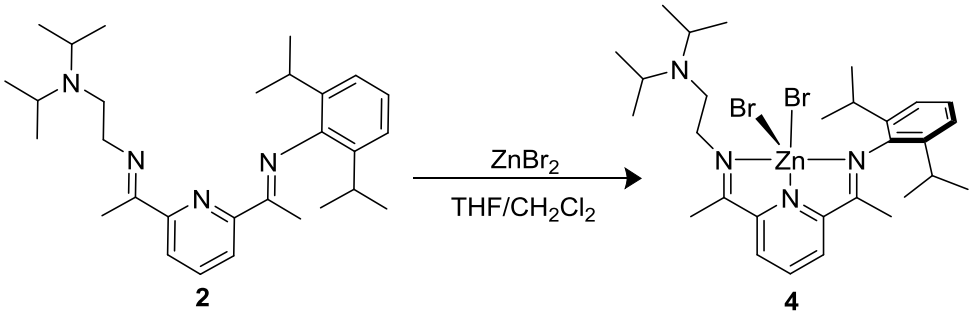

(2.5)

Similar to the Zn(didpa)Cl_2 complex, the solid-state structure of **4** illustrates the five-coordinate complex (Figure 2.13). The solid-state FTIR spectrum of Zn(didpa)Br_2 (**4**) exhibits stretches at 1635 cm^{-1} and 1584 cm^{-1} due to the imine stretches of the complex (Figure 2.14). These stretches are similar to those of the IR spectrum observed in (**3**).

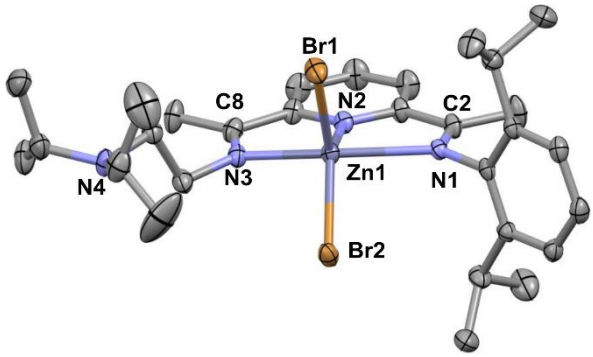

Figure 2.13. Solid-state structure of Zn(didpa)Br_2 (**4**). Selected bond lengths (Å) and angles (deg): Zn(1)-N(2) 2.085(4), Zn(1)-N(3) 2.214(4), Zn(1)-Br(2) 2.3666(8), Zn(1)-Br(1) 3.3749(8), Zn(1)-N(1) 2.374(4), N(1)-C(2) 1.274(6), N(2)-C(7) 1.340(6), N(3)-C(8) 1.261(7), C(2)-C(3) 1.496(7), C(7)-C(8) 1.499(7), N(2)-Zn(1)-Br(2) 131.47(11), N(2)-Zn(1)-Br(1) 112.58(11), N(3)-Zn(1)-Br(1) 100.07(11), Br(2)-Zn(1)-Br(1) 115.95(3), N(3)-Zn(1)-N(1) 145.44(15).

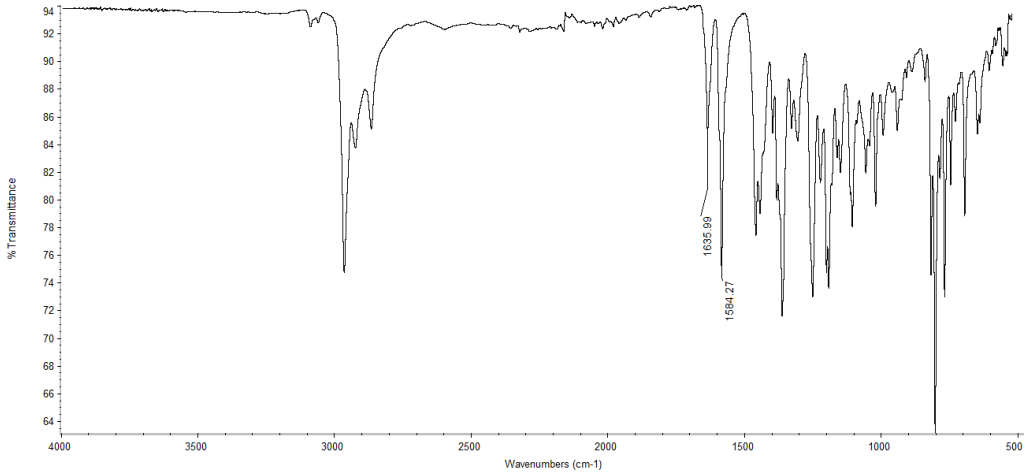

Figure 2.14. Solid-state FTIR spectrum of Zn(didpa)Br_2 (**4**).

The NMR spectrum of Zn(didpa)Br_2 further confirms the synthesis of the product (Figure 2.15). The aromatic region displays three peaks at 8.43 ppm, 8.21 ppm and 7.26 ppm which correspond to the protons of the aromatic rings of the complex. The appearance of a multiplet at 3.01 ppm integrates for six protons and is due to the protons from the isopropyl group of the diisopropyl aryl group and the diisopropyl group of the didpa ligand. Two of the protons from the ethylene bridge are also included into the multiplet. The other two ethylene bridge protons from the pendant amine arm shows up at triplet at 4.07 ppm.

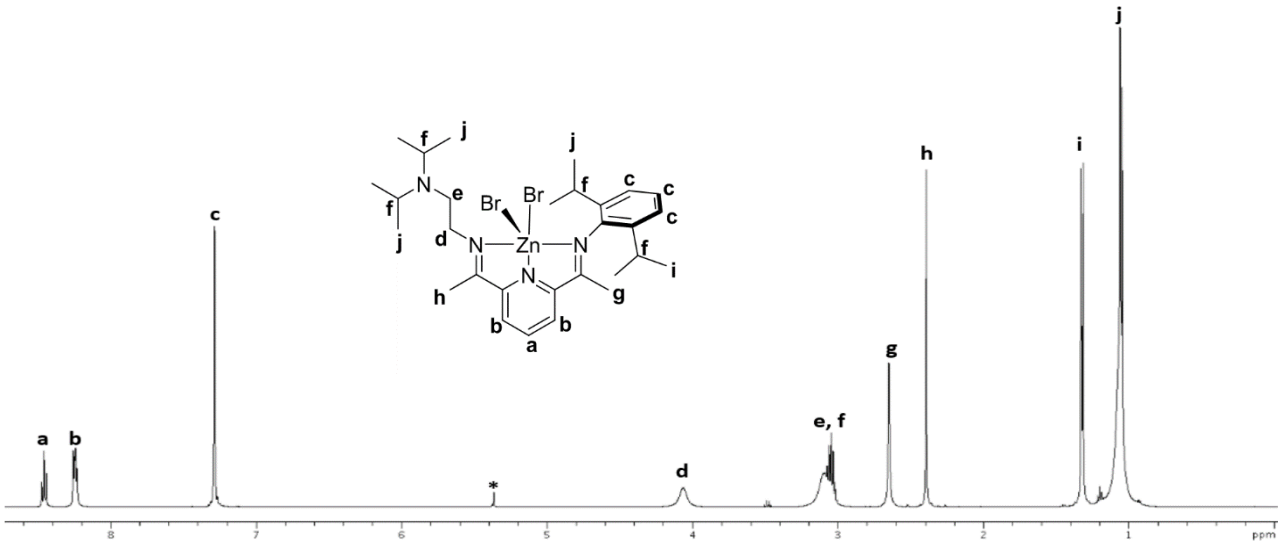

Figure 2.15. The ^{1}H NMR spectrum of Zn(didpa)Br_2 (**4**) (500 MHz, CD_2Cl_2) (*represents solvent).

The Fe(II) analogue was also synthesized. In a nitrogen filled glovebox, the didpa ligand was dissolved in CH_2Cl_2 and carefully added to a solution of $FeCl_2$ in THF to produce a dark blue solution (Eq. 2.6). The solution was stirred for one day and then filtered through celite to remove any impurities.

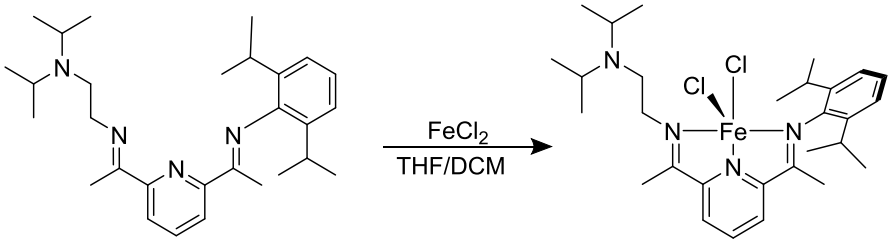

2 **5** **(2.6)**

The IR spectrum of **5** displays two stretches at 1619 cm^{-1} and 1581 cm^{-1}, corresponding to the C=N amine stretches found in these complexes (Figure 2.16).

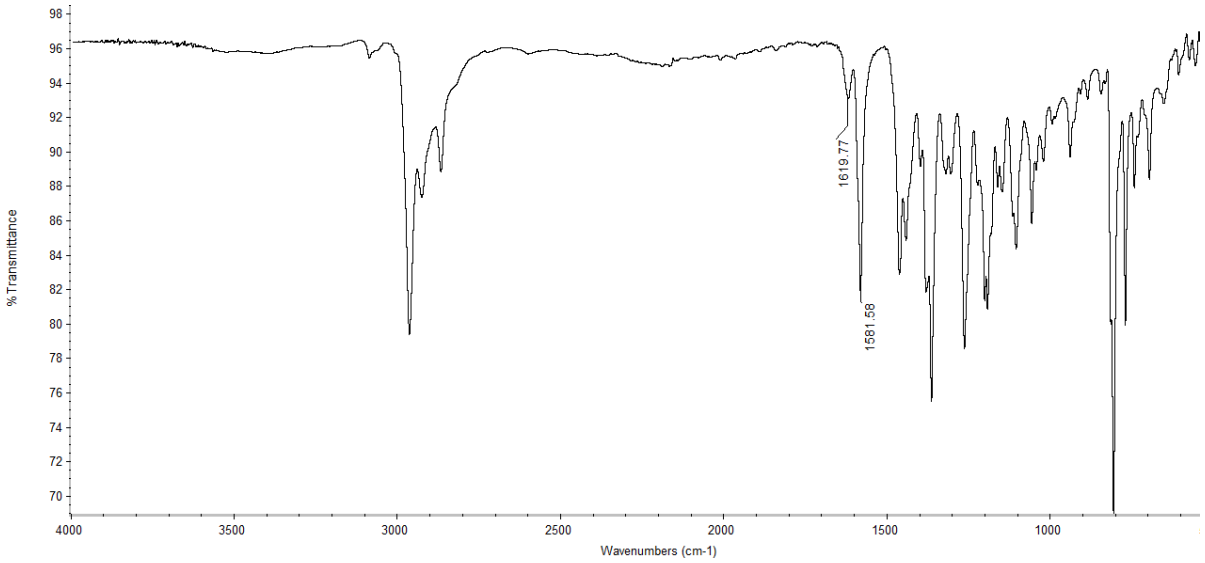

Figure 2.16. Solid-state FTIR spectrum of $Fe(didpa)Cl_2$ (**5**).

However, the synthesis could not be confirmed by means of NMR due to the paramagnetic nature of the species (Figure S3). A solid-state structure (Figure 2.17) was obtained to confirm the synthesis. The solid-state structure reveals a five-coordinate distorted square pyramidal geometry (τ =0.34). The measured effective magnetic moment (μ_{eff}) for this complex can be measured in solid-state via a magnetic susceptibility balance, or in solution by Evan's NMR method measurements.[60] The solid-state also allows a measured μ_{eff} value of 5.8 μ_B and 5.7 μ_B in solution, suggesting a high spin (S=2) Fe(II) center.

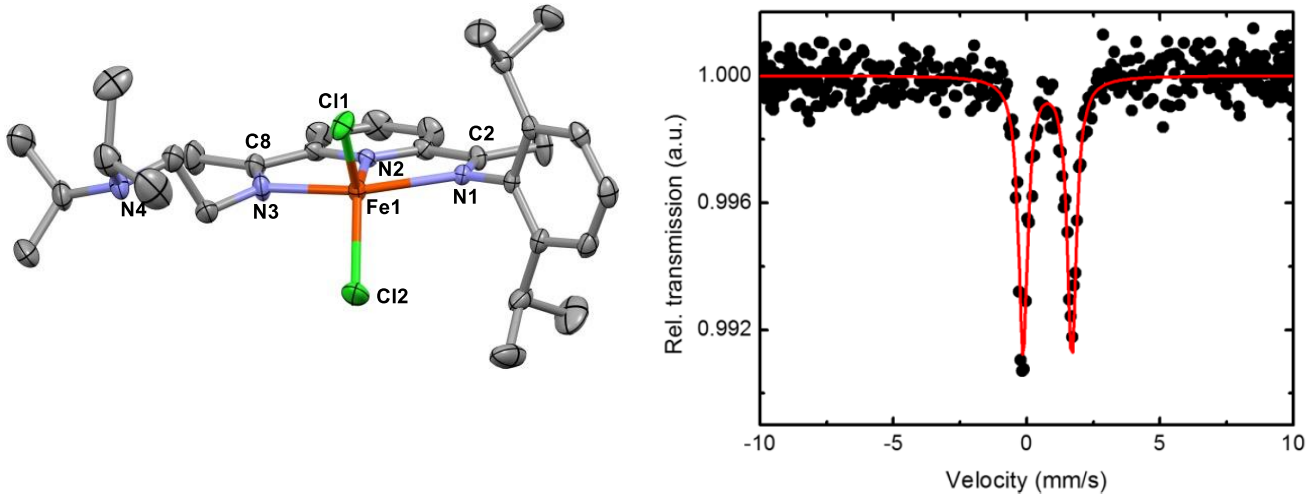

Figure 2.17. Solid-state structure of $Fe(didpa)Cl_2$ (**5**) (left) and Room-temperature zero-field ^{57}Fe Mössbauer spectrum of $Fe(didpa)Cl_2$ (**5**) (right) [δ = 0.882(3) mm/s, ΔE_Q = 1.841(7) mm/s]. Selected bond lengths and angles: Fe(1)−Cl(1) 2.2959(12), Fe(1)−Cl(2) 2.2790(14), Fe(1)−N(1), 2.285(3), Fe(1)−N(2)

2.117(3), Fe(1)−N(3) 2.192(3), C(2)−N(1) 1.283(5), C(8)−N(3) 1.280(6), and Cl(1)Fe(1)Cl(2) 109.52(6), N(2)Fe(1)Cl(1) 124.58(9), and N(1)Fe(1)N(3) 146.39(13).

In order to confirm the oxidation state of the iron center, the room-temperature Mössbauer spectrum of the complex was analyzed. The results yielded an isomer shift (δ) of 0.882(3) mm/s and a quadrupole splitting (E_Q) value of 1.841(7) mm/s, consistent with the parameters of other previously synthesized high-spin iron center complexes.[61-64] Relevant Mössbauer parameters of Fe(II) PDI complexes are summarized in Table 2.1.

Table 2.1. Pertinent Room-temperature zero-field ^{57}Mössbauer parameters of Fe(II) PDI complexes.

PDI complex	Isomer shift (δ) [mm/s]	Quadropole splitting (ΔE_Q) [mm/s]	Ref
Fe(didpa)Cl_2	0.882(3)	1.841(7)	65
[Fe(Hdidpa)Cl_2][PF_6]	0.863(45)	1.933(8)	65
Fe(didpa)$(CO)_2$	−0.061	1.43	65
[Fe(Hdidpa)(CO_2)][PF_6]	-0.075(5)	1.435(8)	65
Fe(^{MeO}PDI)Br_2	0.644 (9)	1.13 (2)	57
Fe(^{MeNH}PDI)Cl_2	0.835 (7)	1.06 (1)	58
Fe($^{(Me)_2N}$PDI)Cl_2	0.840 (2)	1.215 (4)	58
Fe(^{Bpin}PDI)Cl_2	0.868 (5)	1.23 (1)	58
Fe(^{MeNH}PDI)$(CO)_2$	-0.076 (9)	1.25 (2)	58
Fe($^{(Me)_2N}$PDI)$(CO)_2$	-0.061 (1)	1.07 (2)	58
Fe(^{Bpin}PDI)$(CO)_2$	-0.061 (4)	1.510 (8)	58
(^{iPr}EtPDI)FeN_2	0.37	1.75	66
(^{iPr}iPrPDI)FeN_2	0.37	1.85	66

2.3. Protonation of the Zn(II) and Fe(II) Species

The pendant base of the zinc(II) complex was protonated with a weak acid, ammonium hexafluorophosphate (NH_4PF_6). A yellow solution of Zn(didpa)Cl_2 in THF was reacted with NH_4PF_6 in MeOH, and allowed to stir overnight (Eq. 2.7). The solution was filtered through a celite plug and layered with diethyl ether. The solid-state structure revealed the formation of the protonated complex, [Zn(Hdidpa)Cl_2][PF_6] (**6**).

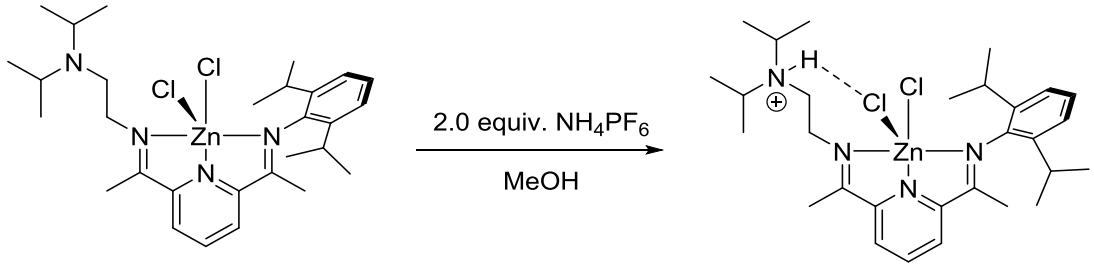

(2.7)

3 **6**

The IR spectrum contains an amine stretch (C=N) at 1642 cm^{-1} (Figure 2.18). However, the NH stretch expected to be observed from this product is not present. This absence could be a cause of the intramolecular hydrogen bonding of this complex. This lack of a resolved NH stretch is common in other complexes that are involved in intramolecular hydrogen bonds.[67] Also observed is the PF_6^- counterion at 832 cm^{-1}.

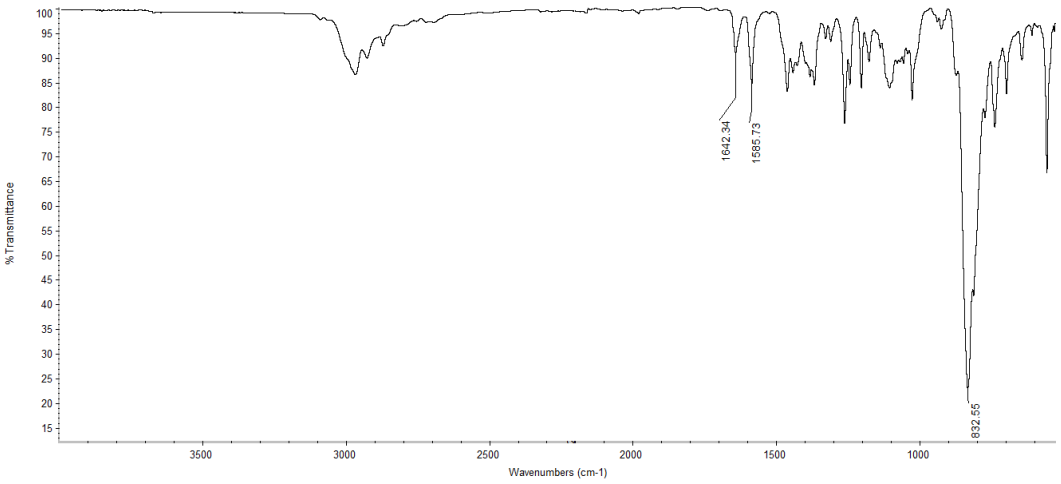

Figure 2.18. Solid-state FTIR spectrum of $[Zn(Hdidpa)Cl_2][PF_6]$ (**6**).

Upon inspection of the ^1H NMR spectrum (Figure 2.19), a new resonance is observed at 8.50 ppm as a result of the protonated diisopropylamine pendant arm of the complex. There is a clear downfield shift of this N-H resonance to the aromatic region due to intramolecular hydrogen bonding. Similar to the ^1H NMR of the free ligand, the aromatic region of the spectrum contains five distinct resonances, corresponding to the two aromatic rings. The ethylene bridge proton resonances show up at 4.37 ppm and 3. 74 ppm as

two triplets. At 3.86 ppm we observe a septet corresponding to the diisopropyl protons of the pendant amine.

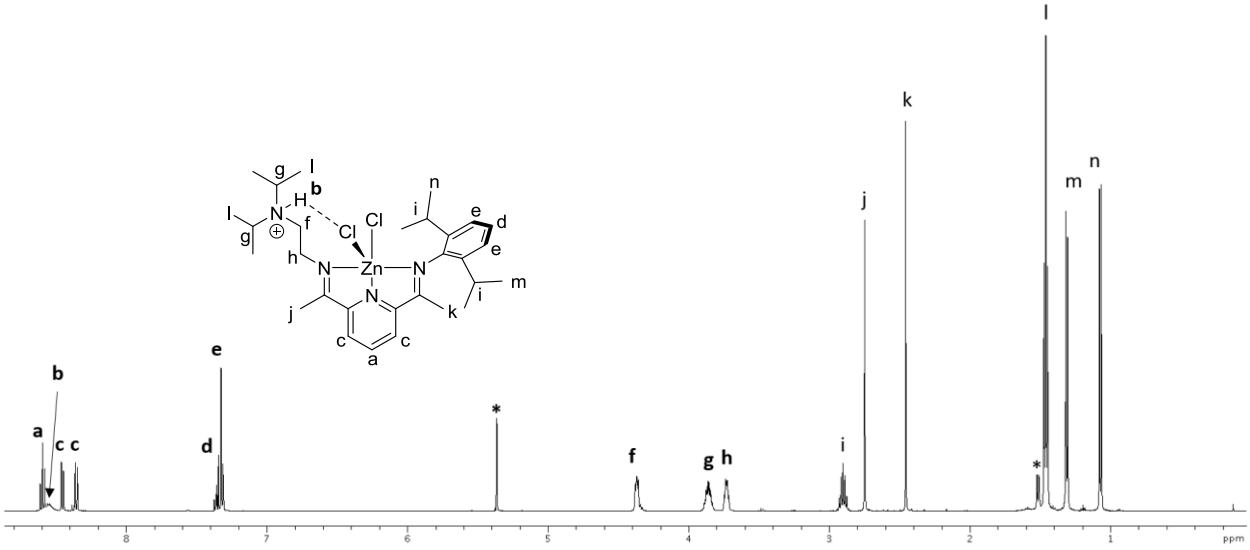

Figure 2.19. ^{1}H NMR of [Zn(Hdidpa)Cl_2][PF_6] (**6**) (500 MHz, CD_2Cl_2) (*represents solvent).

The solid-state structure (Figure 2.20) indicates square pyramidal geometry of **6** (τ = 0.00). The solid-state structure also exhibits the intramolecular hydrogen bonding, previously determined from the proton NMR. Hydrogen bonding occurs between the zinc, one of the chlorine atoms, and the protonated pendant diisopropyl (Zn-Cl···H-N), making a metal halogen hydrogen bond (MHHB). A further indication of intramolecular H-bonding can be seen in the solid-state structure by the fact that the N-H group is directed toward the Cl atom that it is H-bonding with. The bonds lengths yielded 2.17(6) Å for the N-H···Cl distance and 3.152 (6) Å for the N···Cl distance. Steiner describes a strong hydrogen bond of a Cl···H to be 1.2-1.5 Å, the N-H···Cl angle of 170-180°, and the N···Cl distance of 2.5-3.2 Å.[52] The parameters of what constitutes medium and weak hydrogen bonds are summarized in Table 2.2. The presence of MHHBs in other systems result in similar spectroscopic data that we observe in [Zn(Hdidpa)Cl_2][PF_6] (**6**).[68] The Zn-Cl bond distance afforded a value of 2.2696 (18) Å. The N-H···Cl angle of this complex is 172 (5)°.

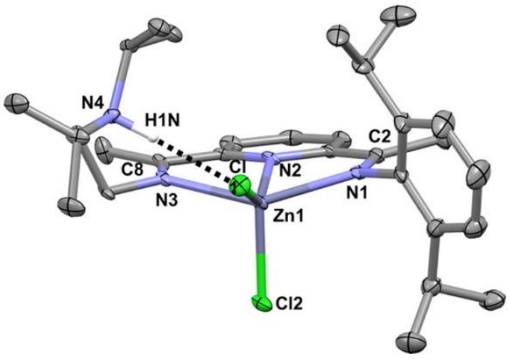

Figure 2.20. Solid-state structure of [Zn(Hdidpa)Cl_2][PF_6] (**6**) (30% probability) displaying the capability of the protonated pendant base to form intramolecular hydrogen bonds. Selected bond lengths (Å) and angles (deg): Zn(1)−Cl(1) 2.2696(18), Zn(1)−Cl(2) 2.2346(19), Zn(1)−N(1) 2.240(5), Zn(1)−N(2) 2.079(5), Zn(1)−N(3) 2.251(5), N4-(H1N) 0.99(6), Cl(1)···H(4N) 2.17(6), N(4)···Cl(1), 3.152(6), C(2)−N(1) 1.252(8), C(8)−N(3) 1.277(8), and Cl(1), Zn(1)Cl(2) 113.45(7), N(2) Zn(1)Cl(1) 143.89(15), N(1) Zn(1)N(3) 143.1(2), and N(4)-H(1N)···Cl(1) 172(5).

Table 2.2. Parameters for weak, medium, and strong H-bonds.[48]

	Strong	Medium	Weak
H···X bond length (Å)	1.2- 1.5	1.5-2.22	>2.2
N···X bond distance (Å)	2.2- 2.5	2.5-3.2	>3.2
N-H···X bond angle (˚)	170-180	>130	>90

*X= Halide (Cl, Br, I, etc.)

To compare the intramolecular H-bonding strength, [Zn(Hdidpa)Br_2][PF_6] (**7**) was also synthesized in the same manner as **3**. Similar to [Zn(Hdidpa)Cl_2][PF_6], an NH stretch is not observed in the solid-state FTIR spectrum (Figure 2.21). The PF_6^- counterion from the synthesis is observed at 835 cm^{-1}.

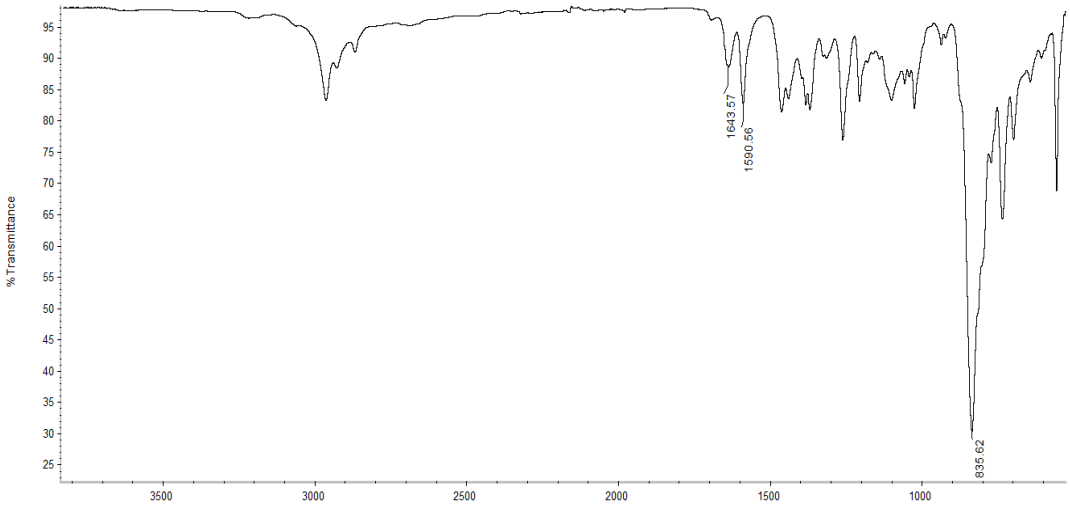

Figure 2.21. Solid-state FTIR spectrum of [Zn(Hdidpa)Br_2][PF_6] (**7**).

The complex, [Zn(Hdidpa)Br_2][PF_6], was characterized by ^{1}H NMR and the solid-state structure. The ^{1}H NMR spectrum (Figure 2.22), analogous to **6**, [Zn(Hdidpa)Br_2][PF_6] (**7**) illustrates an N-H bond resonance shifted downfield. The resonance is found to be at 7.78 ppm as opposed to 8.50 ppm in[Zn(Hdidpa)Cl_2][PF_6]. This difference suggests a weaker intramolecular H-bond interaction in [Zn(Hdidpa)Br_2][PF_6] (**7**).

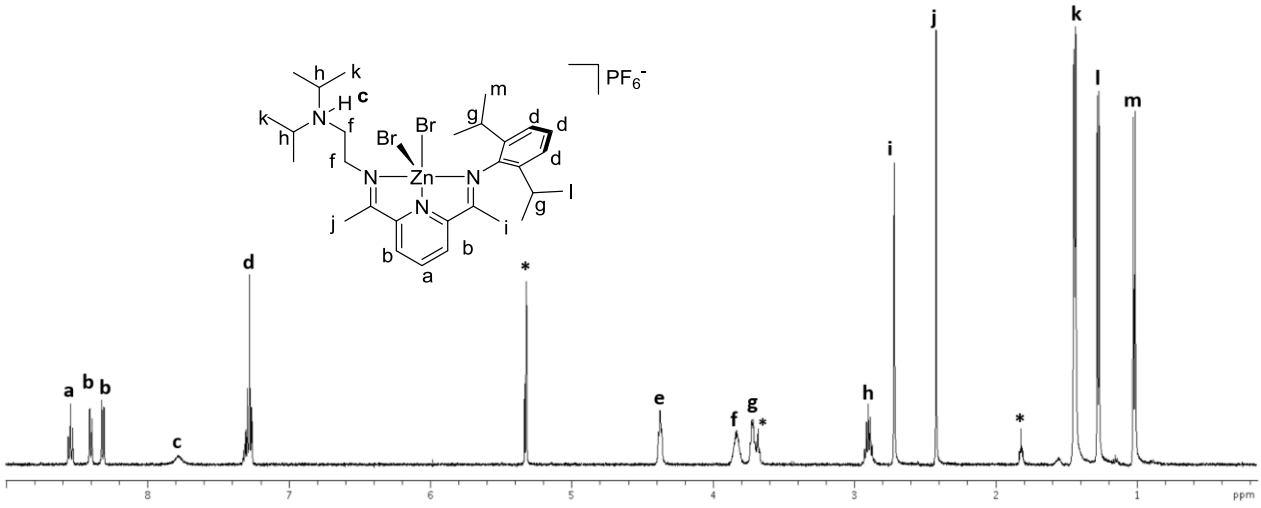

Figure 2.22. ^{1}H NMR of [Zn(Hdidpa)Br_2][PF_6] (**7**) (500 MHz, CD_2Cl_2) (*represents solvent).

In comparison to [Zn(Hdidpa)Cl_2][PF_6], the solid-state structure of the [Zn(Hdidpa)Br_2][PF_6] shows an N-H···Br distance of 2.45(4) Å and the N···Br distance of 3.309 (3) Å (Figure 2.23). These bond distances are slightly longer than those seen in the [Zn(Hdidpa)Cl_2][PF_6] species, as expected due to a weaker H-bond interaction. The N-H···Br angle is 174 (3)°. This follows the trend of MHHB strength described by Sherwood who describes trend to be H-F<<H···Cl≤ H···Br< H···I, with H-F being the shortest bond length.[52] Again, it is observed that the NH group of the pendant arm is directed toward Br^- as we saw in the [Zn(Hdidpa)Br_2][PF_6]**.**

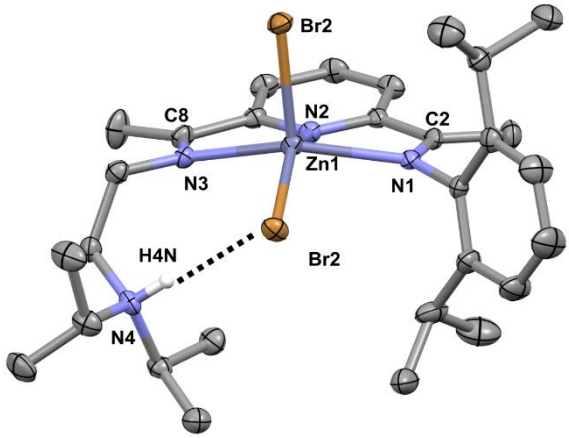

Figure 2.23. Solid-state structure of [Zn(Hdidpa)Br_2][PF_6] (**7**) (30% probability). Selected bond lengths (Å) and angles (deg): Zn(1)-N(2) 2.081(3), Zn(1)-N(3) 2.270(3), Zn(1)-Br(2) 2.3746(7), Zn(1)-Br(1) 2.3992(6), Zn(1)-N(1) 2.233(3), N(1)-C(2) 1.283(5), N(2)-C(7) 1.332(5), N(3)-C(8) 1.277(5), C(2)-C(3) 1.495(5), C(7)-C(8) 1.499(6), N(4)-H(1N) 0.86(4), N(4)-H(1N)…Br(1) 2.45(4), N(4)...Br(1) 3.309(3), N(2)-Zn(1)-Br(2) 145.94(9), N(2)-Zn(1)-Br(1) 100.81(9), N(3)-Zn(1)-Br(1) 98.02(8), Br(2)-Zn(1)-Br(1) 113.17(3), N(3)-Zn(1)-N(1) 143.06(12), N(4)-H(1N)-Br(1) 174(3).

The protonated Fe(II) analogue was synthesized similarly to the protonated Zn(II) complexes. Complex **5** was dissolved in methylene chloride and added to a MeOH solution of NH_4PF_6 (Eq. 2.8). The solution stirred for one day and was filtered through a celite plug. Purple crystals identified as [Fe(Hdidpa)Cl_2][PF_6] (**8**) were obtained upon layering the DCM solution with diethyl ether and leaving for one week in the freezer at -10° C.

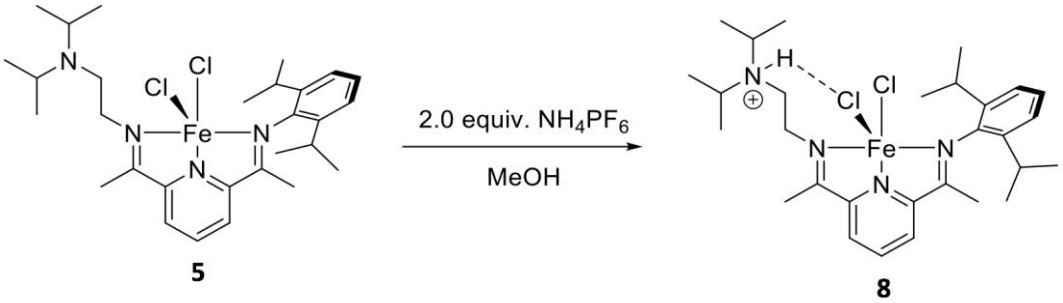

(2.8)

The solid-state FTIR spectrum of **8** illustrates a stretch at 1622 cm^{-1} and 1582 cm^{-1} from the imine bonds in this complex (Figure 2.24). However, again no NH stretch is observed in the spectrum due to

intramolecular H-bonding interactions. The lack of an NH stretch in the FTIR spectrum has also been observed in other Fe(II) didpa complexes.[39]

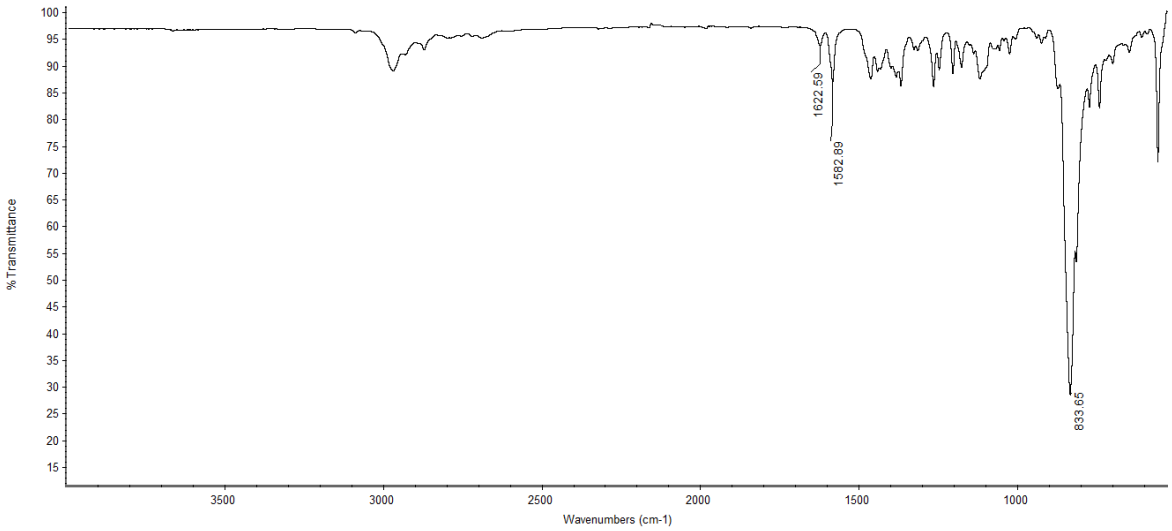

Figure 2.24. Solid-state FTIR spectrum of $[Fe(Hdidpa)Cl_2][PF_6]$ (**8**).

The paramagnetic nature of complex **8** resulted in a ^1H NMR spanning a much larger window in comparison to diamagnetic species (Figure S6). In order to confirm the synthesis of $[Fe(Hdidpa)Cl_2][PF_6]$ (**8**), the solid-state structure was obtained (Figure 2.25). The solid-state structure reveals a five-coordinate iron center with a distorted square pyramidal geometry ($\tau = 0.06$). The measured value of the μ_{eff} is 4.8 μ_B in the solid state and 4.7 μ_B in solution. Again, we observe the NH group facing the Cl^- group as was observed in both the $[Zn(Hdidpa)Cl_2][PF_6]$ (**6**) and $[Zn(Hdidpa)Br_2][PF_6]$ (**7**). The Mössbauer spectrum of **8** further confirms an iron(II) metal center (Figure 2.25). The Mössbauer room-temperature parameters include an isomer shift of 0.863(4) mm/s and a ΔE_Q of 1.933(8)mm/s (Table 2.1).

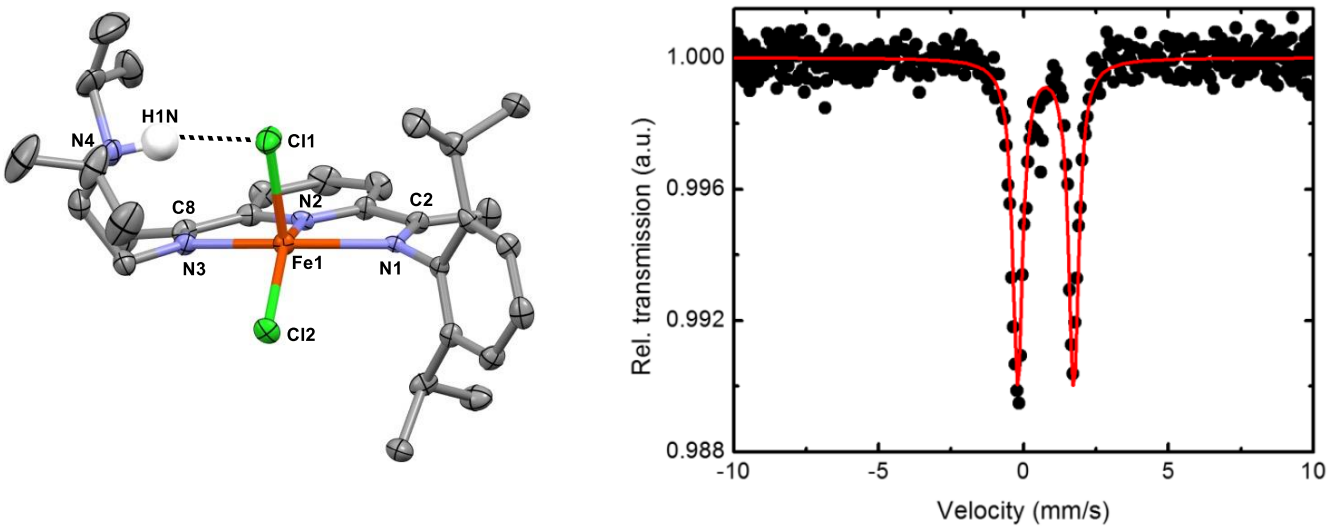

Figure 2.25. Solid-state structure of [Fe(Hdidpa)Cl_2][PF_6] (**8**) with PF_6^- omitted for clarity, displaying a MHHB (left) and room-temperature zero-field ^{57}Fe Mössbauer spectrum of [Fe(Hdidpa)Cl_2][PF_6] (**8**) (right); [δ = 0.863(4) mm/s and a ΔE_Q of 1.933(8)]. Selected bond lengths (Å) and angles (deg): Fe(1)−Cl(1) 2.327(2), Fe(1)−Cl(2) 2.263(2), Fe(1)−N(1) 2.225(6), Fe(1)−N(2) 2.102(5), Fe(1)−N(3) 2.215(7), N4- (H4N) 1.00(2), Cl(1)···H(4N) 2.18(3), N(4)···Cl(1) 3.157(8), C(2)−N(1) 1.282(8), C(8)−N(3) 1.283(9), and Cl(1)Fe(1)Cl(2) 111.94(9), N(2)Fe(1)Cl(2) 142.54(17), N(1)Fe(1)N(3) 146.1(2), and N(4)-H(4N)···Cl(1) 166(10).

2.4 Reduction of Fe(didpa)Cl_2

In order to study the relationship between the ligand-based redox activity of the primary sphere and the protonation state of the secondary coordination sphere, the Fe(II) analogue was synthesized. Due to the redox inactivity of the Zn(II) metal center, the redox active Fe(II) center is needed to study this relationship. The dichloride compound, **5**, can be reduced with NaHg amalgam under CO to make the carbonyl compound, Fe(didpa)$(CO)_2$ (**9**). A Fischer-Porter tube was pressurized with 20 psi of CO and left to stir vigorously overnight (Eq. 2.9). Dark green crystals of Fe(didpa)$(CO)_2$ (**9**) were obtained by slow ether evaporation of a filtered ether solution.

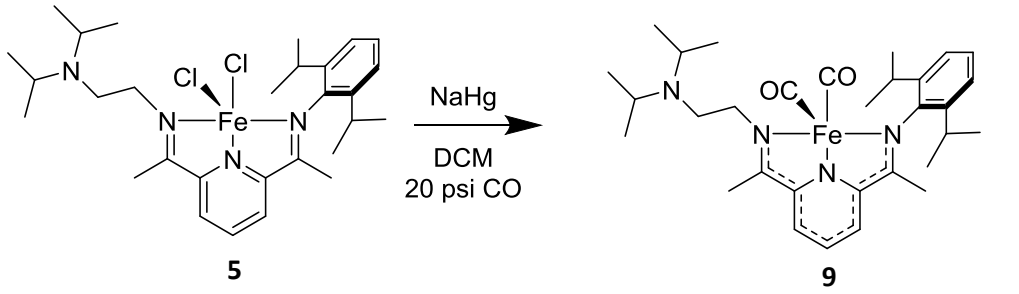

5 **9** **(2.9)**

The dashed line in the ChemDraw representation of Fe(didpa)$(CO)_2$ represents reduction of the PDI ligand is reduced by two electrons which are delocalized throughout the backbone ligand.

The FTIR spectrum (Figure 2.26) of this complex shows two stretching frequencies at 1940 cm^{-1} and 1871 cm^{-1}, corresponding to the carbonyl ligands present in the synthesized complex.

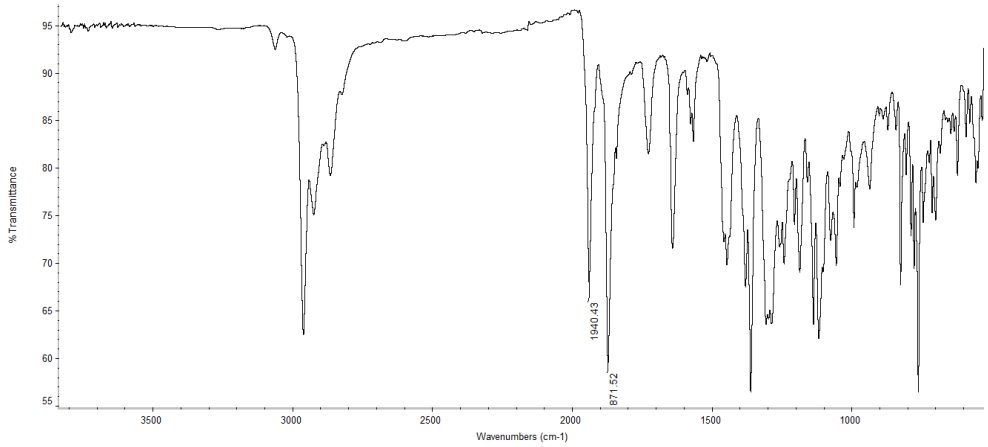

Figure 2.26. Solid-state FTIR spectrum of Fe(didpa)$(CO)_2$ (**9**) displaying the CO stretches.

The ^{1}H NMR spectrum of the diamagnetic complex, Fe(didpa)$(CO)_2$, confirms the synthesis of this complex (Figure 2.27). The two triplets found at 4.25 ppm and 2.88 ppm integrate for the four protons of the ethylene bridge. There is a septet at 3.10 ppm integrating for the two protons of the diisopropylamine didpa arm. Another septet is also observed at 2.51 corresponding to the two protons of the diisopropyl of the aryl group. The ^{13}C NMR of Fe(didpa)$(CO)_2$ (**9**) was also obtained to further confirm the presence of

the CO ligands (Figure S7) displayed at 214 ppm, consistent with the resonances observed in other $Fe(CO)_2$ PDI complexes.[57,58]

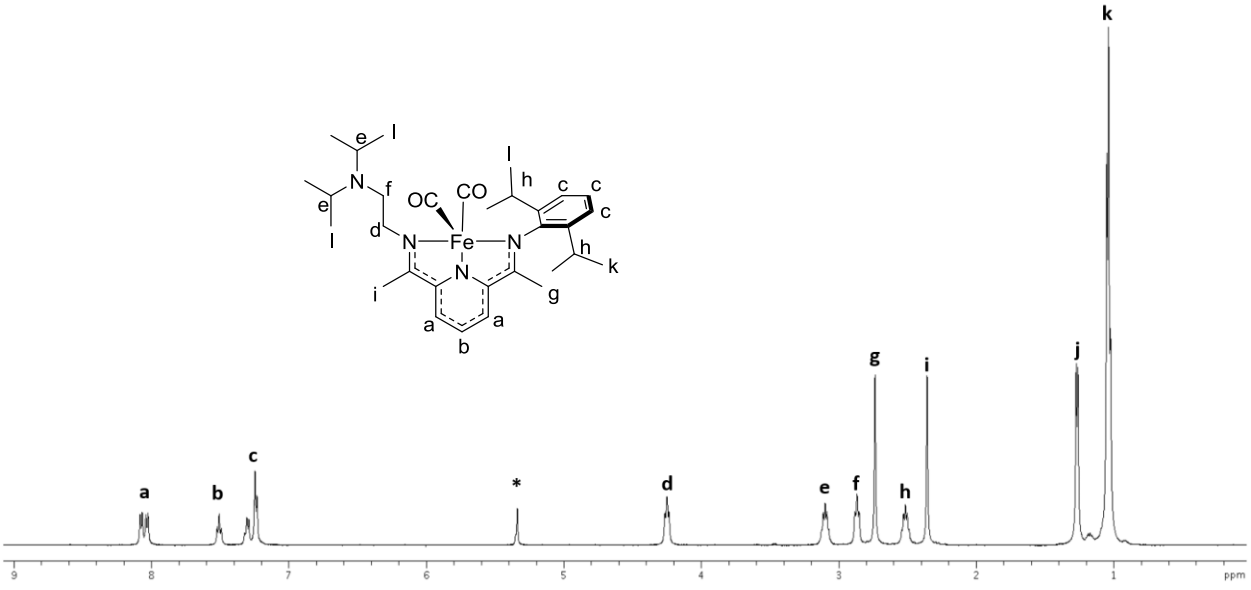

Figure 2.27. ^{1}H NMR spectrum of $Fe(didpa)(CO)_2$ (**9**).

The solid-state structure of $Fe(didpa)(CO)_2$ (**9**) (Figure 2.28) shows the C=N imine double bonds are elongated from 1.283(5) and 1.280(6) Å in the dichloride species to 1.3330(7) and 1.329(7) Å in the $Fe(didpa)(CO)_2$ (**9**). To confirm the oxidation state of the iron center, the room temperature Mössbauer spectrum was analyzed (Figure 2.28). Based on the Mössbauer parameters of **9** (ΔE_Q= 1.43, δ= -0.06 mm/s) along with the C_{imine}-N_{imine} bond lengths, it was determined that the metal center is Fe(II) with a doubly reduced PDI ligand.

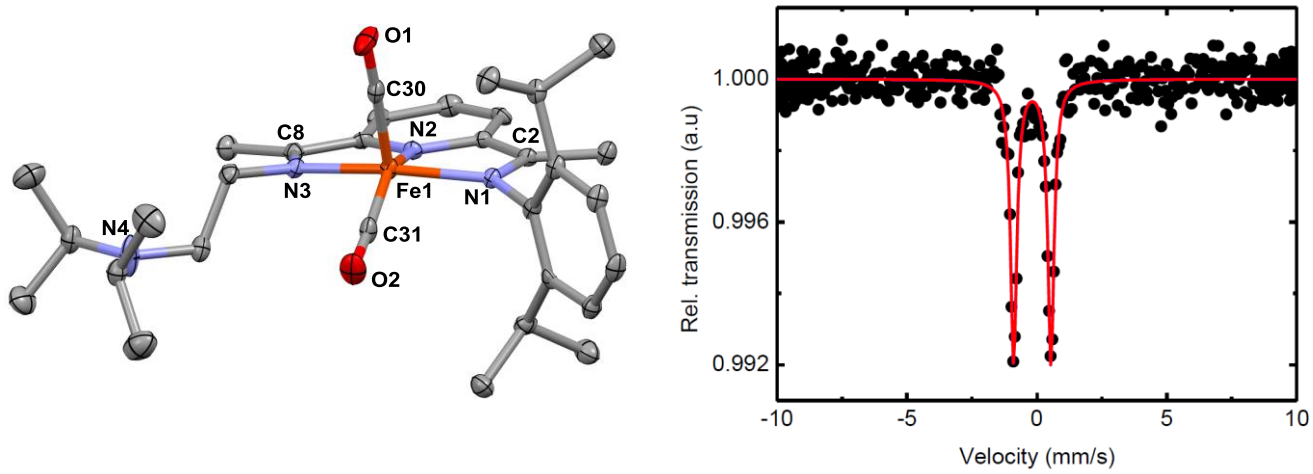

Figure 2.28. Solid-state structure of Fe(didpa)$(CO)_2$ (**9**) (30% probability) (left) and room-temperature zero-field ^{57}Fe Mössbauer spectrum (right) of Fe(didpa)$(CO)_2$ (**9**) [ΔE_Q= 1.43, δ= -0.06 mm/s]. Selected bond lengths (Å) and angles (deg): Fe(1)−C(31) 1.774(6), Fe(1)−C(30) 1.788(7), Fe(1)−N(1) 1.961(5), Fe(1)−N(2) 1.846(4), Fe(1)−N(3) 1.960(5), C(2)−N(1) 1.330(7), C(8)−N(3) 1.329(7), and C(31)Fe(1)C(30) 98.9(3), N(2)Fe(1)C(31) 149.2(3), and N(1)Fe(1)N(3) 156.99(19).

2.5 Protonation of the Reduced Fe(II) PDI Complex

The Fe(didpa)$(CO)_2$ complex can be protonated similarly to Fe(didpa)Cl_2 (**5**) in order to study the relationship between the protonation state of the base and the redox activity of the iron center. A solution of ammonium hexafluorophosphate in CH_3OH was introduced to a solution of [Fe(didpa)$(CO)_2$] in DCM and left to stir for one day (Eq. 2.10). Careful layering of the filtered DCM solution with diethyl ether yielded dark purple crystals identified as [Fe(Hdidpa)$(CO)_2$][PF_6] (**10**).

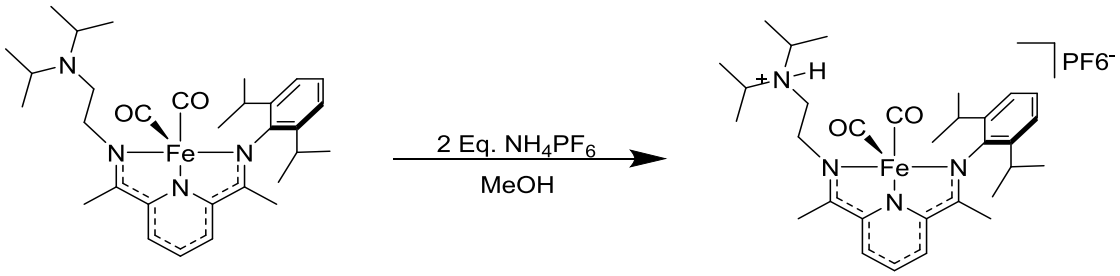

9 **10** **(2.10)**

The solid-state FTIR spectrum illustrates the CO stretches at 1945 cm^{-1} and 1879 cm^{-1} (Figure 2.29). The PF_6^- counterion is displayed at 831 cm^{-1}.

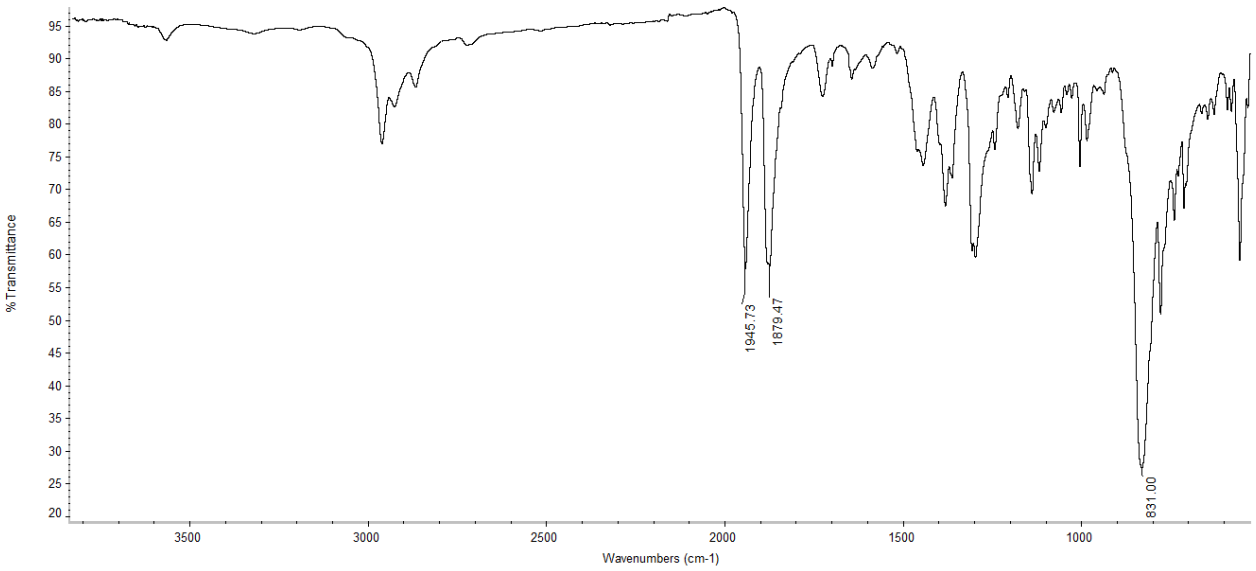

Figure 2.29. Solid-state FTIR spectrum of $[Fe(Hdidpa)(CO)_2][PF_6]$ (**10**).

Although the FTIR spectrum lacks the N-H stretch, the ^{1}H NMR spectrum (Figure 2.30) shows the N-H resonance at 7.60 ppm. Upon protonation of the reduced species, we observe a few other changes in the NMR spectrum. A singlet is observed at 8.18ppm responsible for three protons of the aryl group. The ethylene bridge proton resonances are found at 4.65 ppm and 3.82 ppm. The septet from the two protons of the diisopropylamine pendant base are found within the multiplet at 2.51 ppm.

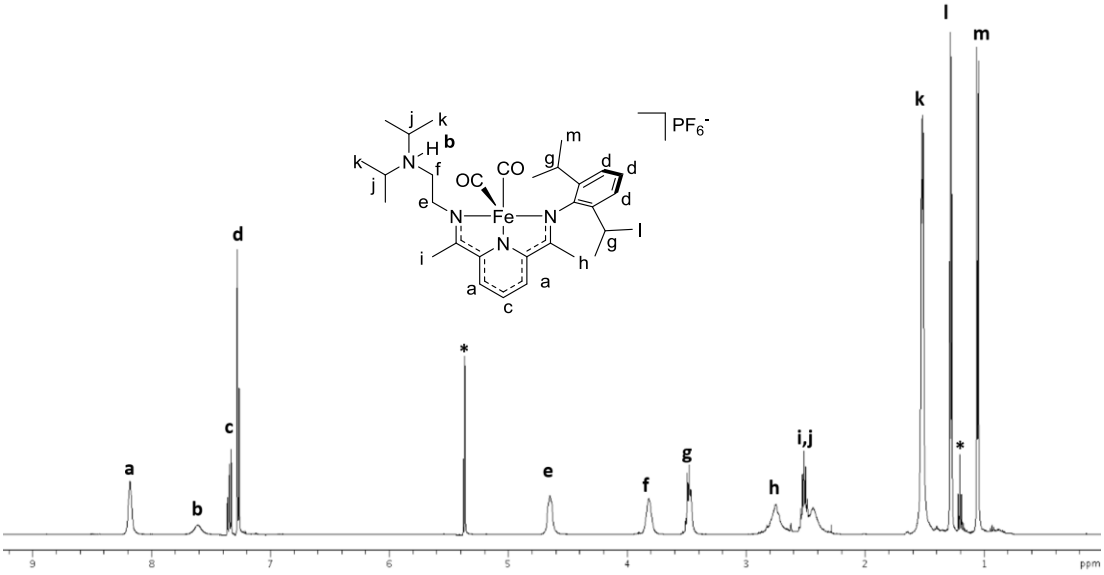

Figure 2.30. ^{1}H NMR spectrum of $[Fe(Hdidpa)(CO)_2][PF_6]$ (**10**).

The zero-field Mössbauer parameters of **10** (ΔE_Q= 1.435(8), δ= -0.075(5) mm/s) suggest the oxidation state remains Fe(II) as was observed in the unprotonated species. The solid-state structure (Figure 2.31) illustrates the protonated amine in the secondary coordination sphere. The solid–state structure reveals a five-coordinate Fe center with a square pyramidal geometry (τ = 0.12). The C_{imine}-N_{imine} bond lengths calculated suggest no change in oxidation state of the ligand upon protonation of the pendant amine.

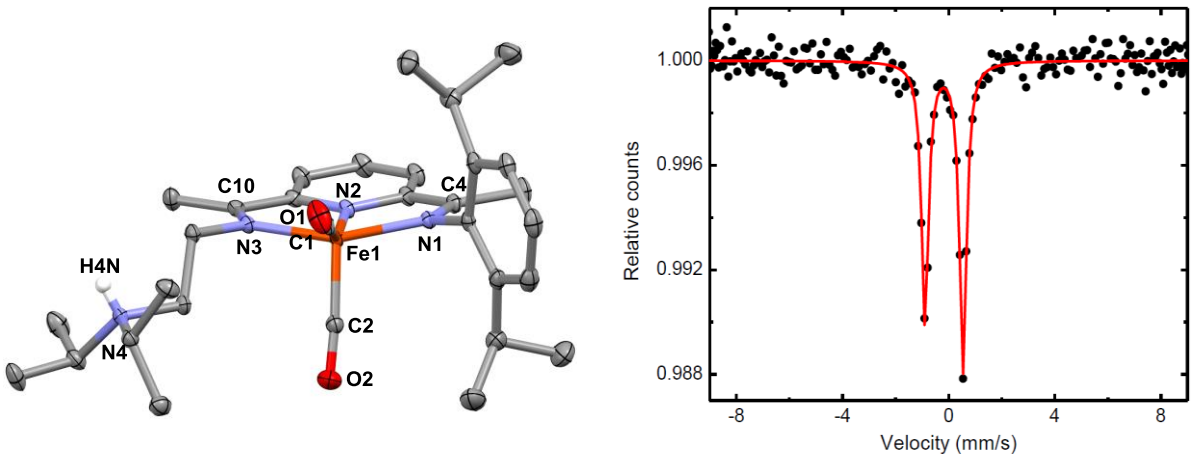

Figure 2.31. Solid-state structure (30% probability) (left) and the Mössbauer spectrum (right) of [Fe(Hdidpa)$(CO)_2$][PF_6] (**10**)**.** Only the H atom of the protonated diisopropylamine is shown, and the PF_6^- counterion is omitted for clarity. Selected bond lengths (Å) and angles (deg): Fe(1)−C(1) 1.779(2), Fe(1)−C(2) 1.7821(18), Fe(1)−N(1) 1.9617(15), Fe(1)−N(2) 1.8452(15), Fe(1)−N(3) 1.9461(16), N4-(H4N) 0.74(3), C(4)−N(1) 1.317(2), C(10)−N(3) 1.329(3), and C(1)Fe(1)C(2) 94.29(9), N(2)Fe(1)C(1) 151.19(8), and N(1)Fe(1)N(3) 154.70(6).

2.6. Electrochemistry of Fe(II) PDI Complexes

As previously discussed, the redox activity of iron complexes can be influenced by the secondary coordination sphere. In order to investigate the relationship between the redox activity and alterations made in the secondary coordination sphere, the cyclic voltammograms of complex **9** and **10** were analyzed (Figure 2.32).

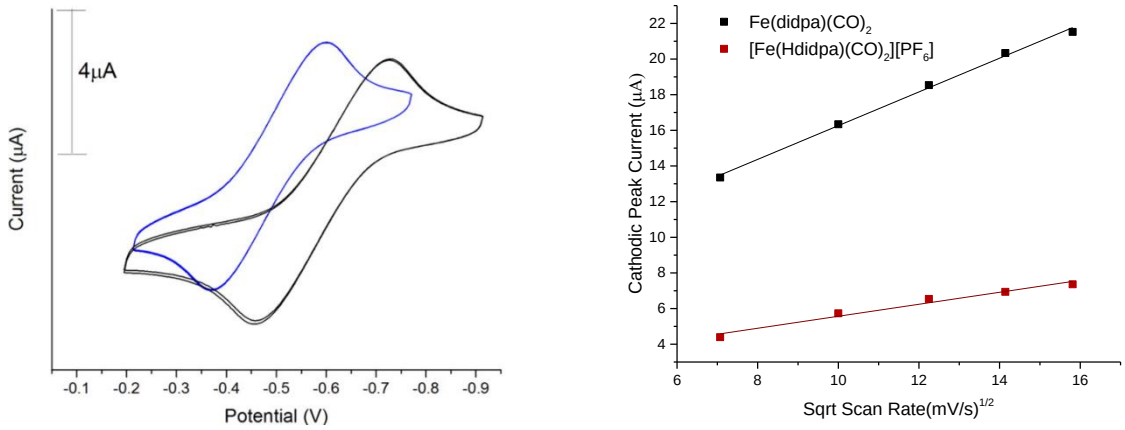

Figure 2.32. Left: Cyclic voltammogram of 0.005 M Fe(didpa)$(CO)_2$ (**9**) (black line) and 0.010 M $[Fe(Hdidpa)(CO)_2][PF_6]$ (**10**) (blue line); 0.1 M $[(^nBu)_4N][PF_6]$ in DCM, 200 mV/s scan rate. Right: Plot of $E_{cathodic}$ peak current versus square root of the scan rate for Fe(didpa)$(CO)_2$ (**9**) (black) and $[Fe(Hdidpa)(CO)_2][PF_6]$ (**10**) (red) shows a linear correlation, to confirm the quasi-reversible process in CH_2Cl_2.

Previous studies have shown that the one electron oxidation involves the redox-active PDI ligand as opposed to the metal center.[56-58] The PDI ligand scaffold forms $[FePDI(CO)_2]^+$ via the quasi-reversible one electron oxidation. The cyclic voltammograms of **9** and **10** display the quasi-reversible one electron oxidation of the PDI ligand platform expected (Figure 2.32, above). The neutral form, complex **9**, showed the oxidation event at $E_{1/2}$= -0.590 V vs. ferrocene. Protonation of the pendant amine in the secondary coordination sphere shifts the event to $E_{1/2}$= -0.485 V vs. ferrocene, a difference of 105 mV. This suggests that the ligand is more difficult to oxidize once the pendant arm is protonated. However, typical shifts upon protonation of different metal complexes where the ligand is directly bound to the metal center tends to be around a 500 mV shift.[68,69] Overall, the electrochemical data indicates very little change in the reduction potential upon protonation of the PDI ligand scaffold, making this system a suitable system for chemical transformations requiring the use of both protons and electrons.

In addition to exploring the relationship between the protonation state and redox activity, it was also necessary to determine how protonation of the secondary coordination sphere affected the basicity of the diisopropylamine. The pK_a of **10** was measured, yielding a value of 19.2 in acetonitrile. The pK_a value

is relatively close to that of Hünig's base (pK_a= 18.8) which suggests that the presence of the ethylene bridge prevents a wild deviation in the basicity of the pendant amine. The results of both the electrochemistry as well as the pK_a determination indicated no change in the oxidation state upon protonation in the secondary coordination sphere. This was further confirmed by the C_{imine}-N_{imine} bond lengths, Mössbauer parameters, and CO stretches (Table 2.3). This means that adding a proton to a highly reduced species has left it essentially unchanged, inconsistent with the redox behavior observed in other systems, such as Mayer's, which experience ~500 mV shift upon protonation.[53]

Table 2.3. Spectroscopic and electrochemical data of **5** and **7**.

PDI complex	Isomer shift (δ) [mm/s]	Quadropole splitting (ΔE_Q) [mm/s]	C_{imine}-N_{imine} (Å)	V_{CO} (cm^{-1})
$Fe(didpa)(CO)_2$	−0.061	1.43	1.329 (3), 1.330 (7)	1940, 1871
$[Fe(Hdidpa)(CO_2][PF_6]$	-0.075(5)	1.435(8)	1.329 (3), 1.317 (2)	1945, 1879

2.7. Hydrogen Bonding in Solution

Intramolecular hydrogen bonding in $[Zn(Hdidpa)Cl_2][PF_6]$ (**6**)**,** $[Zn(Hdidpa)Br_2][PF_6]$ (**7**) and $[Fe(Hdidpa)Cl_2][PF_6]$ (**8**), and $[Fe(Hdidpa)(CO)_2][PF_6]$ (**10**) were observed through the solid-state structures. However, it was necessary to investigate the intramolecular H-bonding in solution. It was also important to study how the environment around the metal center was altered upon binding and protonation of the pendant amine. In order to establish an understanding of how the basicity changes upon binding to the complex, the pK_a of the pendant diisopropylamine in the didpa ligand was determined. The pK_a values of $Zn(didpa)Cl_2$ were determined by establishing equilibria with a base of a known pKa, triethylamine. These experiments were performed in acetonitrile solutions and monitored by NMR spectroscopy. The pendant amine of the unprotonated species was measured to be 18.4, while the pK_a of Hünigs base is 18.8. This means that the basicity of the diisopropylamine is not altered upon binding. The pK_a did not change in the

didpa complex perhaps due to the ethylene bridge serving as an insulator from the metal. The PDI ligand does not affect the pK_a of the pendant amine which differentiates the PDI from other systems.[70]

In the solid state, we observed a metal halogen hydrogen bond (MHHB) in $[Zn(Hdidpa)Cl_2][PF_6]$ (**6**) and $[Zn(Hdidpa)Br_2][PF_6]$ (**7**). In order to show the hydrogen bonding interaction of $[Zn(Hdidpa)X_2]^+$ (where X= Cl^- or Br^-) species in solution, analysis by NMR spectroscopy was performed. The N-H resonances of both **6** and **7** are shifted downfield to the aromatic region. The downfield shift is representative of the presence of an intramolecular hydrogen bond in the system.[44a,71-73] Since Cl is more electronegative than Br, the proton resonances in **6** are more deshielded than those in **7**. Therefore the N-H resonance for $[Zn(Hdidpa)Cl_2][PF_6]$ (**6**) is further downfield than that of $[Zn(Hdidpa)Br_2][PF_6]$ (**7**) which is expected due to the weaker MHHB interaction from the bromide. The results from the NMR experiment confirm that in solution, the H-bonds are intact. In order to investigate the strength of the H-bond in each of the $[Zn(Hdidpa)Cl_2][PF_6]$ (**6**) and $[Zn(Hdidpa)Br_2][PF_6]$ (**7**), it was necessary to try and break that H-bond. One way to accomplish this is to titrate in a better H-bond acceptor that will interact with that H-bond more favorably the MHHB. The three solvents used to probe the H-bond of these complexes included acetone, DMF, and DMSO. Using the Beta scale of hydrogen bonding ability (HBA), basicities determined by solvatochromatic comparison method, DMSO exhibited the most H-bonding ability (Table 2.4).[74] Upon titration of each solvent, the N-H resonance was monitored. Acetone had the smallest chemical shift in the ^1H NMR, correlating well with its H-bond accepting ability. As expected, there is a clear shift observed when the complexes are titrated with DMF and DMSO. The binding isotherms for all three solvents correlate well based on the H-bonding ability of these solvents (Figure 2.33, Table 2.4).[75]

Table 2.4. Solvents with their H-bond accepting abilities.

Solvent	H-bond accepting ability (β)
DMF-d_7	0.69
DMSO-d_6	0.76
Acetone-d_6	0.43

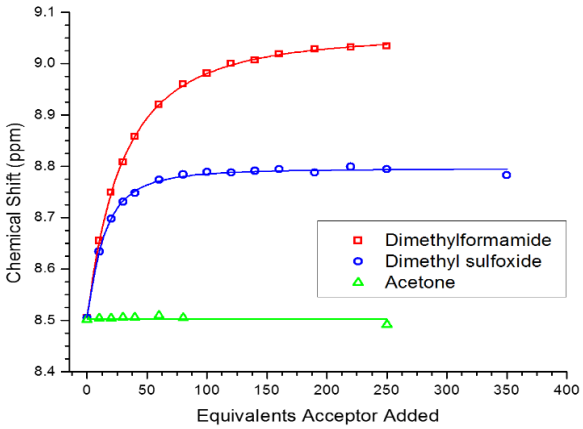

Figure 2.33. Left: Binding isotherms of the ^{1}H NMR titrations of **6** with deuterated solvents of different H-bond accepting strength.

As seen from the binding isotherms, there is a large downfield shift of the N-H resonance in DMF and DMSO, but no shift when there is an addition of acetone. The large chemical shift of the N-H resonance upon titration with DMSO can be observed in the NMR spectrum (Figure 2.34).

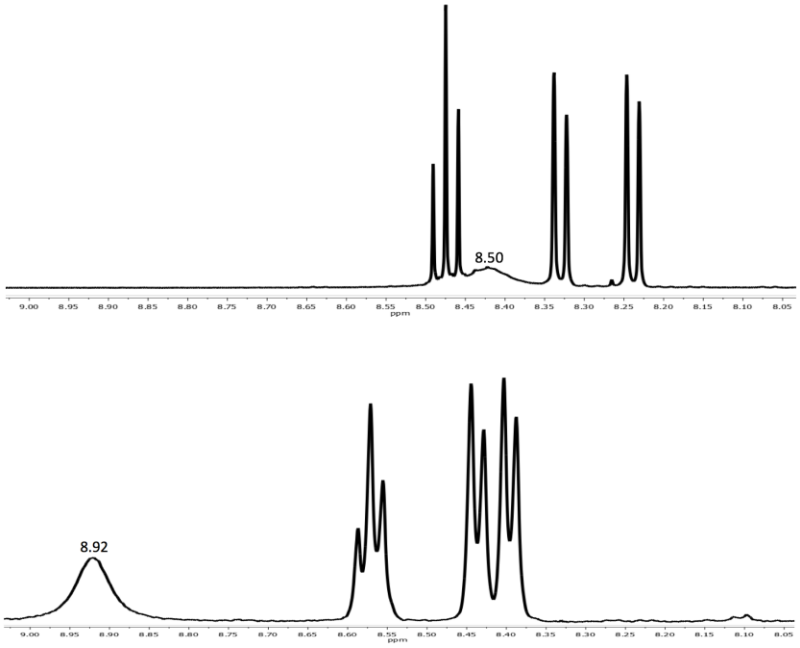

Figure 2.34. ^{1}H NMR chemical shift of Zn(didpa)Cl_2 (**6**) in CD_2Cl_2 (top) and upon addition of DMF-d_7 (bottom), illustrating the shift in the N-H resonance.

Since the Zn(didpa)Br_2 is expected to have a weaker intramolecular H-bond, the strength of the H-bond in solution was also analyzed through a series of titrations. Similar to [Zn(Hdidpa)Cl_2][PF_6] (**6**), a large shift was noted for the N-H resonance upon addition of DMF and DMSO (Figure 2.35). However, unlike [Zn(Hdidpa)Cl_2][PF_6], a small shift of the N-H resonance was also observed with the introduction of acetone likely as a result of a weaker MHHB in [Zn(Hdidpa)Br_2][PF_6] (**7**). The weaker MHHB therefore allows interaction with poorer H-bond acceptors like acetone. Another feature to notice is that the shifts in the N-H resonance for DMF and DMSO are much larger than that of the [Zn(Hdidpa)Cl_2][PF_6] (**6**)**.** This larger shift highlights a larger hydrogen bond interaction because there is a weaker intramolecular interaction. From the titration experiments performed, the conclusion is that the bromide forms a weaker MHHB bond than chloride. The weak H-bond acceptor, acetone, showed a slight interaction in the bromide analogue due to a weaker intermolecular H-bond interaction. There is also a much larger interaction observed with the two other solutions for the same reason. These NMR titrations give us an

idea of how these intermolecular H-bonds behave in solution. However, in order to measure the interactions in solid state, the strength of the H-bond was determined by computational analysis.

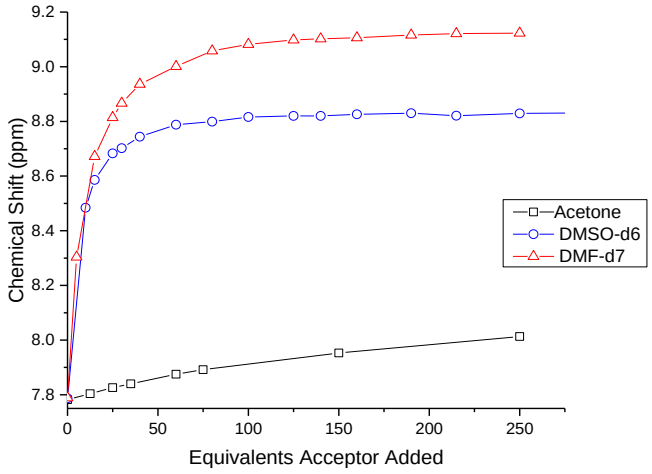

Figure 2.35. Binding isotherms of the titration of [Zn(Hdidpa)Br_2][PF_6] (**7**) with hydrogen bond acceptors acetone (black squares), DMSO (blue circles), and DMF (red triangles).

It is proposed that these MHHB get weaker going down the periodic table, and this trend was observed in [Zn(Hdidpa)Cl_2][PF_6] (**6**)and [Zn(Hdidpa)Br_2][PF_6] (**7**). To verify this, gas phase computational density functional theory (DFT) calculations were performed on both the [Zn(Hdidpa)Cl_2][PF_6] (**6**) and [Zn(Hdidpa)Br_2][PF_6] (**7**) complexes. Using the solid-state structure of [Zn(Hdidpa)Cl_2][PF_6] (**6**) as a starting basis, the energy of the H-bond in [Zn(Hdidpa)Cl_2][PF_6] (**6**) was calculated. The energy is calculated once again when the diisopropylamine group is rotated away, yielding a difference of 6 kcal/mol (Figure 2.36). In order to measure the H-bond strength in [Zn(Hdidpa)Br_2][PF_6] (**7**), this similar process was performed using DFT calculations and a smaller value is obtained (5 kcal/mol). These results further support the proposed trend which suggested that a weaker MHHB in [Zn(Hdidpa)Br_2][PF_6] (**7**) would be observed.

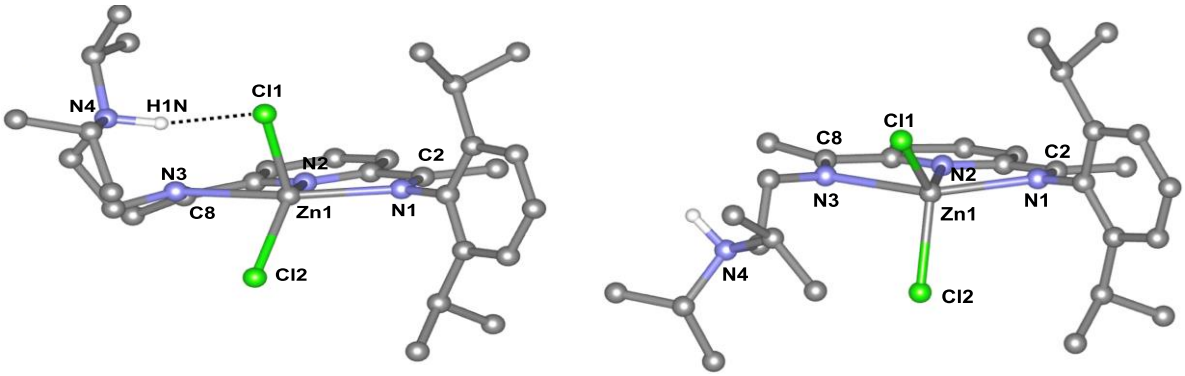

Figure 2.36. Computational DFT studies of $[Zn(Hdidpa)Cl_2][PF_6]$ (**6**) showing MHHB (left) and with the diisopropylamine group rotated (right).

2.8. Reactivity of Didpa with Hydrogen Sulfide

The didpa ligand was revealed to form intramolecular H-bonding within the secondary coordination in both solid state and in solution, providing stabilization of metal halogen hydrogen bonds (MMHBs) and other substrates. It was previously observed that the didpa scaffold allowed for the stabilization of an Fe-OH species through intramolecular hydrogen bonding.[39] In the neutral form, the didpa ligand can serve as an H-bond acceptor while the protonated form of the ligand can function as an H-bond donor (Figure 2.37).

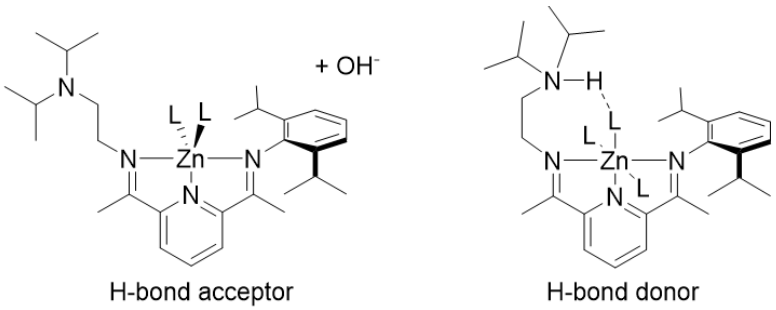

Figure 2.37. The didpa ligand scaffold acting as an H-bond acceptor (left) and an H-bond donor (right) which can use intramolecular H-bonding to stabilize substrates.

Systems containing hydrogen bond acceptors have been shown to aid in the stabilization of various substrates, such as hydrosulfide.[71-73] However, the synthesis of ligand systems containing H-bond acceptors remain rare and there is only a handful of stable hydrosulfide complexes that illustrate stabilization via secondary coordination sphere interactions. Some groups who have incorporated H-bond acceptors in their ligand design includes Borovik, Szymczak, and Fout.[38] Given that the neutral form of the

didpa ligand can serve as a hydrogen bond acceptor, didpa was an ideal candidate for stabilization of the SH bond.

The $[Zn(didpa)Cl_2SH]^-$ complex was synthesized upon addition of NBu_4SH in DCM or MeCN to a solution of $Zn(didpa)Cl_2$ (**10**) (Eq. 2.11).[76]

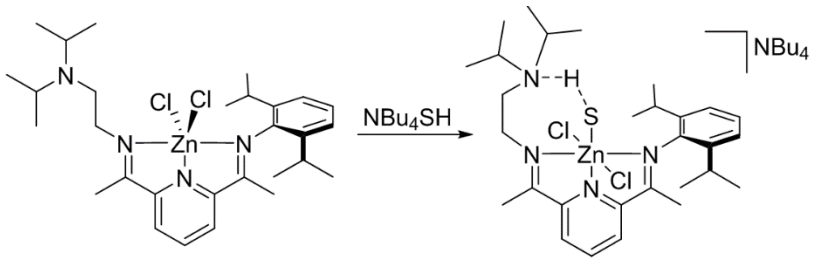

(2.11)

In order to determine the synthesis of the six-coordinate complex, the ^1H NMR was monitored upon addition of 1.5 equivalents of NBu_4SH (Figure 2.38). A significant change in the spectrum suggests that a reaction has occurred. There is a shift in the aromatic region of the spectrum due to a change in environment of the diisopropylphenyl group. There is also a shift in the diisopropyl protons from the pendant amine similar to the ^1H NMR spectrum of **6**. This is an indication that the diisopropylamine is locked into position due to being wrapped up in an H-bond.

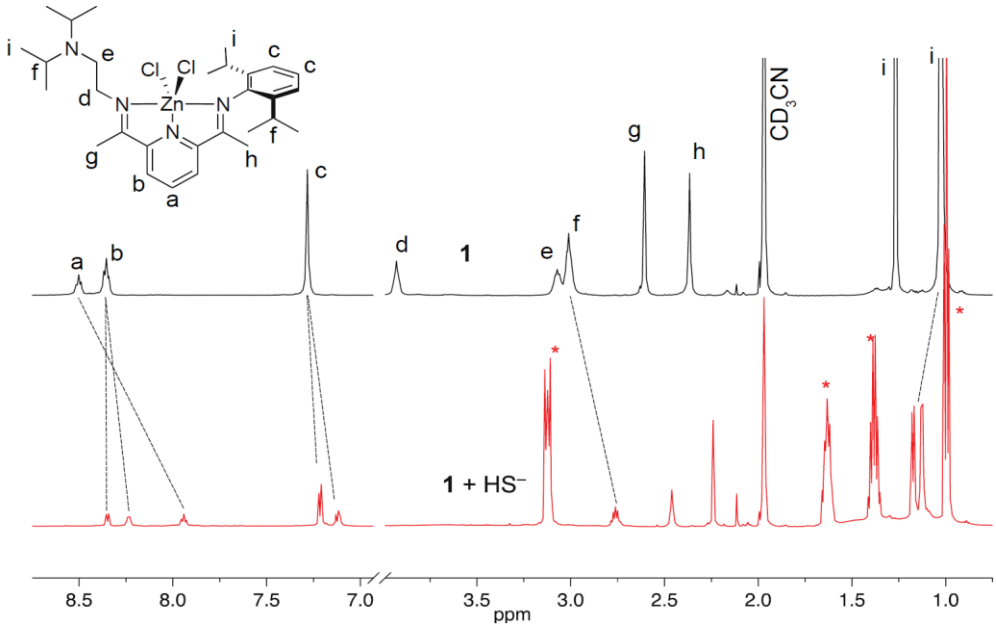

Figure 2.38. ^1H NMR spectra of $[Zn(didpa)Cl_2SH]^-$ before the addition of NBu_4SH (top, black) and after the addition of 1.5 equivalents of NBu_4SH (bottom, red).

In order to show the reactivity and coordination with HS^-, a UV-Vis titration was performed. The UV-Vis spectrum shows that upon addition of tetrabutylammonium hydrosulfide (NBu_4SH), we see a decrease in intensity at the 313 nm peak and a new peak growing in at 282 nm. The spectrum also illustrates an isosbestic point at 296 nm, suggesting that there are only two species in solution. The Job plot tells about the binding ratios and is consistent with a 1:1 binding of HS^- to the [Zn(didpa)Cl_2] complex. To further verify that the Zn is capable of binding another group, tetrabutylammonium hydroxide pentahydrate was added in 0.1 equivalent increments and a UV-Vis spectrum was obtained after each addition (Figure 2.39). Up to 3 equivalents were added to the Zn(didpa)Cl_2 solution. In order to analyze the binding activity of the hydroxide to the complex, a Job plot was obtained by analysis of UV-Vis. The didpa complex was introduced with tetramethylammonium hydroxide pentahydrate in MeCN at a total concentration of 413 µM.

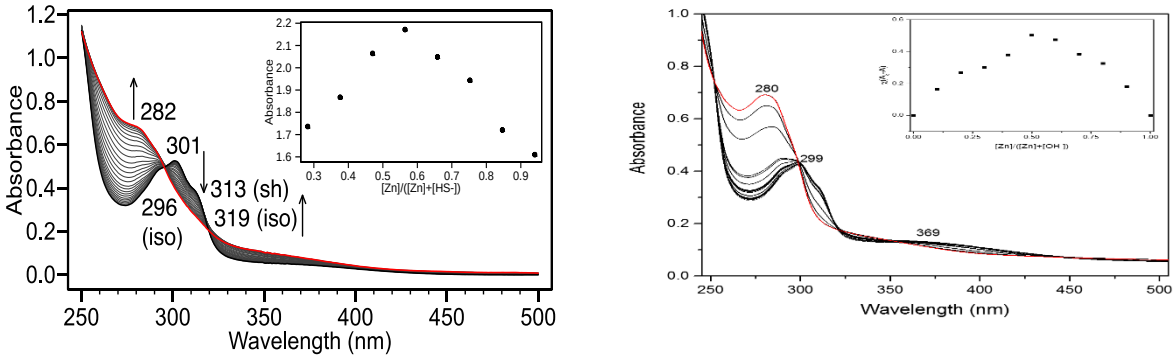

Figure 2.39. Left: Titration of Zn(didpa)Cl_2 (87.3 µM, CH_2Cl_2, black) with NBu_4SH (0.1 equiv. increments up to 6 equivalents, red). Inset: Job plot consistent with 1:1 binding; Right: Titration of Zn(didpa)Cl_2 (85.5 µM, CH_2Cl_2, black) with tetramethylammonium hydroxide pentahydrate). Inset: Job plot consistent with 1:1 binding.

Similarly, addition of OH^- yields a 1:1 binding after plotting the Job plot. It is proposed that the OH^- binds to the [Zn(didpa)Cl_2] complex, generating a six-coordinate zinc complex (Figure 2.40). To further support that a six-coordinate zinc complex is forming as opposed to a simple subsitution of the substrate, a titration with a chloride source was performed. In the same way, titration of Zn(didpa)Cl_2 with excess Cl^- was analyzed through UV-vis and exhibited the same behavior as in the case of titration with SH^- and OH^- (see Figure S24). A disappearance of one peak and growing in of the other which is proposed to be the six-coordinate Zn(II) species (Figure 2.39) is observed in the UV-Vis spectrum.

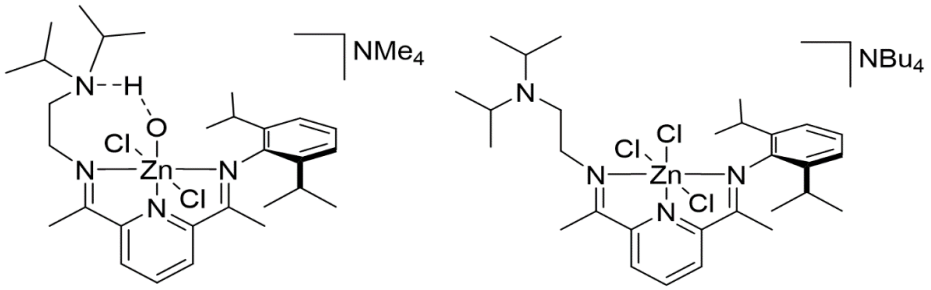

Figure 2.40. Proposed structures of the six-coordinate Zn(didpa) complexes upon addition of tetramethylammonium hydroxide pentahydrate (Me_4NOH) [left] and tetrabutylammonium chloride (NBu_4Cl) [right].

Unfortunately, no crystals were obtained despite the various use of chloride sources and solvent systems. Due to the reversibility of the process. In order to determine the stability of the [Zn(didpa)$Cl_2SH]^-$ complex, the ^{1}H NMR spectrum was interrogated. Low temperature NMR spectra were obtained in order to investigate the structural flexibility of the scaffold and the presence of the coordinated hydrosulfide (Figure S25, supporting information). As the sample is cooled, the HS resonance starts to appear in the ^{1}H NMR spectrum. Upon cooling the sample to -35 ˚C in CD_3CN, the HS resonance is shifted far downfield to 11.05 ppm, suggesting that there is an NH hydrogen bond present in the sample. This was a feature observed in ^{1}H NMR of the [Zn(Hdidpa)Cl_2][PF_6] complex as a result of H-bonding to the nitrogen from the pendant amine. This downfield shift observed was a result of the diisopropylamine serving as an H bond acceptor, accepting its H bond from the Zn-SH moiety. The ethylene bridge resonance at 3.6 ppm is

narrowed upon cooling the sample down. Similarly to complex **6**, an N-H stretch is not observed in the FTIR spectrum, commonly seen in many H-bonding systems.[28]

To confirm the requisite of an internal hydrogen bond in the complex, a previously sythesized zinc PDI complex containing no pendant base in the secondary coordination sphere was exposed to the same treatment as $[Zn(Hdidpa)Cl_2][PF_6]$ (**6**). Addition of 0.5 equivalents of NBu_4SH to the compound resulted in the formation of a white precipitate (Eq. 2.12). It was determined that the precipitate formed was zinc sulfide. Reaction of Bis-PDI with NBu_4SH shows decomposition, demonstrating the importance of the H-bond acceptor in the secondary coordination sphere for the stabilization of the zinc hydrosulfide complex.

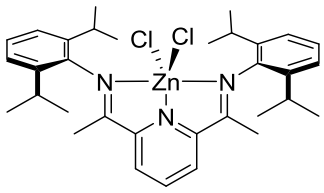

$\xrightarrow{NBu_4SH}$ Decomposition Products **(2.12)**

The synthesis of and characterization of various Fe(II) and Zn(II) complexes using the pyridinediimine ligand, didpa, have been utilized in order to probe the role of the secondary sphere. The intramolecular hydrogen bonding ability that the didpa ligand scaffold possesses has allowed us to explore the metal halogen hydrogen bonds (MHHBs) in zinc complexes, redox activity in iron complexes, and the stabilization of a six-coordinate zinc complex via H-bond acceptance. The MHHBs in $[Zn(Hdidpa)Cl_2][PF_6]$ (**6**)**,** $[Zn(Hdidpa)Br_2][PF_6]$ (**7**) and $[Fe(Hdidpa)Cl_2][PF_6]$ (**8**), and $[Fe(Hdidpa)(CO)_2][PF_6]$ (**10**) were determined by X-ray crystallography. The strength of the MHHBs were determined in both the solid-state as well as in solution. Additionally, the pK_a was determined to remain unaffected relative to the pK_a of Hünig's Base (pK_a=18.8). The redox activity of the didpa ligand was also explored using $Fe(didpa)(CO)_2$ (**9**) and $[Fe(Hdidpa)(CO)_2][PF_6]$ (**10**), resulting in a 105 mV upon protonation of the secondary coordination sphere. Given that the didpa ligand scaffold had the ability to stabilize MHHBs by use of an H-bond acceptor in the secondary coordination sphere, but can also function as an H-bond

donor in the neutral form, the zinc hydrosulfido complex was synthesized. Analysis of UV-Vis spectra for the six-coordinate zinc complexes was used to confirm the synthesis $[Zn(didpa)Cl_2SH]^-$ upon addition of NBu_4SH.

Chapter 3. Redox Inactive Metals

3.1 Incorporation of Redox Inactive Metals

The incorporation of various redox inactive metal ions is essential in many biological and biomimetic electron transfer reactions.[37,77] In nature, the utilization of a redox-inactive metal is demonstrated by the conversion of water to oxygen carried out by the oxygen evolving complex (OEC) in photosystem II.[36a] The redox inactive Ca ion is crucial for catalysis and without it, the OEC is virtually inactive.[36a,78] The calcium ion participates in the binding and activation of a water substrate, as well as the proton coupled electron transfer of the cluster. During this process, the OEC undergoes 4 electron transfer events which in turn leads to a high oxidation state manganese cluster. In this high oxidation state, the Mn cluster is able to promote O-O bond formation and release of O_2.[79]

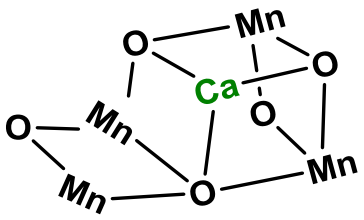

Figure 3.1. Depiction of the OEC, displaying the "cubane-like" structure of the Mn_4CaO_5 cluster.

In a non-biological setting, this is observed in the water oxidation catalyzed by heterogeneous cobalt and manganese oxides containing alkali or alkali earth metals.[80-83] These bio-inspired catalysts are responsible for water oxidation and mimics the cubane-like architecture recognized from the native oxygen evolving complex (OEC) active site. Redox inactive metals can also play a role in dioxygen activation[84], peroxide activation[85], H-H bond cleavage[86], O- and H- atom transfer[87], and alkane oxidation.[79, 88] Considering the participation of redox inactive metal ions in electron transfer reactions,

many synthetic models have been synthesized containing attributes that mimic those of the native OEC. Metal ions that can function as Lewis acids are often combined with redox active metals in order to promote a variety of reactions involving the transfer of electrons.[77a]

Borovik and coworkers have demonstrated that incorporating redox-inactive metal ions in the secondary coordination sphere of their Mn^{II} complex enhances the rates of O_2 reduction.[77a] Specifically, the presence of group 2 metal ions has allowed for this rate enhancement. The structural design of the the sulfonamido-based tripodal system contains SO_2AR groups acting as H-bond acceptors (Figure 3.2).[77a] The oxygen atoms of these SO_2AR groups are capable of binding group the redox-inactive metal ions in order to accelerate the dioxygen activation process. Similar to the native OEC, there is a dependence on the presence of redox-inactive metals for the rate of O_2 activation. It was noted that there an increase of Ca^{2+} and Ba^{2+} metal ions increased the initial rate.[77a]

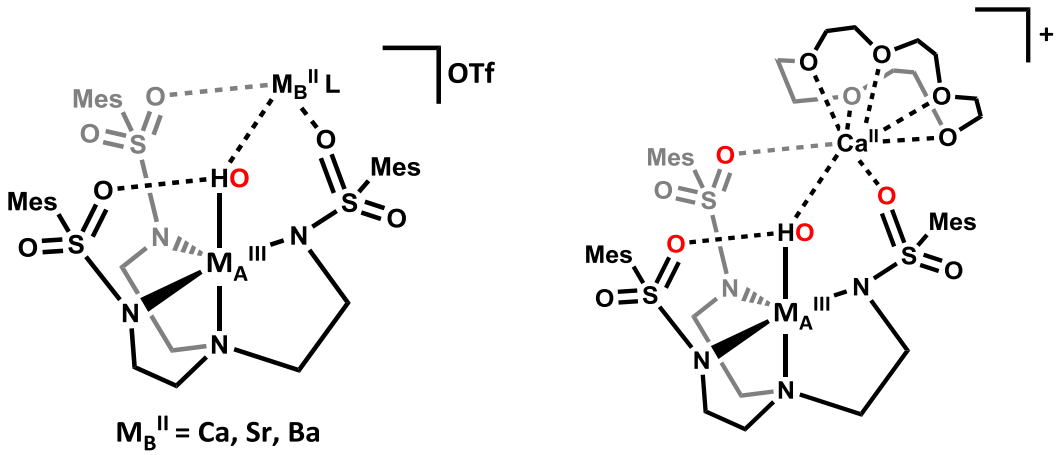

Figure 3.2. Structural construct of the tripodal ligands containing H-bond acceptors; sulfonamindo based tripodal system presenting a manganese center and a calcium ion in the secondary coordination sphere, similar to that of the OEC (right).[77a]

A way to control catalytic activity and selectivity is the use of non-covalent cation-crown interactions. Miller and coworkers were able to incorporate a redox inactive metal in their pincer scaffold containing an aza-crown ether moiety, which promotes cation reactivity near the active site of the metal ion (Figure 3.3). The cation is capable of tuning the chemical reactivity by aiding in the binding of low coordinate, reactive intermediates as well as offering a mechanistic pathway for catalysis acceleration through acid-promoted steps upon addition of the Lewis acid. The pincer crown ether ligand can act as a gate for substrate binding for catalytic reactions. The series of these iridium complexes with the ability to coordinate Lewis acidic metal cations can be used to explore small molecule activation.[86,90]

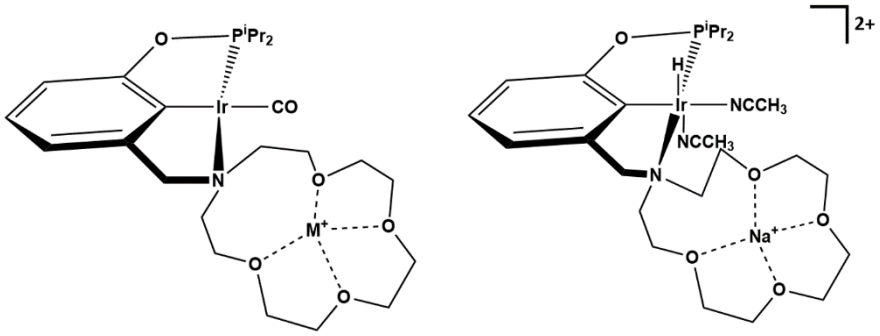

Figure 3.3. Iridium carbonyl complex containing an aza-crown ether macrocycle capable of cation-crown interactions (left) and pincer crown ligand scaffold with the addition of Na^+ to the system. [86,90]

As was discussed in Chapter one, Agapie and coworkers have synthesized heterometallic clusters in which a redox inactive metal ion can be incorporated in order to study the effect on the electronic properties of the complex.[77b,79] A series of high oxidation state tetranuclear-dioxido clusters and with varying redox inactive metal ions were investigated by cyclic voltammetry. Heterometallic mangansese-oxido clusters and heterometallic triiron-oxido clusters were synthesized in order to systematically investigate the redox potential of the complexes by varying the redox-inactive metal ions. The results of the electrochemical studies of these complexes showed that there was a linear correlation between the reduction potential and the pKa of the metal, suggesting the importance of metal ions in modulating the redox potential of the clusters.[37b]

Inspired by previously developed systems in which redox-inactive metals are incorporated, our group wanted to merge the idea of Lewis acids in the secondary coordination sphere in conjunction with the redox-active PDI scaffolds in order to modulate the redox activity of the system. By appending a crown ether in the secondary coordination sphere, we are able to chelate a redox-inactive metal ion (Lewis acid) in the cavity of a pendant 15-crown-5 (Figure 3.4).[91] The effect that the encapsulated alkali metal ions (Na^+ and Li^+) have on the redox active Fe(PDI) system was explored.[91]

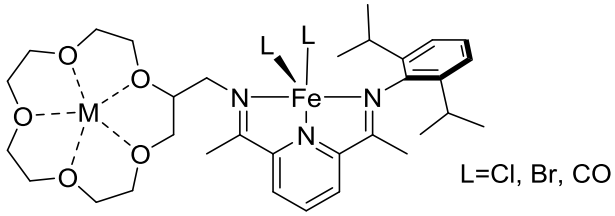

Figure 3.4. Fe^{II} PDI complex capable of chelating a redox inactive metals in the crown ether (M= Na^+, Li^+).

3.2 Synthesis of ^{15c5}PDI Complexes

The asymmetric PDI ligand [(ArN=C(CH_3))C_2H_3N((CH_3)C=O] and $FeCl_2$ were dissolved in approximately 20 mL of ethanol into a 100 mL round bottom Schlenk flask with a stir bar. The solution was heated to 80 °C for 15 min under N_2 gas and stirred. A solution of 2-aminomethyl-15-crown-5 in 10 mL of ethanol was slowly syringed into the flask and the solution was heated for 12 h under N_2 gas (Eq. 3.1). The solvent was removed *in vacuo* and a dark blue solid was obtained. Back in the glovebox, the resulting solid was redissolved in 5 mL of CH_2Cl_2 and filtered through Celite into a 20-mL scintillation vial. The filtrate was layered with pentane and set aside to allow for crystallization. Blue crystals identified as Fe(^{15c5}PDI)Cl_2 (**11**) were isolated.

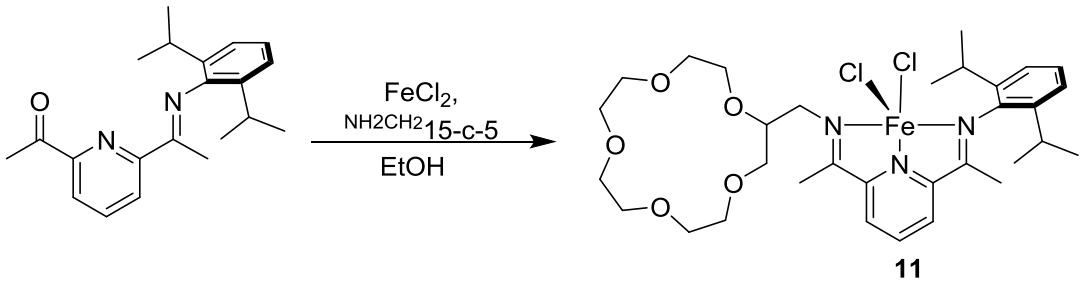

11

(3.1)

The solid-state structure was mostly unresolvable due to severe disorder in the 15-c-5, however, the general view of the preliminary structure (Figure 3.5) shows that the Fe center is five-coordinate.

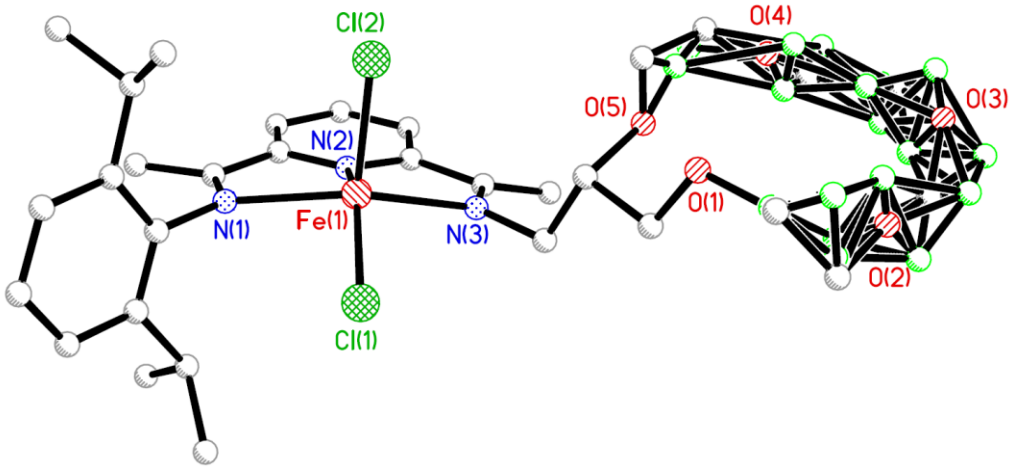

Figure 3.5. General view of complex Fe(^{15c5}PDI)Cl_2 (**11**), illustrating the disorder from the 15-c-5.

The Mössbauer parameters obtained included the quadrupole splitting (ΔE_Q) and isomer shift (δ), 0.949 (8) mm/s and 0.824 (5) mm/s respectively. These Mössbauer parameters confirm the high spin Fe^{II} center (Figure 3. 6).[92]

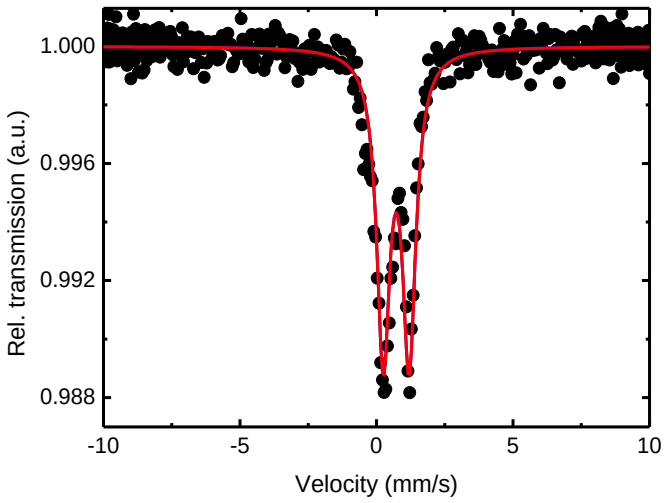

Figure 3.6. Room temperature zero-field Mössbauer spectrum of Fe(^{15c5}PDI)Cl_2 (**11**).

3.3 Reduction of ^{15c5}PDI Complexes

The dichloride species was dissolved in DCM and reduced under 20 psi CO in order to produce the dicarbonyl iron species (Eq. 3.2). Slow evaporation of diethyl ether yielded dark green crystals identified as Fe(^{15c5}PDI)(CO)$_2$ (**12**).

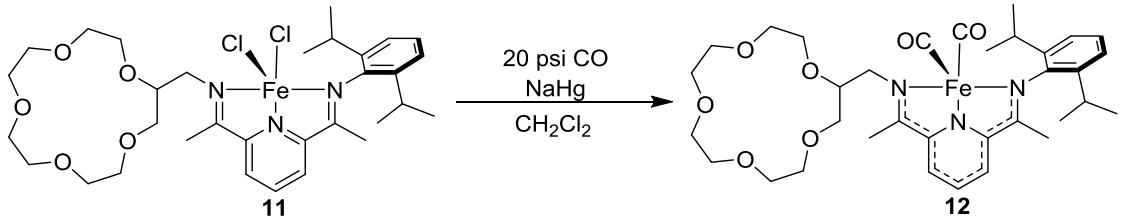

(3.2)

The solid-state FTIR illustrates the appearance of two stretches at 1946 cm^{-1} and 1882 cm^{-1}, corresponding to the CO stretches from complex **12** (Figure 3.7).

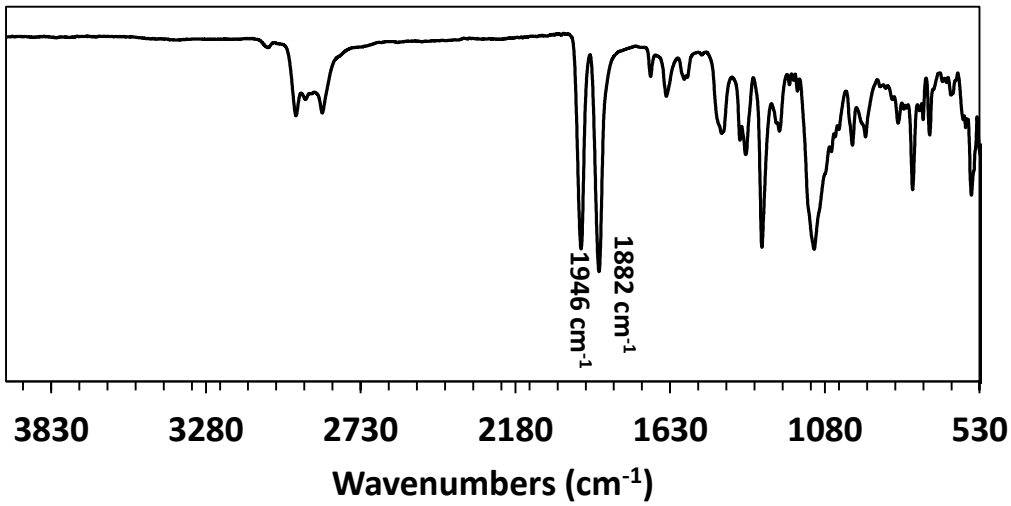

Figure 3.7. Solid-state FTIR spectrum of Fe(^{15c5}PDI)(CO)$_2$ (**12**).

The ^{1}H NMR spectrum (Figure 3.8) reveals the C-H resonances from the 15-c-5 pendant crown are found in the range from 3.5 ppm to 4.5 ppm. At 1 ppm, we observe the resonances from the protons corresponding to the isopropyl group of the 2,6-diisopropyl aryl group. The aromatic protons from that group give rise to resonances at 7.2 ppm, 7.5 ppm, and 8.15 ppm.

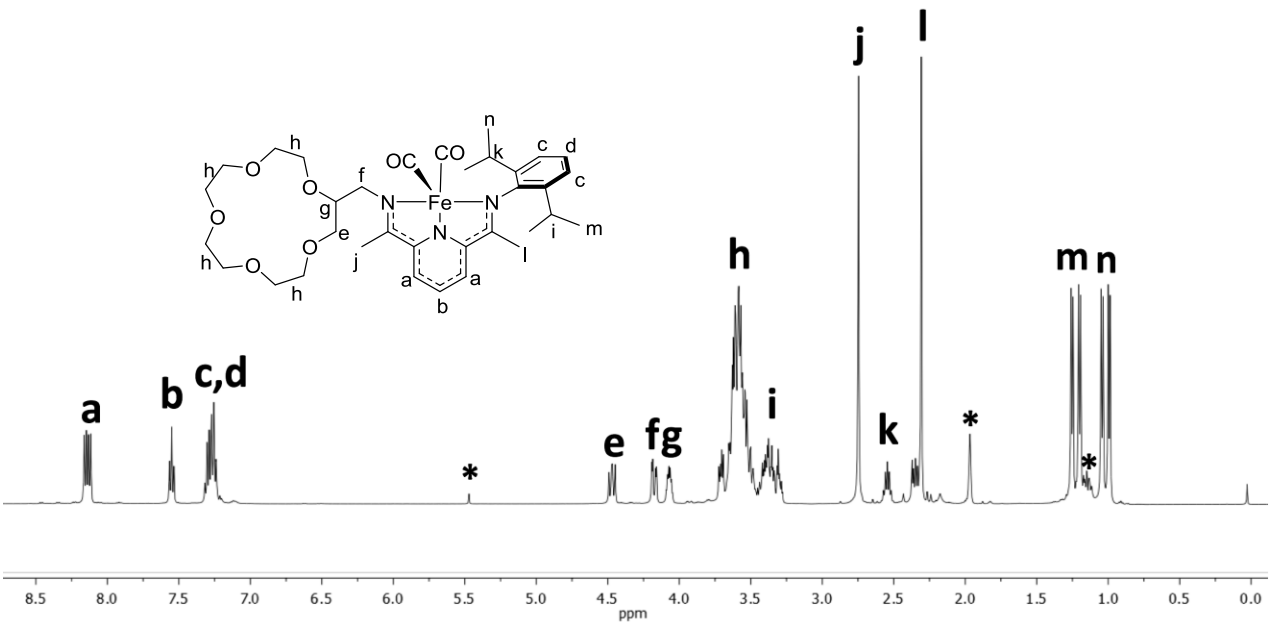

Figure 3.8. ^{1}H NMR of Fe(^{15c5}PDI)(CO)$_2$ (**12**), 500 MHz, CD_3CN (* represents solvent).

The solid-state structure of **12** (Figure 3.9, left) reveals a square pyramidal geometry ($\tau = 0.04$).[93] The C_{imine}-N_{imine} bonds measured as 1.333(5) and 1.323(5) Å. The C_{imine}-C_{ipso} bonds measured to be 1.431 (5) and 1.444 (5) Å. The Mössbauer parameters (ΔE_Q= 1.198 (7) and δ= -0.080 (2) mm/s) suggest a spin state of S = 0 with a Fe^{II} center and a doubly reduced ^{15c5}PDI ligand.[92] The Mössbauer spectrum is shown in Figure 3.9, right. Table 3.1 summarizes the Mössbauer parameters for **12**, **13**, and **14.**

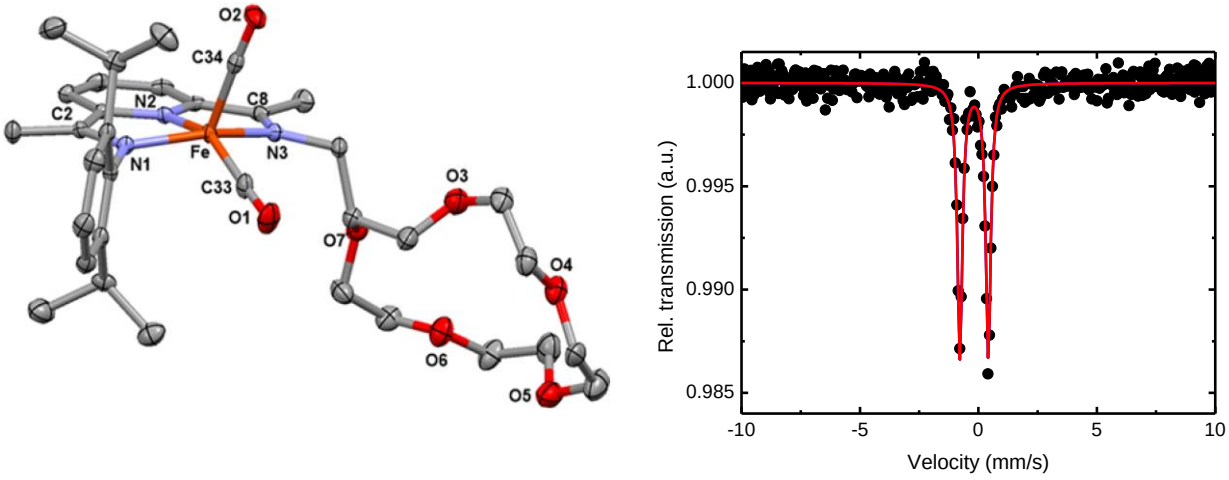

Figure 3.9. Solid-state structure (30% probability) of Fe(^{15c5}PDI)(CO)$_2$ (**12**) (left) and zero-field room temperature Mössbauer spectrum of Fe(^{15c5}PDI)(CO)$_2$ (**12**) (right). Selected bond lengths (Å) and angles

(deg): Fe1–C34 1.784(4), Fe1–C33 1.787(5), Fe1–N1 1.964(3), Fe1–N2 1.857(3), Fe1–N3 1.965(3), C2–N1 1.333(5), C8–N3 1.323(5); C34–Fe1–C33 95.56(19), N2–Fe1–C33 153.18(17), N1–Fe1–N3 155.54(13).

Table 3.1. Mössbauer parameters for and selected bond lengths for **12**, **13**, **14**.

	12	**13**	**14**
ΔE_Q (mm/s)	1.198 (7)	1.75(1)	1.418(9)
δ (mm/s)	–0.080(2)	–0.080(5)	–0.087(5)
C_{imine}-N_{imine} (Å)	1.333(5), 1.323(5)	1.312(7), 1.325(6)	1.326(6), 1.331(6)
C_{imine}-C_{ipso} (Å)	1.431(5), 1.444(5)	1.424(8), 1.428(7)	1.441(7), 1.434(7)

3.4 Encapsulation of Li^+

A slight excess of Lithium hexafluorophosphate ($LiPF_6$) was added to a dark green solution of ^{15c5}PDIFe(CO)$_2$ (**12**) in acetonitrile and allowed to stir for one day. The solvent was removed in *vacuo* and redissolved in CH_2Cl_2. The filtered CH_2Cl_2 solution was layered with pentane to produce dark green crystals were identified as [^{15c5}PDIFe(CO)$_2$Li][PF_6] (**13**) (Eq. 3.3).

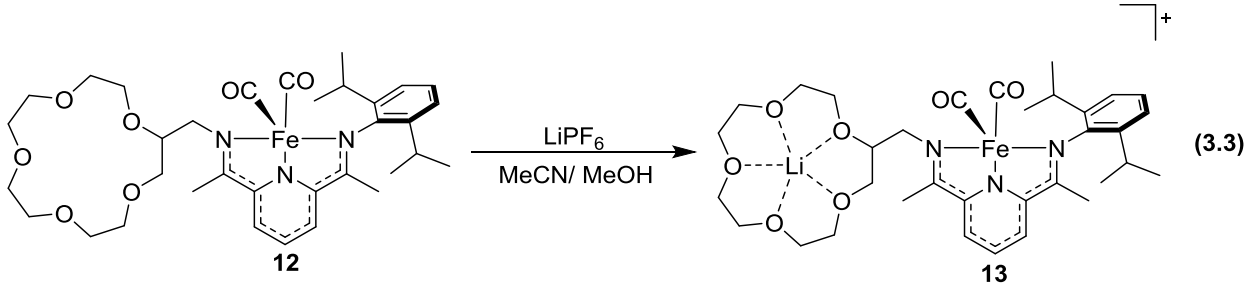

12 **13** **(3.3)**

The FTIR spectrum displayed the carbonyl stretches at 1931 and 1866 cm^{-1} (Figure 3.10). However, in solution a shift is observed in the carbonyl stretches to 1951 and 1886 cm^{-1}. The PF_6^- counterion shows up at 824 cm^{-1}.

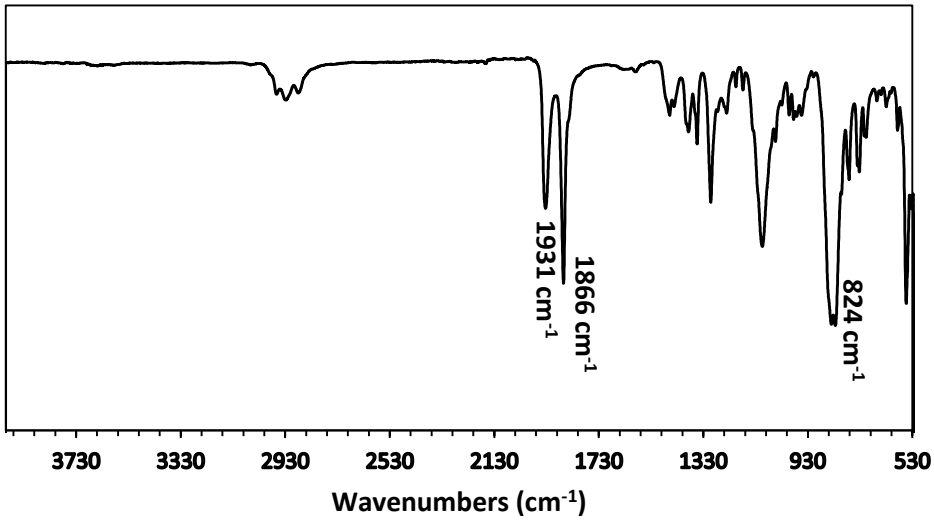

Figure 3.10. Solid FTIR spectrum of [^{15c5}PDIFe(CO)$_2$Li][PF_6] (**13**).

The ^{1}H NMR spectrum of **13** shows a fairly similar spectrum to that of **12** (Figure 3.11). However, upon encapsulation, a slight shift is observed in the crown protons from 3.04, 3.13, and 3.42 ppm in **12** to 3.25, 2.28, and 3.49 ppm in **13**. The expected triplet and doublet are overlapped into a multiplet integrating for the three protons. In complex **12** however, two very distinct resonances are observed for those protons.

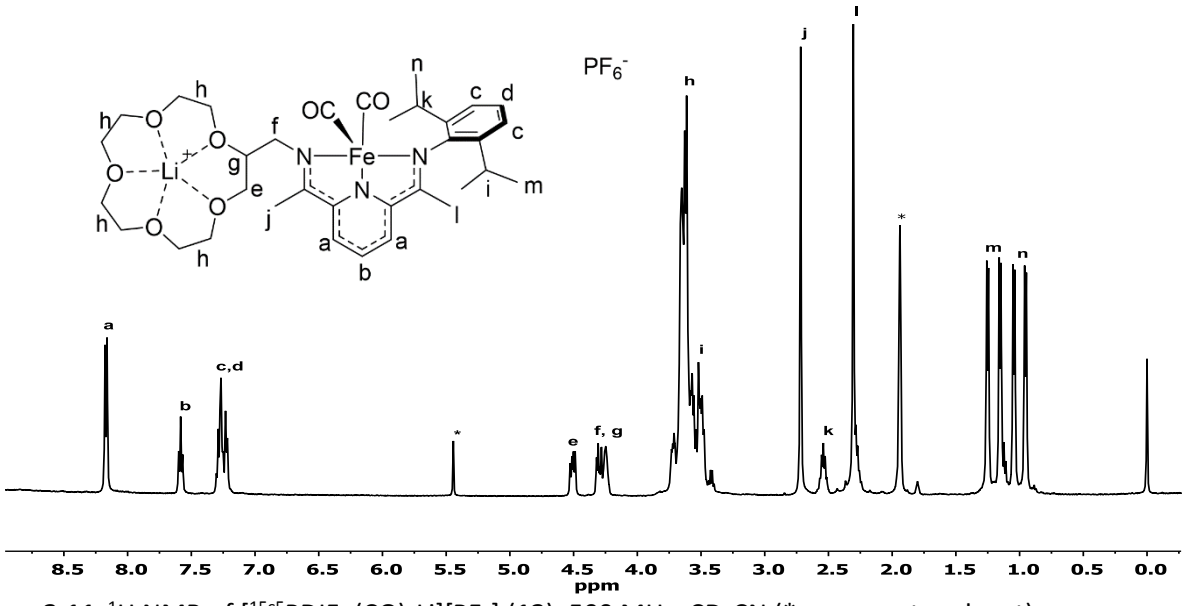

Figure 3.11. ^{1}H NMR of [^{15c5}PDIFe(CO)$_2$Li][PF_6] (**13**); 500 MHz, CD_3CN (* represents solvent).

The solid-state structure of **13** (Figure 3.12) established a five-coordinate Fe(II) center with square pyramidal geometry ($\tau = 0.36$). The C_{imine}-N_{imine} bond lengths measured yielded values of 1.326 (6) and 1.331 (6) Å. The C_{imine}-C_{ipso} bond lengths remain the same (1.441 (7) and 1.434 (7) Å), confirming no change in the oxidation state of the ligand upon addition of the alkali metal ion (Table 3.1). The structure illustrates a six coordinate Li^+, in which it interacts with the 5 oxygen atoms from the 15-c-5 crown and one of the fluorine atoms from the PF_6^- counterion (Figure 3.12). The Mössbauer parameters include E_Q of 1.75(1) mm/s and δ of -0.080(5) mm/s shows a doubly reduced PDI ligand, further confirming no change in the oxidation state.

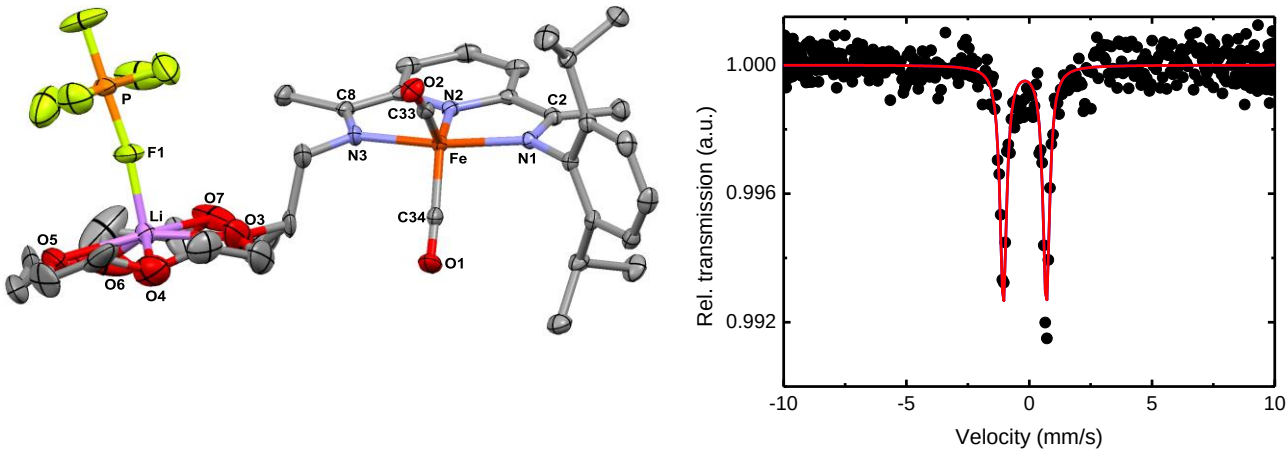

Figure 3.12. Solid-state structure (30% probability) of [^{15c5}PDIFe(CO)$_2$Li][PF_6] (**13**) (left); Zero-field room temperature Mössbauer spectrum of [^{15c5}PDIFe(CO)$_2$Li][PF_6] (**13**) (right). Selected bond lengths (Å) and angles (˚): Fe(1)-C(34) 1.777(6), Fe(1)- C(33) 1.777(6), Fe(1)-N(1) 1.975(4), Fe(1)-N(2) 1.842(4), Fe(1)-N(3) 1.967(4), C(2)-N(1) 1.325(6), C(8)-N(3) 1.312(7), Li(1)-F(1) 1.860(10), Li(1)-O(3) 2.147(11), Li(1)-O(3) 2.147(11), Li(1)-O(4) 2.318(12), Li(1)-O(5) 2.153(11), Li(1)-O(6) 2.104(12), Li(1)-O(7) 2.277(11), and C(34)Fe(1)C(33) 93.2(2), N(2)Fe(1)C(33) 128.9(2), N(1)Fe(1)N(3) 158.21(18).

The complex was investigated in solution to further explore the interaction between the Li^+ and the 15-c-5. Titrations of Li^+ in acetonitrile-d_3 to a solution of **12** acetonitrile-d_3 (Figure 3.13) were carefully examined through NMR spectroscopy. The C-H region of the 15-c-5 ring was monitored in order to observe its chemical shift upon encapsulation of the Li^+. An average chemical shift of 0.125 ppm was

observed in the crown ether resonances of ^{15c5}PDIFe(CO)$_2$ (**12**) upon encapsulation of the Li^+ metal ion. A plot of the chemical shift of the C-H group versus the equivalents of $LiPF_6$ added to the solution demonstrated that there was a 1:1 binding ratio of complex to $LiPF_6$. This observation is also reflected in the ^{1}H NMR spectrum. After the addition of one equivalent of $LiPF_6$, there is no resonance shift observed in the C-H region.

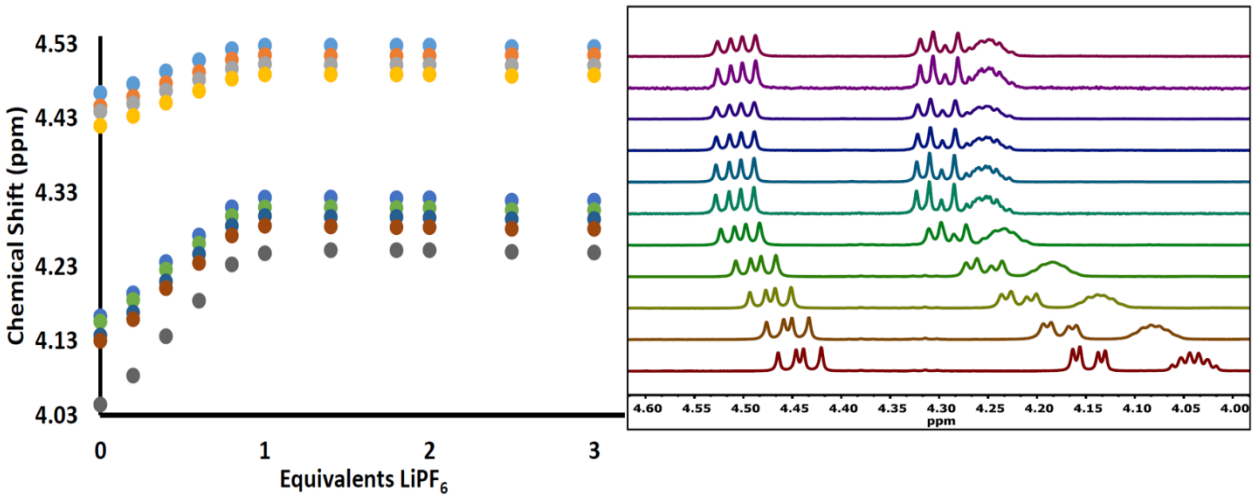

Figure 3.13. Plot of the chemical shift of the 15c5 C-H resonances in ^{15c5}PDIFe(CO)$_2$ (**12**) versus the equivalents of $LiPF_6$ added (left) and the stacked ^{1}H NMR spectra corresponding to the 15c5 C-H resonances upon titration with $LiPF_6$. (0 equivalents of $LiPF_6$ [bottom] and 3 equivalents of $LiPF_6$ added [top]).

3.5 Encapsulation of Na^+

The ^{15c5}PDIFe(CO)$_2$ (**12**) complex can also chelate the Na^+ metal ion. A slight excess of sodium hexafluorophosphate was added to a dark green solution of **12** in CH_3CN and allowed to stir for one day (Eq. 3.4). The solvent was removed in *vacuo* and redissolved in CH_2Cl_2. The filtered DCM solution was layered with pentane to produce dark green crystals were identified as [^{15c5}PDIFe(CO)$_2$Na][PF_6] (**14**).

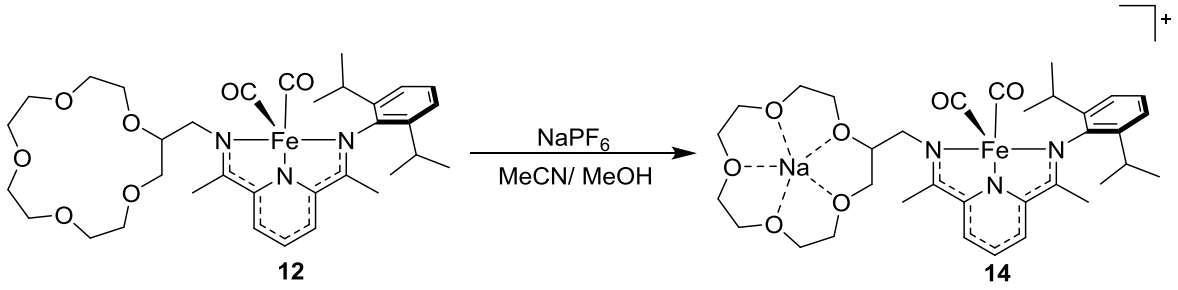

12 14 (3.4)

The solid-state FTIR spectrum reveals the carbonyl stretches at 1936 and 1868 cm^{-1} (Figure 3.14). The PF_6^- counterion is present at 835 cm^{-1}. In solution, a shift in the carbonyl stretches is also observed (1951 cm^{-1} and 1886 cm^{-1}).

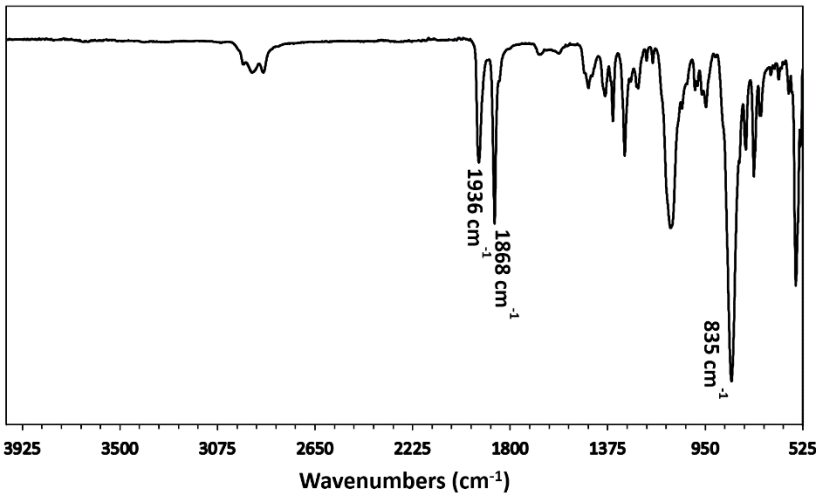

Figure 3.14. Solid-state FTIR spectrum of [^{15c5}PDIFe(CO)$_2$Na][PF_6] (**14**).

The solid-state structure (Figure 3.14, left) established a five-coordinate iron center with a square pyramidal geometry (τ = 0.01). In this case, the Na^+ is seven coordinate interacting with five oxygen atoms and two F atoms from the PF_6^- counterion. Upon encapsulation of the Na^+ metal ion, the C_{imine}-N_{imine} bond lengths yielded values of 1.333(5) and 1.323 (5) Å and C_{imine}-C_{ipso} bond lengths of 1.441 (7) and 1.434 (7) Å (Table 1). These bond lengths did not change much from the C_{imine}-N_{imine} (1.326 (6) and 1.331 (6) Å) and C_{imine}-C_{ipso} (1.431 (5) and 1.444 (5) Å) measured in ^{15c5}PDIFe (CO)$_2$ (**12**), suggesting that there is no change in oxidation state of the ligand. As determined by Mössbauer(ΔE_Q= 1.418(9) mm/s

and δ= -0.087(5) mm/s), the iron center remains Fe(II) and the ligand is confirmed to be a doubly reduced ^{15c5}PDI (Figure 3.14, right).

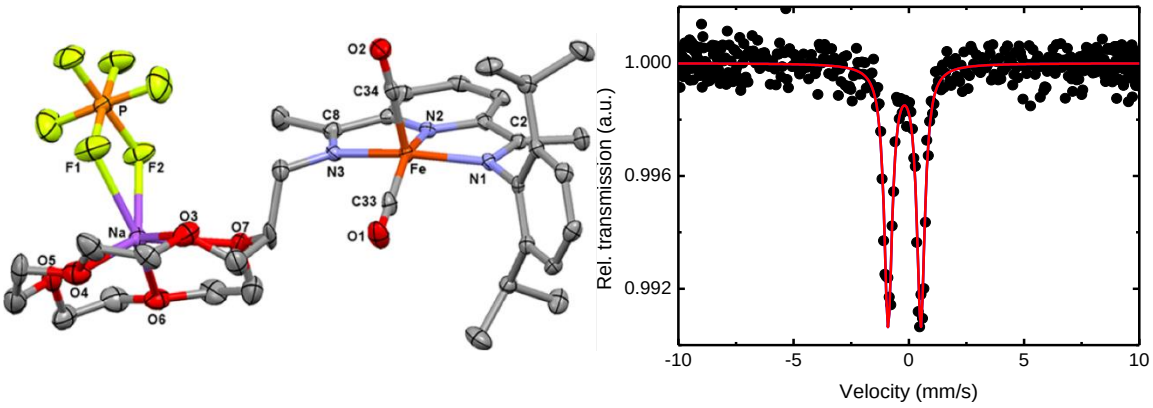

Figure 3.15. Solid-state structure (30% probability) of [Fe(^{15c5}PDI)(CO)$_2$Na][PF$_6$] (**14**) (left). Room-temperature Mössbauer of [Fe(^{15c5}PDI)(CO)$_2$Na][PF$_6$] (**14**). Selected bond lengths (Å) and angles (deg): Fe1–C34 1.795(6), Fe1–C33 1.792(6), Fe1–N1 1.980(4), Fe1–N2 1.863(4), Fe1–N3 1.972(4), C2–N1 1.331(6), C8–N3 1.326(6), Na1–F1 2.438(4), Na1–F2 2.401(4), Na1–O(avg) 2.414; C34–Fe1–C33 97.5(2), N2–Fe1–C33 155.7(2), N1–Fe1–N3 153.79(16).

Similar to the observations made between the ^{1}H NMR spectra of **12** and **13**, the ^{1}H NMR of **14** results in a downfield shift in the C-H resonances from the 15-c-5 upon the encapsulation of Na^+ (Figure 3.15). There is a slightly bigger shift observed upon encapulation of the Na^+ metal ion (0.134 ppm shift in **14** versus a 0.125 ppm in **13**).

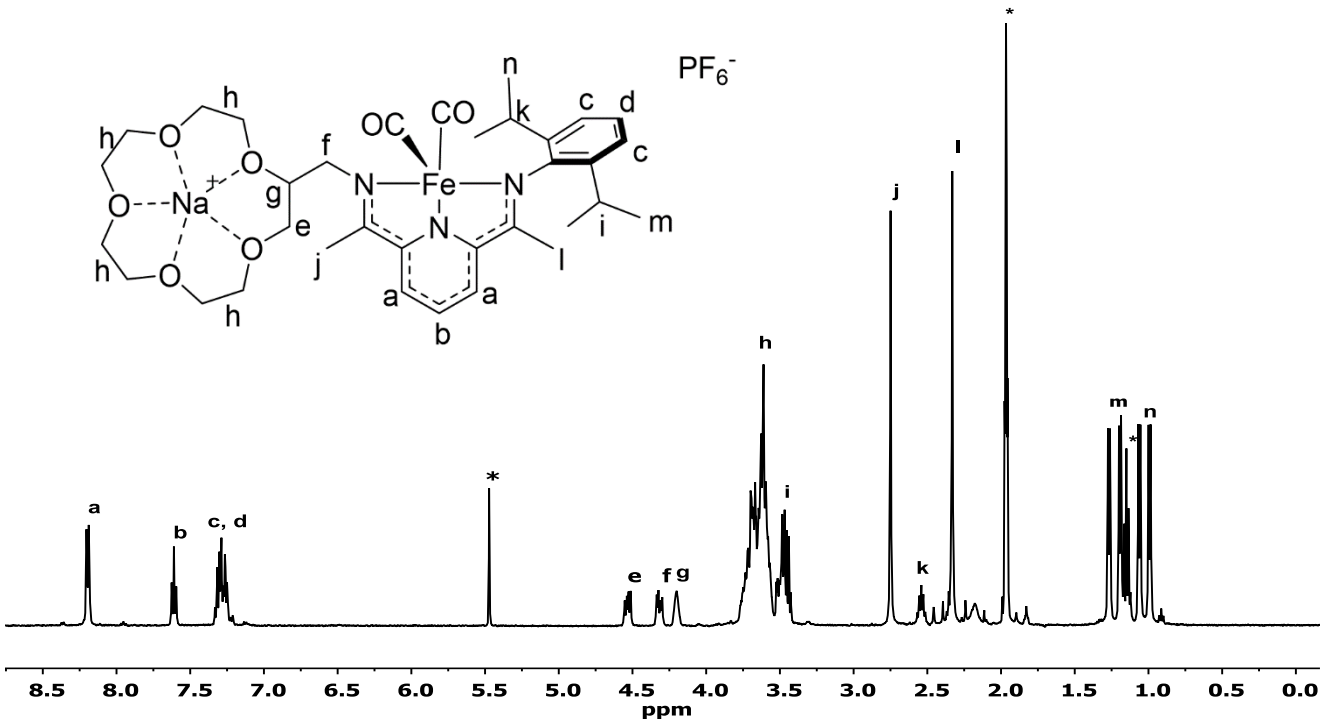

Figure 3.16. ^{1}H NMR of of [^{15c5}PDIFe(CO)$_2$Na][PF$_6$] (**14**); 500 MHz, CH_3CN (* represents solvent).

The C-H region of the 15-c-5 ring in complex **14** was investigated in solution through a series of titrations in order to determine the binding effect of the Na^+ metal ion (Figure 3.16). An average shift of 0.134 ppm is observed after the addition of one equivalent $NaPF_6$. No further shift in the C-H crown proton resonances were observed after one equivalent $NaPF_6$, suggesting that the Na^+ metal ion was encapsulated in the crown ether. The plot of the chemical shift of the 15-c-5 resonances versus the equivalents of $NaPF_6$ added to the complex demonstrates a 1:1 binding of the alkali metal ion, Na^+.

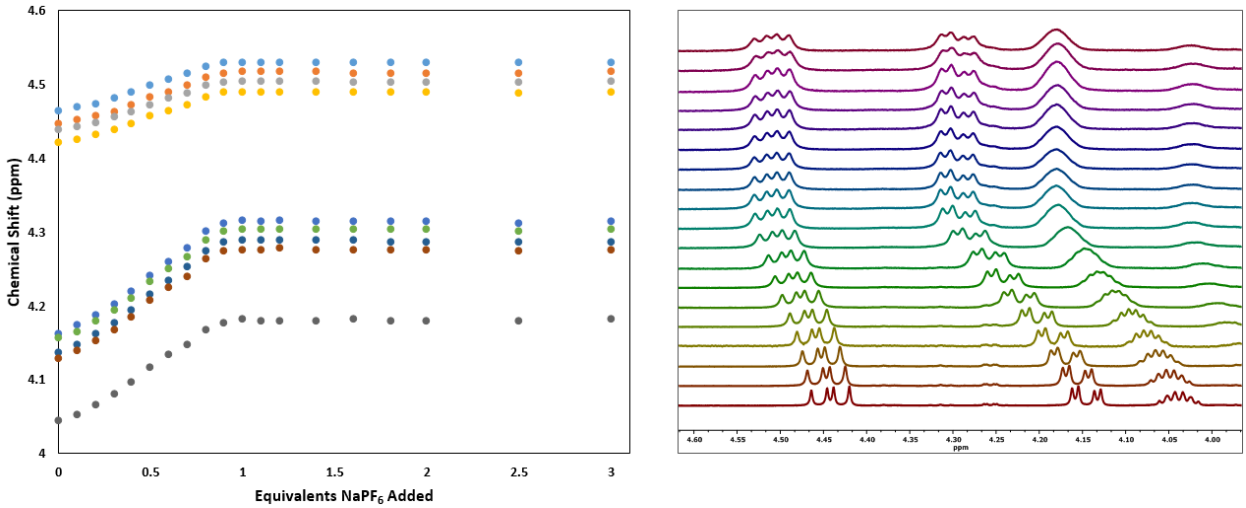

Figure 3.17. Plot of the chemical shift of the 15c5 C-H resonances in ^{15c5}PDIFe(CO)$_2$ (**12**) versus the equivalents of $NaPF_6$ added (left) and the stacked ^{1}H NMR spectra corresponding to the 15c5 C-H resonances upon titration with $NaPF_6$. (0 equivalents of $NaPF_6$ [bottom] and 3 equivalents of $NaPF_6$ added [top]).

3.6 Effect on Reduction Potentials

The secondary coordination sphere has been shown to tune the redox potential of the metal center.[94] In order to study the effect of the alkali ion on the reduction potentials, the electrochemistry of these reduced complexes was performed in three different solvents, THF, dichloromethane and acetonitrile. The results of the cyclic voltammetry in THF illustrated two quasi-reversible events observed corresponding to the one electron oxidation of the ligand and the one electron reduction from the metal (Figure 3.17).

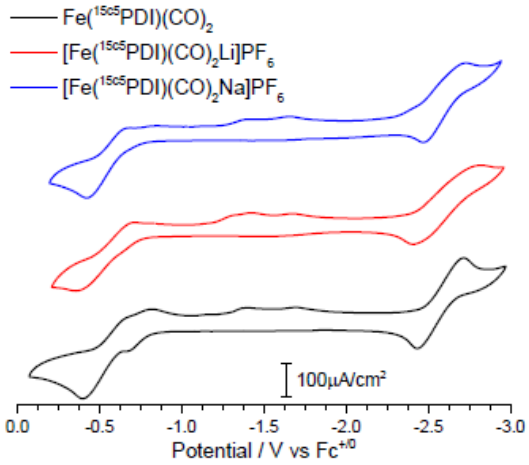

Figure 3.18. Cyclic voltammograms of ^{15c5}PDIFe(CO)$_2$ (**12**), [^{15c5}PDIFe(CO)$_2$Li][PF$_6$] (**13**), and [^{15c5}PDIFe(CO)$_2$Na][PF$_6$] (**14**) in THF; 0.1 M TBAPF$_6$, Ag/Ag$^+$ reference electrode, glassy carbon working electrode, Pt counter electrode

These quasi-reversible events have been previously observed in PDI ligand systems.[58, 95] However, when the electrochemistry is performed in acetonitrile, there are three redox events present (Figure 3.18). There are two irreversible events (-0.550 V and -1.20 V) and one reversible event (-2.303 V) observed in the cyclic voltammograms. One irreversible event is due to the one electron oxidation of the ligand to form [Fe(^{15c5}PDI)(CO)$_2$]$^+$ and the second irreversible event is likely a result of acetonitrile binding.

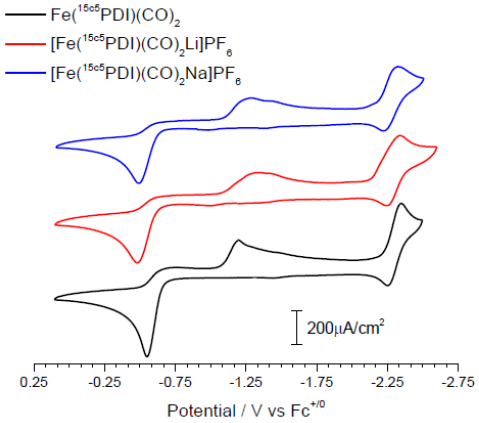

Figure 3.19. Cyclic voltammograms of ^{15c5}PDIFe(CO)$_2$ (**12**), [^{15c5}PDIFe(CO)$_2$Li][PF$_6$] (**13**), and [^{15c5}PDIFe(CO)$_2$Na][PF$_6$] (**14**) in Acetonitrile; 0.1 M TBAPF$_6$, Ag/Ag$^+$ reference electrode, glassy carbon working electrode, Pt counter electrode.

In DCM, however, the irreversible event present in the THF and MeCN samples is now reversible. This oxidative event in DCM has an $E_{1/2}$ value of -0.602 V. Compared to **12**, there is only about a 50 mV shift in the oxidation potential (E_{ox}) and the reduction potential (E_{red}) when Na^+ is added to the system. However, upon addition of Li^+ to the system, the 50 mV shift is only observed in the E_{ox}. The results of these experiments showed that we are able to have highly reduced complexes with a redox-inactive metal in the secondary coordination sphere which can then be used to perform other types of electron transfer reactions.

In order to confirm the reversibility of these redox events, the reductive event versus the square root of the scan rate was plotted in both DCM and MeCN (Figure 3.19). The linearity of these plots supports the reversibility of these redox events.

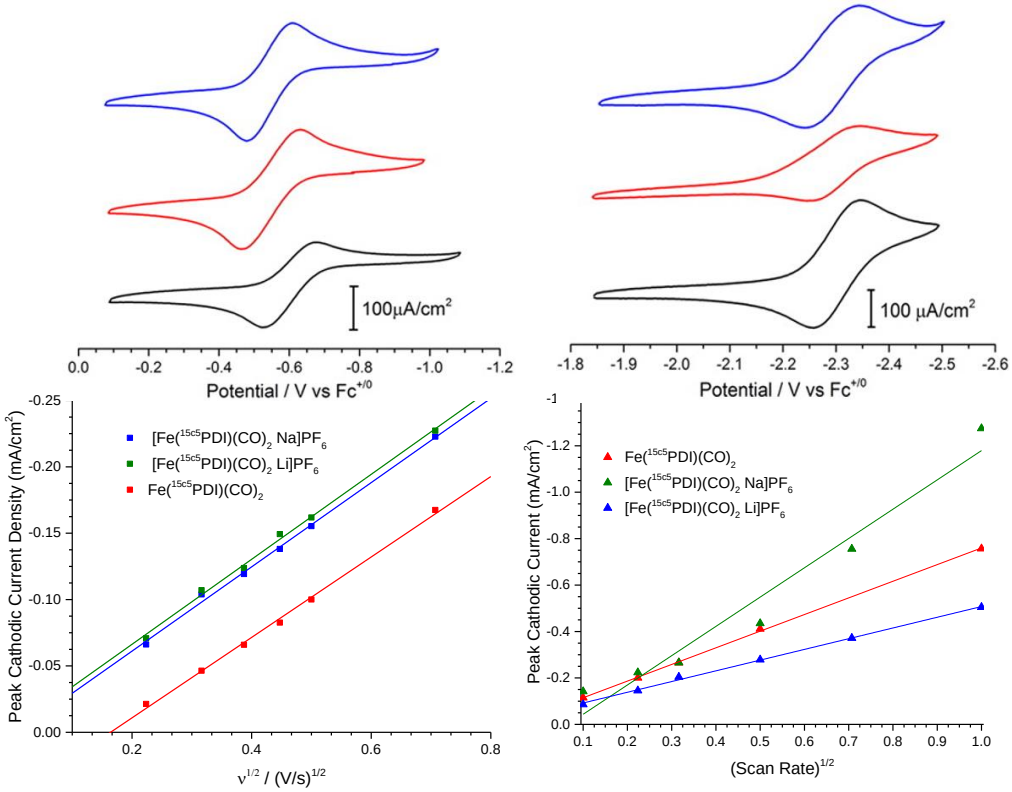

Figure 3.20. Cyclic voltammograms of 1mM Fe(^{15c5}PDI)$(CO)_2$ (**12**) (black), [Fe(^{15c5}PDI)$(CO)_2$ Li][PF_6] (**13**) (red), [Fe(^{15c5}PDI)$(CO)_2$ Na][PF_6] (**14**) (blue) in DCM (left) and in CH_3CN (right); 0.1 M $TBAPF_6$, Ag/Ag^+ reference electrode, glassy carbon working electrode, Pt counter electrode; and their corresponding plot of reductive event, $E_{cathodic}$ peak current versus square root of the scan rate for of Fe(^{15c5}PDI)$(CO)_2$ (**12**) (red squares), [Fe(^{15c5}PDI)$(CO)_2$ Li][PF_6] (**13**) (blue squares), [Fe(^{15c5}PDI)$(CO)_2$ Na][PF_6] (**14**) (green squares).

It was determined that these highly modular PDI ligand scaffolds are capable of encapsulating redox-inactive alkali metal ions (Li^+ and Na^+) both in solution and in solid state within the cavity of a pendant 15-crown-5. The electrochemical studies of the PDI system upon encapsulation of the Li^+ and Na^+ ions have shown to only have modest shifts in redox sites of the complex. Due to the unchanged redox sites, these systems can now be used to participate in electron transfer reactions, such as those observed in biological and synthetic systems.

Chapter 4. Dinitrosyl Iron Complex (DNIC)

4.1. Reduction of nitrate and nitrite to nitric oxide

Nitric oxide (NO) is versatile as a coordinating ligand due to its low ionization potential (9.5 eV) in comparison to other small molecules such as N_2 (14.5 eV) or CO (14.1 eV).[96] Nitric oxide's role as a signaling molecule aids in regulating blood pressure in the cardiovascular systems as well as regulating blood flow. Biologically, NO targets metal sites such as iron-sulfur cluster proteins, leading to the formation of dinitrosyl iron complexes (DNICs).[97,98] DNICs play a role in the transport of NO to molecules such as hemoglobin and cytochrome c which can absorb NO (Figure 4.1).

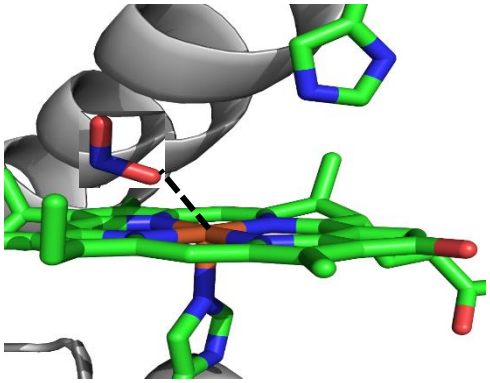

Figure 4.1. The heme site of the structure of the MbChl(NO_2) compound.[99] (Figure made in PyMOL).

Nitric oxide is considered a redox active ligand and is capable of binding in 3 distinct forms: $NO\cdot$, NO^+, or NO^-. The NO ligand is treated as NO^+ in a case where the M-N-O bond is about 180˚, whereas an angle less than 180˚ (bent) will yield to a treatment of NO^-. In order to describe the M-NO moiety in transition metal

nitrosyl complexes, the Enemark-Feltham notation, $\{M(NO)_x\}^n$, is used. In this notation, the n is the total number of metal d and NO π* electrons and x is the number of NO ligands bound to the metal (M) center.[100] The use of this notation allows for the electron count of this moiety to remain consistent, regardless of how the NO ligands are treated.

In order to explore the reduction of nitrate (NO_3^-) and nitrite (NO_2^-) to NO, we have developed complexes capable of mimicking the biological production of NO. Iron(II) PDI complexes with pendant bases in the secondary coordination sphere were synthesized. The redox-active PDI ligand scaffold, is capable of being protonated in the secondary coordination sphere and can therefore be used as the source of both protons and electrons for the transformation. Given that both the reduction of nitrate to NO ($NO_3^- + 4H^+ + 3e^- \rightarrow NO + 2H_2O$; $\Delta E = 0.96$ V) and nitrite to NO ($NO_2^- + 2H^+ + e^- \rightarrow NO + 2H_2O$; $\Delta E = 0.35$ V)[101] require protons and electrons for the transformation to occur, the PDI complexes make ideal candidates to probe these reductions.

4.2. DNIC Complexes

It was previously determined that the $[Fe(H^{DEA}PDI)(CO)_2][PF_6]$ (where ^{DEA}PDI=[(2,6-$^{i}PrC_6H_3$)(N=CMe)($N(Et)_2C_2H_4$)(N=CMe)C_5H_3N]) complex can be used to synthesize the DNIC, $[Fe(H^{DEA}PDI)(CO)_2][PF_6]$, by reduction of nitrite (Eq. 4.1).[102b]

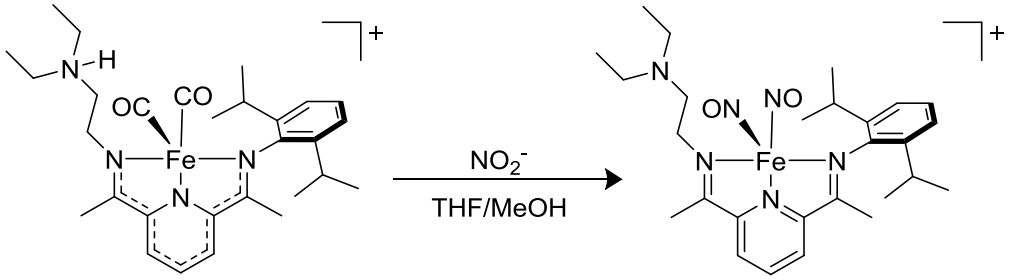

(4.1)

The doubly reduced complex with a protonated secondary coordination sphere, $[Fe(H^{DEA}PDI)(CO)_2][PF_6]$, is capable of the transfer of both protons and electrons. Taking advantage of the presence of both protons and electrons in the PDI system, nitrite reduction to NO was probed, leading to the synthesis of the DNIC.

Given the similarities of the ^{DEA}PDI ligand to the didpa ligand, we postulated that the DNIC complex could also be synthesized using the didpa ligand scaffold. For example, much like the didpa species, the ^{DEA}PDI ligand also undergoes a 105 mV shift upon protonation of the pendant amine.[102b] These two ligand platforms also share near identical architecture with the pendant base of the didpa ligand having a pKa of 18.4 and the diethylamine a pK_a of 18.1 upon being appended to the PDI scaffold. The CV properties of the ^{DEA}PDI ligand and the didpa scaffold are summarized in Table 4.1. For this reason, the didpa complex seemed viable to use for probing the reduction of NO_2^- to NO.

Table 4.1. Summarized CV events of ^{DEA}PDI (pK_a= 18.1) and Didpa (pK_a= 18.4).

	^{DEA}PDI Ligand	Didpa ligand
Unprotonated $E_{1/2}$ (V)	-0.579	-0.590
Protonated $E_{1/2}$ (V)	-0.474	-0.485
Δ $E_{1/2}$ (mV)	105	105

4.3 Synthesis of [Fe(H^{DEA}PDI)(CO)$_2$][PF$_6$]

In order to synthesize $[Fe(didpa)(NO)_2]^+$, a solution of $NaNO_2$ in MeOH was added to a green THF solution of $[Fe(Hdidpa)(CO)_2][PF_6]$ (**10**) (Eq. 4.2). The solution was stirred for overnight before being filtered through Celite. A color change from a dark green to a red-brown solution suggested that a reaction had occurred. Layering of the THF filtrate with pentane led to red-brown crystals identified as $[Fe(didpa)(NO)_2]^+$ (**15**). The remaining products of this reaction are still under investigation.

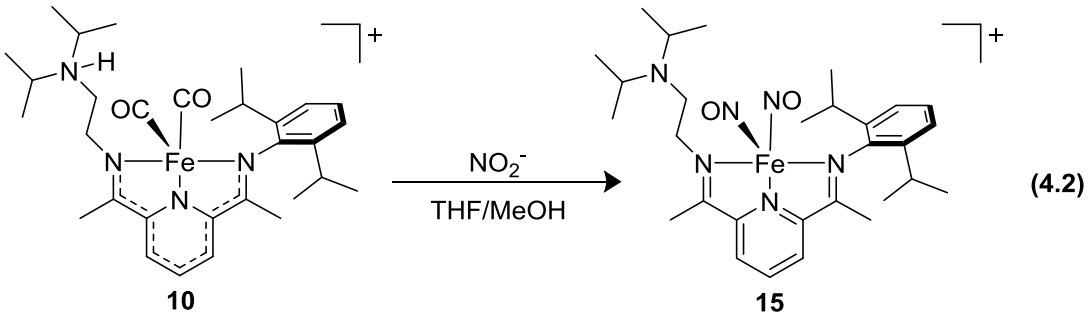

(4.2)

The solid-state FTIR spectrum of the DNIC **15** illustrates the absence of the 1940 cm^{-1} and 1883 cm^{-1} CO stretches from **10** and the appearance of the NO stretches at 1789 cm^{-1} and 1716 cm^{-1} (Figure 4.2). These

results confirm the complete reaction of the CO species, as the CO stretches are no longer present. The NO stretches are similar to those in the $[Fe(^{DEA}PDI)(NO)_2]^+$ complex found at 1786 cm^{-1} and 1716 cm^{-1}.[102,103] The NO stretching frequencies are also around the same values as observed in other synthesized DNICS[103,104] At 837 cm^{-1}, the PF_6^- counterion is observed.

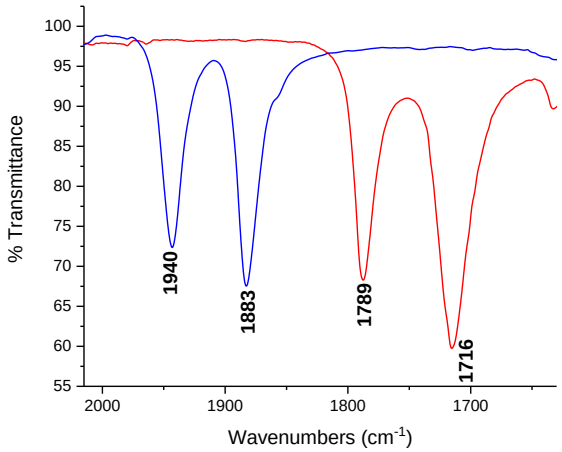

Figure 4.2. Solid-state FTIR spectra of $[Fe(Hdidpa)(CO)_2][PF_6]$ (**10**) (blue line) illustrating the CO stretches and of $[Fe(didpa)(NO)_2][PF_6]$ (**15**) (red line) illustrating the NO stretches.

The ^1H NMR spectrum of **15** illustrates significant changes from **10**. In comparison to the spectrum of **10**, we observe less well-defined resonances (Figure 4.3).

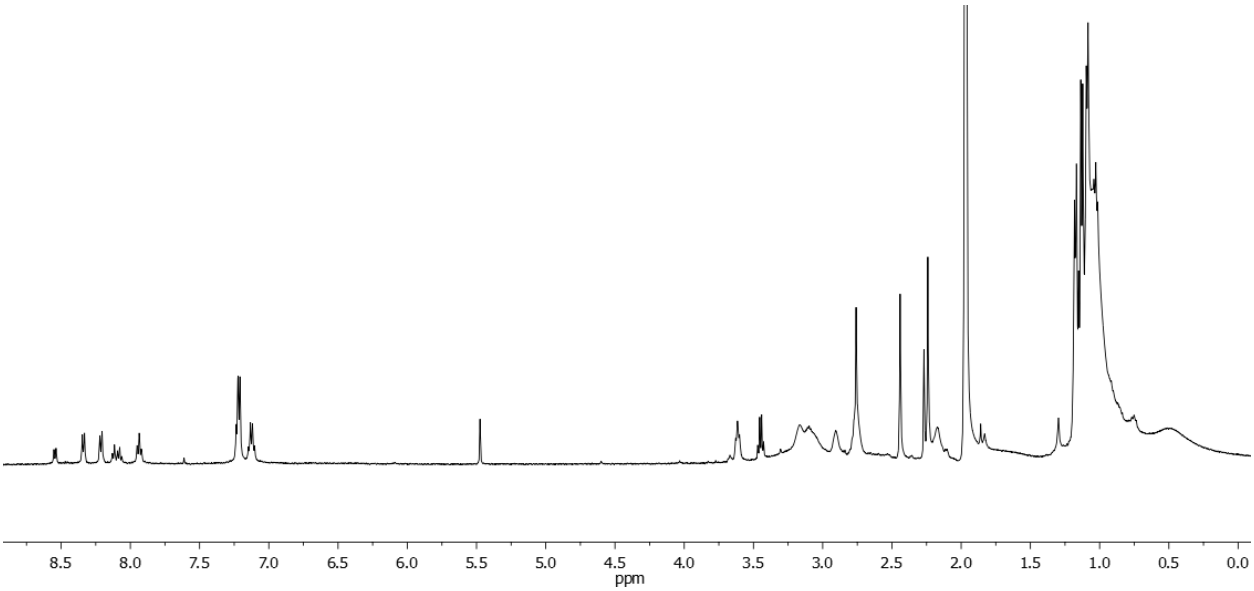

Figure 4.3. ^{1}H NMR spectrum of the $[Fe(didpa)(NO)_2][PF_6]$ (**15**); 500 MHz, CH_2Cl_2.

The solid-state structure of **15** is shown in Figure 4.4, confirming the synthesis of the DNIC. The geometry obtained from the crystal structure of **15** was found to be square pyramidal ($\tau = 0.26$). The C_{imine}-C_{ipso} bonds are measured to be 1.329 and 1.336 Å. The C_{imine}-N_{imine} bonds in **15** are contracted from 1.317 (2) and 1.329 (3) Å in $[Fe(Hdidpa)(CO)_2][PF_6]$ (**10**) to 1.271 Å and 1.282 Å in **15**. This decrease in bond lengths of the C_{imine}-N_{imine} bonds suggests that the system is no longer doubly reduced. The Mössbauer spectrum of **15** was obtained, yielding an isomer shift of 0.348(5) mm/s and an $E_Q = 0.791(7)$ mm/s (Figure 4.4). As was proposed from the contraction of the C_{imine}-N_{imine} bonds and the elongation of the C_{imine}-C_{ipso} bonds, the oxidation state confirms a neutral ligand. These conclusions can be further supported by analyzing the Mössbauer parameters of the $\{Fe(NO)_2\}^9$ DNICs from other groups.[103,104]

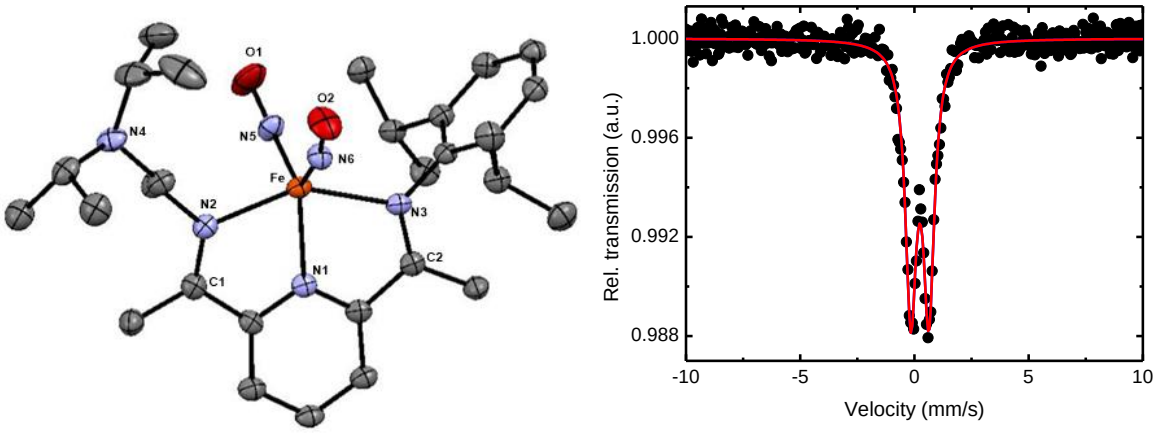

Figure 4.4. Solid-state structure (30% probability) (left) and the Mössbauer spectrum (right) of $[Fe(didpa)(NO)_2][PF_6]$ (**15**). The PF_6^- counterion is omitted for clarity. Selected bond lengths (Å) and angles (deg): Fe-N2 2.227, Fe-N3 2.145, Fe-N5 1.689, Fe-N6 1.688, N6-O2 1.163, N5-O1 1.154, C2-N3 1.271, C1-N2 1.282, Fe-N5-O1 162.5 (3), Fe-N6-O2 163.6 (2), N2-Fe-N3 148.28.

The calculated average Fe-NO bond angle obtained from the solid-state structure was 163.1° (bent). The average bond length for Fe-NO in **15** is 1.698 Å, which correlates well with those of other characterized DNIC systems (Table 4.2).[102,103,104] As was observed from the ^{DEA}PDI system, we can assign **15** an Enemark-Feltham notation of $\{Fe(NO)_2\}^9$ as well. As was previously calculated, the Fe is treated as a neutral (d^8) metal center with each bound NO ligand donating 1 electron, adding to 10 total electrons. However, we must recall that the overall charge of the complex is +1, yielding nine total electrons. Similar Enemark-Feltham notations have been reported by other groups who have synthesized these DNICs.

Table 4.2. Comparison of DNIC parameters.[102,103,104]

Complex	ν_{NO} (cm^{-1})	Fe-N(O) (Å)	N-O (Å)	δ(mm/s)	ΔE_Q (mm/s)
$[Fe(didpa)(NO)_2]^+$	1789, 1716	1.689	1.159	0.348 (5)	0.791 (7)
$[Fe(^{DEA}PDI)(NO)_2]^+$	1786, 1716	1.688	1.173	0.308 (7)	0.89(1)
$[Fe(^{iPr}PDI)(NO)_2]^+$	1794, 1721	1.704	1.169	-	-
$[Fe(dmp)(NO)_2]^+$	1746, 1840	1.674	1.174	0.37	1.77
$[Fe(NHC\text{-}iPr)_2(NO)_2]^+$	1723, 1791	1.696	1.177	0.11	0.27

(*dmp= 2, 9-dimethyl-1,10-phenanthroline; NHC= N-heterocyclic carbenes)

In order to verify that the bound NO ligands came from the nitrite source, as opposed to an external source, an isotopic study was performed. The isotopic form of sodium nitrite ($Na^{15}NO_2$) was obtained and the reaction with **10** was carried out following the synthesis from (Eq. 4.2). Analogous to the synthesis with $Na^{14}NO_2$, we observe the color change from green to red brown. Analysis of the solid-state ATR-FTIR spectrum illustrates the NO stretching frequencies of **15(^{15}NO)$_2$** alongside the NO stretches from the **15(^{14}NO)$_2$** synthesis. There is a distinct shift in the NO stretching frequencies from the ^{14}NO and the ^{15}NO. A shift from 1789 cm^{-1} and 1716 cm^{-1} in **15(^{14}NO)$_2$** to 1755 cm^{-1} and 1684 cm^{-1} in **15(^{15}NO)$_2$** can be seen as a result of the isotopic mass difference. These values correlate well to the expected shift values of 1757 cm^{-1} and 1685 cm^{-1} calculated based on the reduced mass.

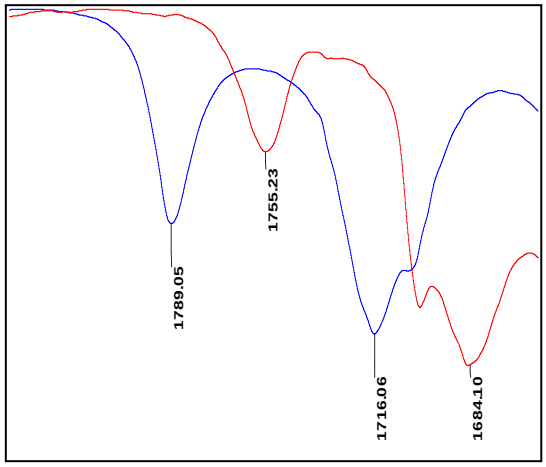

Figure 4.5. Solid-state FTIR spectra of **15(^{14}NO)$_2$** (blue line) and **15(^{15}NO)$_2$** (red line), illustrating the NO stretches.

4.4. Electrochemistry of [Fe(didpa)(NO)$_2$][PF$_6$]

In order to understand the redox properties of **15**, the electrochemistry of the complex was investigated by cyclic voltammetry. This was performed under N_2 atmosphere in CH_3CN using 0.1 M tetrabutylammonium hexafluorophosphate [(^{n}Bu)$_4$N][PF$_6$] as the supporting electrolyte, glassy carbon working electrode, platinum counter electrode, and a Ag/Ag^+ reference electrode. The CV of **15** reveals two reversible electrochemical reduction events at $E_{1/2}$= -0.910 V and $E_{1/2}$= -1.185 V (vs. Fc^+/Fc^0) (Figure

4.6). It can be proposed that the two observed reversible events are ligand-based reduction events, given that the open circuit potential (OCP) of complex **15** yielded a value of -0.360 V.

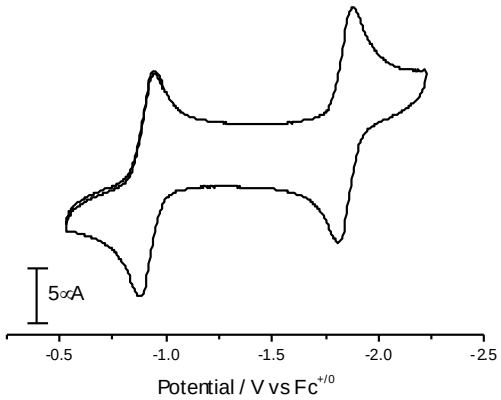

Figure 4.6. Cyclic voltammogram of 0.010 M $[Fe(didpa)(NO)_2][PF_6]$; 0.1 M $[(^nBu)_4N][PF_6]$ in CH_3CN, 200 mV/s scan (glassy carbon working electrode, platinum counter electrode, and a Ag/Ag^+ reference electrode).

In order to determine the reversibility of the redox events, reversibility studies were performed at each redox event. The results (Figure 4.7) confirm the reversible process in acetonitrile which can be seen in the plot of the $E_{cathodic}$ peak current versus square root of the scan rate for **15**.

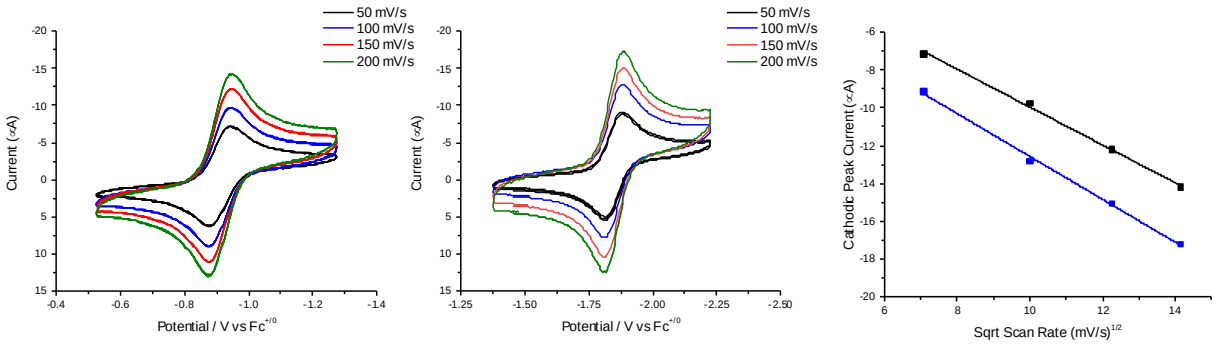

Figure 4.7. Cyclic voltammograms of 0.010 M $[Fe(didpa)(NO)_2][PF_6]$ at $E_{1/2}$= -0.910 V (left) and $E_{1/2}$= -1.185 V (middle); 0.1 M $[(^nBu)_4N][PF_6]$ in CH_3CN; 200 mV/s scan rate. Far right: Plot of $E_{cathodic}$ peak current versus square root of the scan rate for $[Fe(didpa)(NO)_2][PF_6]$ (**15**) at $E_{1/2}$= -0.910 V (black line) and $E_{1/2}$= -1.185 V (blue line), showing a linear correlation, to confirm the reversible process in CH_3CN.

4.5. Synthesis of $[Fe(didpa)(NO)_2][PF_6]$ via Nitrate Reduction

The synthesis of the DNIC was also obtained by the addition of one equivalent of tetrabutylammonium nitrate ($TBANO_3$) to a THF solution of **10** (Eq. 4.3) into a pressure vial. The solution was placed in an 80 °C oil bath for 12 hours before being filtered through a Celite plug. A color change from green to a dark red-brown solution was observed, suggesting a reaction had occurred.

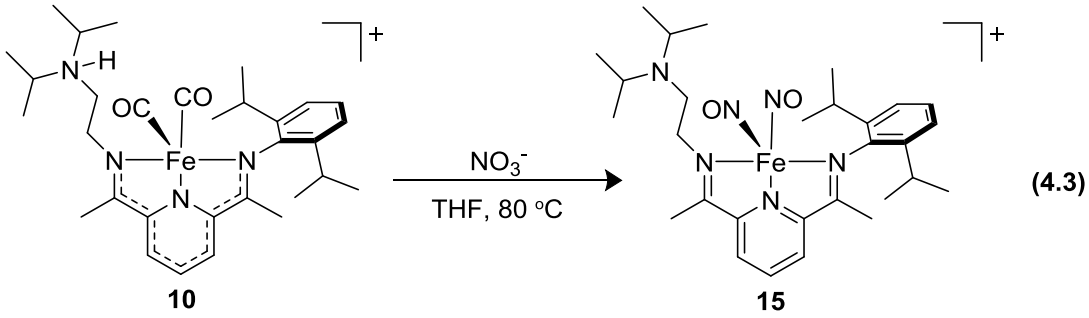

10 **15** **(4.3)**

Both a liquid and a solid IR spectrum was obtained in order to determine the products of the reaction (Figure 4.8, left). The results of the IR spectra confirmed the synthesis of the DNIC complex. Various solvent systems are still under investigation to try and obtain a crystal of the complex in order to investigate the solid state structure and confirm the synthesis of the DNIC complex. The liquid IR spectrum of the synthesized complex (Figure 4.8, right) also illustrates the absence of the carbonyls and the presence of the bound NO.

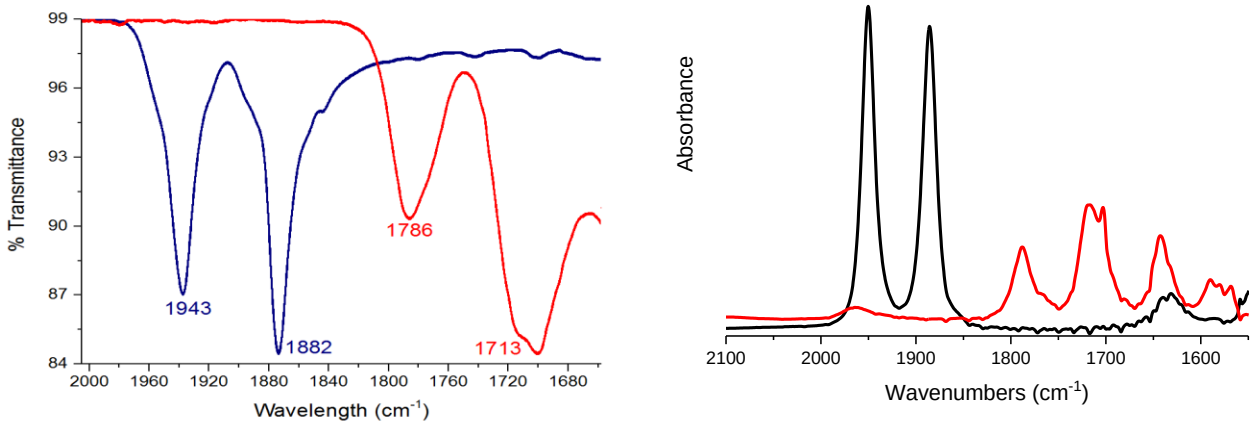

Figure 4.8. Solid-state FTIR (left) and liquid IR (right) spectra of $[Fe(Hdidpa)(CO)_2][PF_6]$ (blue/ black line) illustrating the CO stretches and the proposed DNIC (red line) after reaction with $TBANO_3$, illustrating the NO stretches.

4.6. FTIR Isotopic Labeling

Isotopic studies for the reduction of nitrate with $[Fe(Hdidpa)(CO)_2][PF_6]$ (**10**) were performed using $TBA^{15}NO_3$ as the NO_3^- source in an 80 °C oil bath. The resulting solution showed a color change from green to red-brown. Analysis of the FTIR spectrum shows a shift of the NO stretches from 1785 cm^{-1} and 1713 cm^{-1} to 1750 and 1700 cm^{-1} (Figure 4.9).

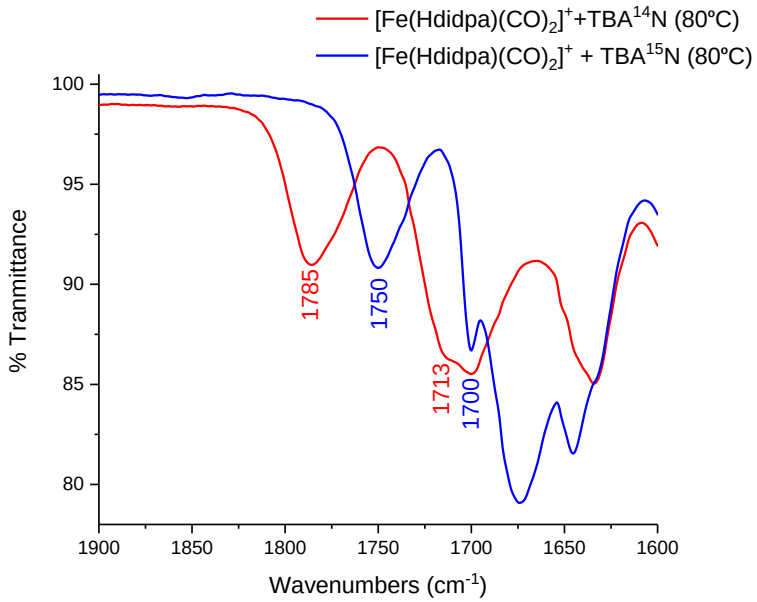

Figure 4.9. Solid-state FTIR spectra of $[Fe(didpa)(NO)_2][PF_6]$ (**15**) with $TBA^{14}NO_3$ reaction (red line) and **15** with $TBA^{14}NO_2$ (blue line), illustrating the NO stretches and the isotopic shift.

A comparison in the solid-state IR spectrum of the newly synthesized complex to **15** further supports the synthesis of the DNIC compound (Figure 4.10).

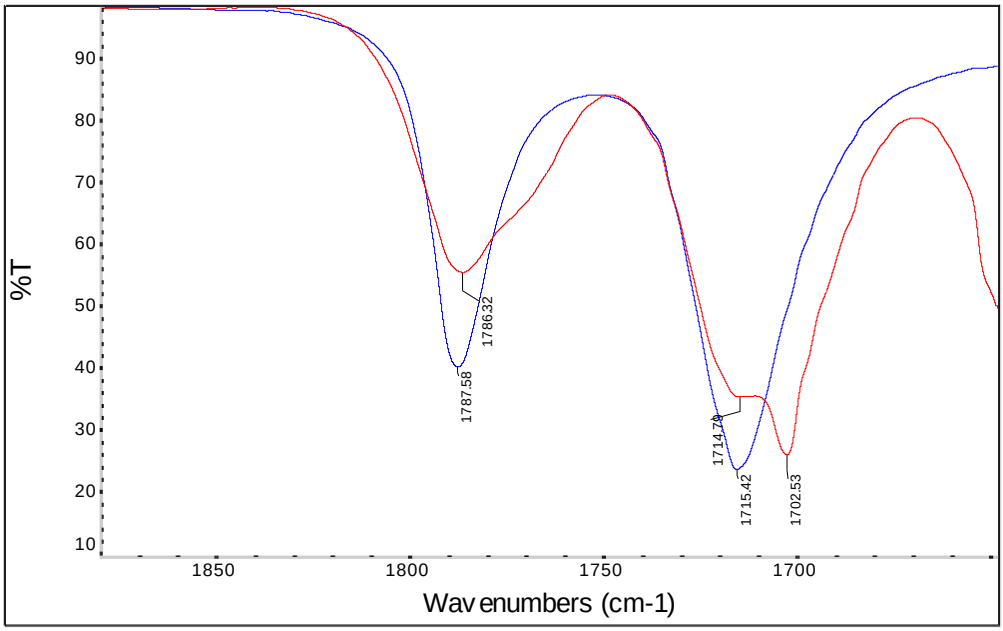

Figure 4.10. Solid-state FTIR spectra of $[Fe(didpa)(NO)_2][PF_6]$ (**15**) (blue line) and the proposed DNIC (red line) after reaction with $TBANO_3$, illustrating the NO stretches.

4.7. Effects of temperature on the synthesis of $[Fe(didpa)(NO)_2][PF_6]$

In order to demonstrate that heat is necessary for synthesis of the DNIC, the reaction from 4.3 was run at room temperature. The resulting products were analyzed via the solid-state and liquid IR spectra (Figure S26 and S27). However, upon inspection of the IR, the CO stretches from compound **10** are still present, suggesting that no reaction occurred between complex **10** and $TBANO_3$ and that reduction of NO_3^- requires heat for the reaction to proceed. A solid-state IR was obtained to determine if a reaction had occurred. However, the IR spectrum showed the presence of the CO's from the complex and no other changes were observed (Figure 4.11).

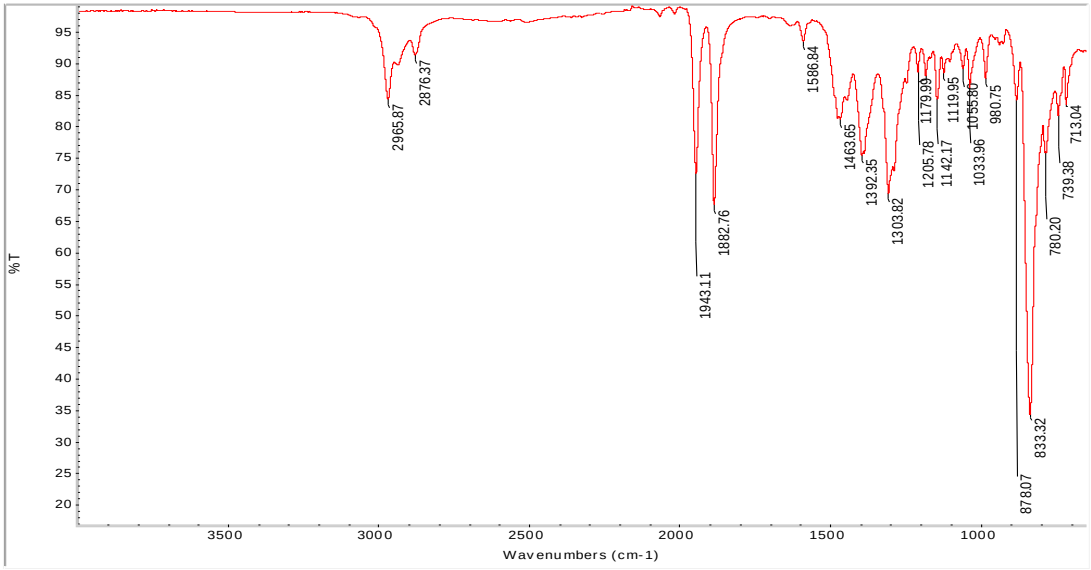

Figure 4.11. Solid-state FTIR spectrum of $[Fe(HdidpaI)(CO)_2][PF_6]$ (**10**) with the addition of $TBANO_3$ in THF after one day of stirring at room temperature.

Considering the possible decomposition of the reactants upon heating to 80 °C, it was important to explore the stability of $TBANO_3$ in 80 °C temperature. $TBANO_3$ was dissolved in THF and transferred to a 20 mL pressure vial and heated overnight at 80 °C. The solvent was removed and a solid-state IR was obtained. Comparing the heated solution to the solid-state IR of the $TBANO_3$ salt at room temperature demonstrated no change in the stretching frequencies (Figure 4.12).

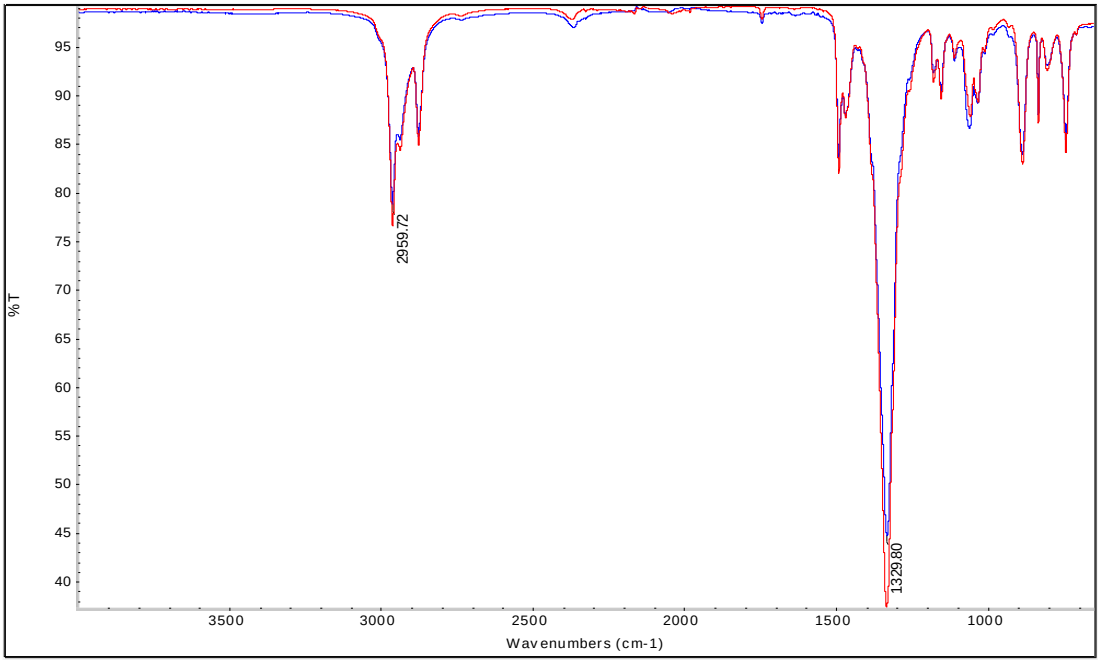

Figure 4.12. Solid-state FTIR spectra of $TBANO_3$ at room temperature (red line) and after being exposed to 80 °C heat for one day (blue line).

4.8. Investigating the role of the secondary coordination sphere in nitrate reduction

In order to probe the role of the secondary coordination sphere of the didpa ligand scaffold, the direduced, unprotonated complex Fe(didpa)$(CO)_2$ (**9**), was explored. The reaction of $TBANO_3$ and Fe(didpa)$(CO)_2$ (**9**) was set up (Eq. 4.4).

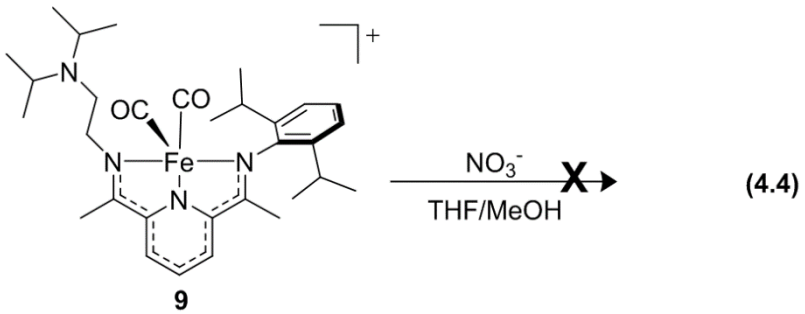

9 **(4.4)**

The solid- state FTIR was obtained and the presence of the CO stretches from complex **9** demonstrated that no reaction had occurred when using **9**, which lacks an H-bond in the secondary coordination.

To further support this observation, the previously synthesized Fe(^{MeO}PDI)$(CO)_2$ complex was utilized as it lacks the intramolecular H-bonding ability that is observed with the dipda system.[57, 94] Addition of $TBANO_3$

to a THF solution of Fe(^{MeO}PDI)(CO)$_2$ resulted in a dark green solution. The solution was placed in an 80 °C oil bath for one day (Equation 4.5). Upon initial inspection of the reaction, there was no color change observed as we saw in the reaction from 4.3.

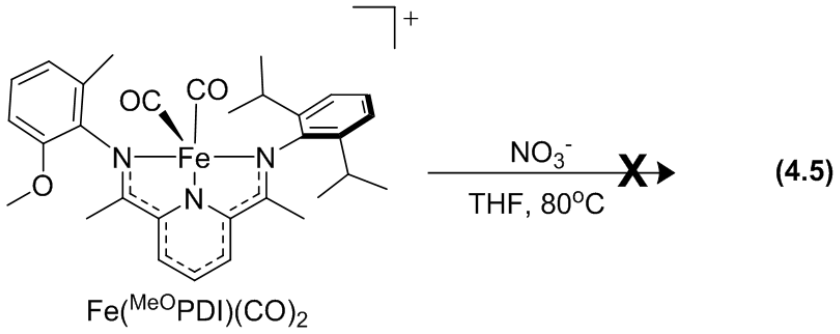

(4.5)

The liquid IR spectrum was obtained and compared to that of **15** in order to resolve whether the dinitrosyl complex was synthesized. The results suggested that the DNIC was in fact not formed. Upon the introduction of an external proton source, protonated Hünig's base [HDIPEA][PF_6^-], a color change occurred. However, it was concluded that the dinitrosyl complex was not synthesized based on the differences in the IR spectra.

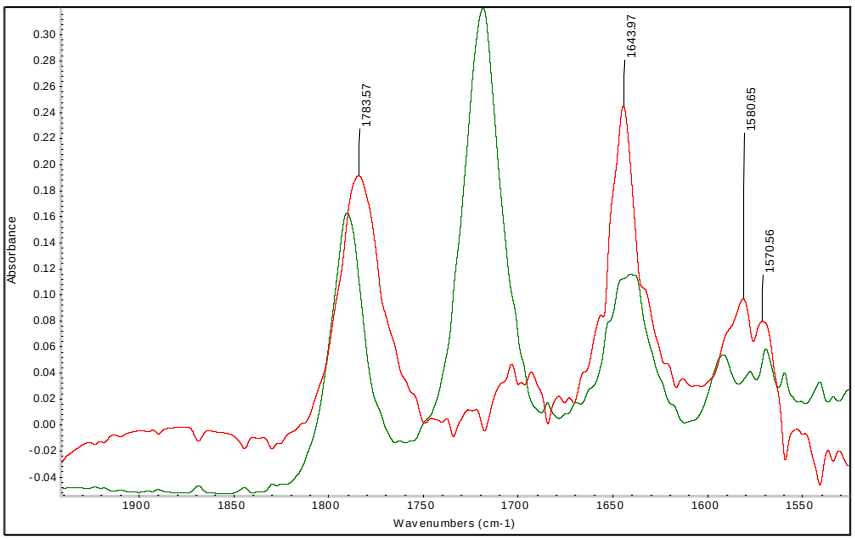

Figure 4.13. Liquid IR of Fe(^{MeO}PDI)(CO)$_2$ after addition of TBANO$_3$ and [HDIPEA][PF_6^-] in THF at 80 °C (red line) and the DNIC complex, [Fe(didpa)(NO)$_2$][PF_6] (**15**) (green line).

4.9. Investigation of the products in the synthesis of $[Fe(didpa)(NO)_2][PF_6]$

The yield of the DNIC complexes were calculated utilizing liquid IR. The small scale of the reactions allowed for a yield calculation using a calibration curve obtained from the NO stretches from the DNIC complexes. In a typical experiment, a series of solutions of known concentration of the DNIC were made up using THF as the solvent. The liquid IR spectrum was obtained for each individual solution using CaF_2 cell plates in the IR cell. The absorbance corresponding to the NO peak allowed for the fitting of two separate calibration curves (Figure 4.14).

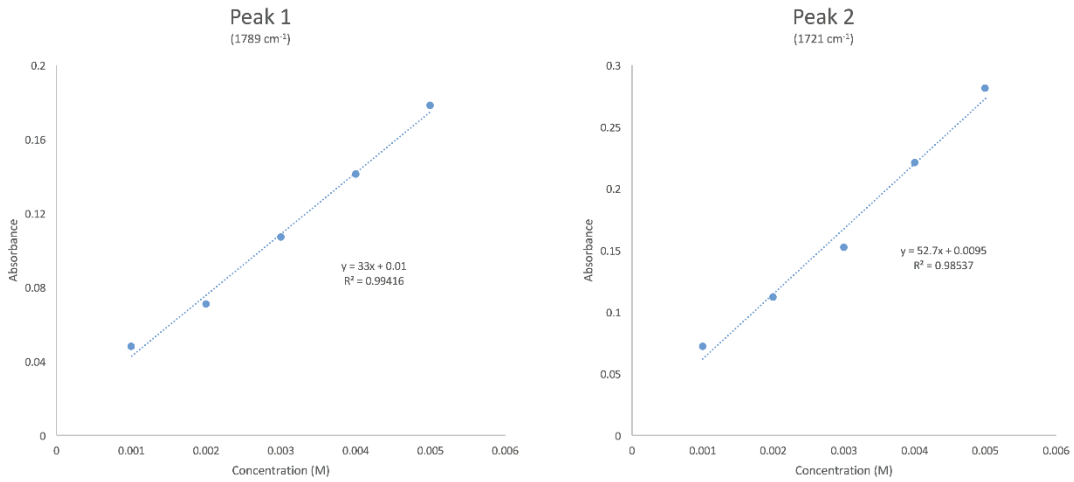

Figure 4.14. Calibration curve of the NO peaks (1789 cm^{-1} and 1721 cm^{-1}) for the % yield calculation of $[Fe(didpa)(NO)_2][PF_6]$ (**15**).

A new liquid IR was obtained of a known concentration of the DNIC in THF, and using the calibration curves, the moles of **15** were obtained. The reduction of NO_2^- to NO using the didpa scaffold produced a 39% yield of the DNIC. In comparison, the ^{DEA}PDI complex demonstrated a 52% yield. The reduction of NO_3^- to NO by use of the didpa complex gave a yield of 20%. The yields are summarized in Table 4.3. The remaining products of the nitrite and nitrate reactions are still under investigation.

Table 4.3. DNIC yields.

Complex	% Yield
$[Fe(^{DEA}PDI)(NO)_2]^+$	52%
$[Fe(didpa)(NO)_2]^+$ via $NaNO_2$	39%
$[Fe(didpa)(NO)_2]^+$ via $TBANO_3$ (80 °C)	20%

In an effort to investigate the remaining products for the $TBANO_3$ (Equation 4.3), the headspace analysis was analyzed for NO gas that may have been produced during the reaction. This was performed in a gas cell and studied via gas IR. The results did not exhibit NO peaks in the IR spectrum (Figure 4.15) and it established that NO gas is not a product of this reaction.

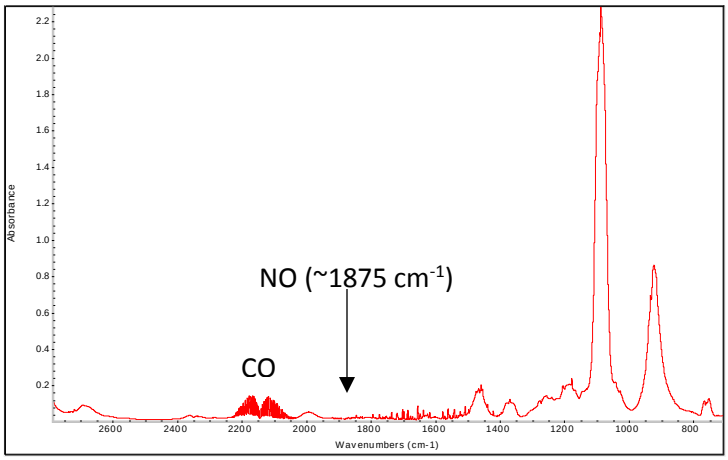

Figure 4.15. Gas IR spectrum of the headspace in reaction of **10** with $TBANO_3$ at 80 °C.

Since NO gas was not found in the headspace of the reaction, it was proposed that any excess nitrogen would be found as nitrate or nitrite in the remaining products. However, the solid-state FTIR spectrum gave inconclusive results, directing us to turn to ion chromatography.

An aqueous extraction of the DNIC solution in THF was done using a 1 M Na_2SO_4 solution. The aqueous solution was analyzed for possible NO_2^- or NO_3^- ions. The results of this experiment (Figure 4.16) illustrated a peak at a retention time of 4.2 minutes, corresponding to NO_3^-. However, there was no peak observed in the NO_2^- region of the spectrum. We can then assume there is an excess in NO_3^- from the $TBANO_3$ which did not react completely. The transformation of NO_3^- to NO requires the use of four protons and three

electrons (NO_3^- + $2H^+$+ $2e^-$→ NO_2^- + $2H_2O$ and NO_2^- + $2H^+$+ e^-→ NO + $2H_2O$). Therefore, it is expected that there is NO_3^- that will remain unreacted to NO due to the lack of electrons available in the PDI system. Upon protonation of the doubly reduced species, the solid-state structure and electrochemistry shows an availability of two electrons per PDI unit present for the reduction of nitrate. This limits the amount of NO_3^- that will fully reduce to NO, given that the full transformation is in need of three electrons. The spectrum obtained from the ion chromatography studies clearly shows the NO_3^- peak which can account for the unused NO_3^- based on the stoichiometry of Equation 4.3. Using the information obtained from the ion chromatograph, the amount of NO_3^- that is left unreacted can be calculated to be 34%.

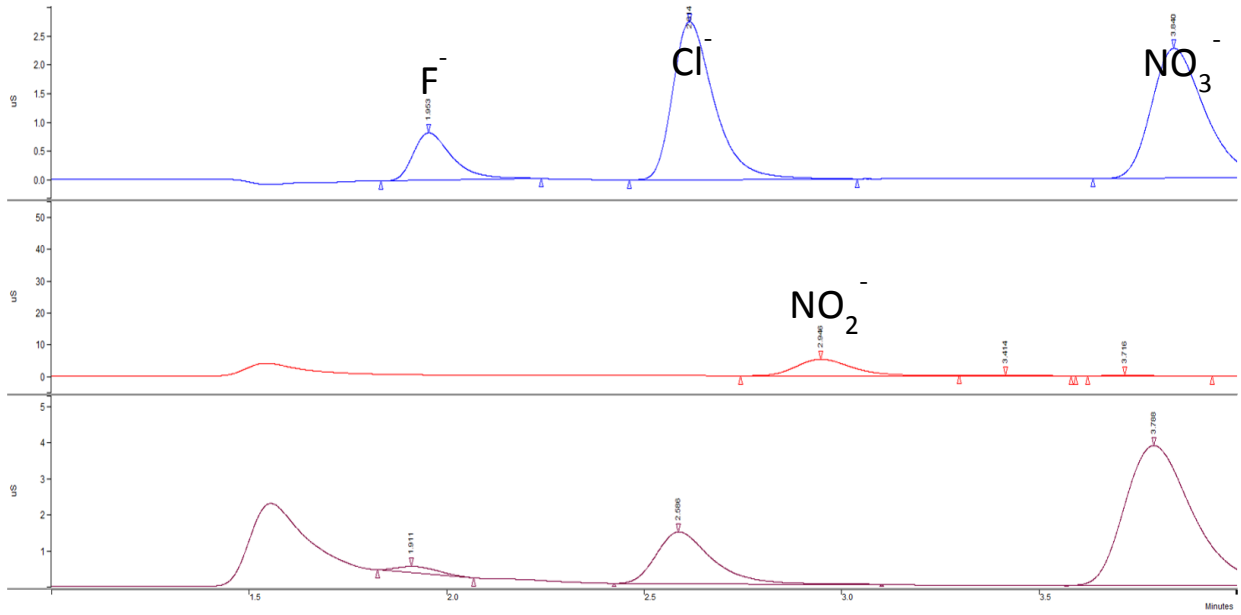

Figure 4.16. Ion chromatograph of the aqueous extraction of the reaction of [Fe(Hdidpa)$(CO)_2$][PF_6] (**15**) after addition of $TBANO_3$ at 80 °C, illustrating the presence of NO_3^- at 3.789 minutes (purple line) vs the standard containing F^- at 1.9 min, Cl^- at 2.6 min, and 15 ppm NO_3^- at 3.8 min (blue line). A standard of tetrabutylammonium nitrite illustrating the presence of NO_2^- at 2.9 min (red line).

Conclusion

Nature uses metalloenzymes for the activation of small molecules into more useful compounds. The motifs around the metal active site of metalloenzymes play a vital role for its function. Many of these reactions require protons and electrons for the transformation to occur. This thesis focuses on examining the secondary coordination sphere and merging that with the redox activity of metal complexes. The redox-active didpa ligand scaffold was used to synthesize Zn(didpa)Cl_2, [Zn(Hdidpa)Cl_2][PF_6], Fe(didpa)Cl_2, [Fe(Hdidpa)Cl_2][PF_6], Fe(didpa)$(CO)_2$, [Fe(Hdidpa)$(CO)_2$][PF_6], [Zn(didpa)Cl_2SH]$^-$ and [Fe(didpa)$(NO)_2$][PF_6] . The pendant amine in the didpa ligand allows for protonation in the secondary coordination, forming intramolecular hydrogen bonds that can aid in stabilizing substrates.

A series of Zn(II) complexes were synthesized and characterized by means of X-ray crystallography, ^{1}H NMR and FTIR. The protonated pendant amine of the didpa ligand in the zinc complexes allowed us to study the secondary coordination sphere of our system. The pKa of the $ZnCl_2$ complex was determined to be 18.1 and demonstrated that the pKa of the pendant amine does not get attenuated when the ligand is bound to the metal center of the complex. When protonated, [Zn(Hdidpa)Cl_2][PF_6] is able to form MHHBs. The strength of the MHHBs were determined by examining the results upon introduction of various H-bond accepting solvents and through gas phase calculations. The MHHB strength was computed to be 6 kcal/mol in Zn(didpa)Cl_2 and 5 kcal/mol in Zn(didpa)Br_2. The didpa ligand not only functions as an H-bond donor, but can also function as an H-bond acceptor. Considering this aspect of the ligand scaffold, the six-coordinate zinc hydrosulfido complex was synthesized. Analysis of UV-Vis spectra for the six-coordinate zinc complexes was used to confirm the synthesis [Zn(didpa)Cl_2SH]$^-$ upon addition of NBu_4SH, stabilized through the H-bond acceptance of the unprotonated didpa ligand.

In order to examine the redox activity of the didpa complexes, Fe(didpa)Cl_2, [Fe(Hdidpa)Cl_2][PF_6], Fe(didpa)$(CO)_2$, and [Fe(Hdidpa)$(CO)_2$][PF_6] were synthesized. The Fe(didpa)Cl_2 was reduced under CO and protonated in the secondary coordination sphere, leading to the doubly reduced, protonated species, Fe(didpa)$(CO)_2$. Electrochemistry was employed to measure the redox potential of the neutral iron PDI complex as well as the direduced species. The cyclic voltammograms showed a 105 mV shift upon protonation of the secondary coordination sphere.

Fe(PDI) complexes with a 15-c-5 crown ether were capable of chelating alkali metal ions in the pocket of the crown. The encapsulation of Li^+ and Na^+ to the ^{15c5}PDI complex were analyzed in the solid-state and in solution through X-ray crystallography and ^{1}H NMR. The electrochemistry of these compounds was also examined in DCM, MeCN, and THF. There was only a small shift in the redox event of the compound upon addition of either Na^+ or Li^+ into the system. There is a shift of 50 mV observed in the E_{ox} of the system upon encapsulation of Li^+, only when the cyclic voltammetry is run in DCM. On the other hand, encapsulation of Na^+ causes a shift of 50 mV in the E_{ox} when the CV is run in DCM, but there is also a 50 mV in the Er_{ed} when the CV is run in THF. This provides us with highly reduced complexes with pendant redox-inactive Lewis acids in the secondary coordination sphere.

The versatility of the didpa ligand allowed us to explore nitrite and nitrate reduction. Both of these chemical transformations require the use of both protons and electrons to achieve reduction to NO. Addition of sodium nitrite to [Fe(Hdidpa)$(CO)_2$][PF_6] resulted in the synthesis of a five-coordinate dinitrosyl iron complex (DNIC). Through IR spectroscopy, it was also determined that the DNIC complex can be synthesized by reaction of [Fe(Hdidpa)$(CO)_2$][PF_6] with $TBANO_3$ in THF at 80 °C. A series of control experiments showed that the protonated state of the secondary coordination plays a vital role in the reduction of both NO_3^- and NO_2^-.

In an effort to determine the products of these reactions, the headspace analysis via FTIR was taken after complete reaction of [Fe(Hdidpa)$(CO)_2$][PF_6] with $TBANO_3$. The results showed that NO gas is not

one of the products produced in the reaction. Ion chromatography of the reaction solution was also analyzed. The results showed the presence of NO_3^- after complete reaction of $[Fe(Hdidpa)(CO)_2][PF_6]$ with $TBANO_3$.The ion chromatography results provide enough information to determine how much NO_3^- is not being used up in the reaction. However, these experiments are ongoing.

The DNIC reaction will be further studied to determine the remaining products which will in turn allow us to determine the mechanism of the DNIC formation. Protonation of the secondary coordination sphere in the DNIC will also allow us to explore the effects that modulating the secondary coordination sphere has on the reactivity of the DNIC.

Experimental

General Methods. All air sensitive experiments were performed using standard Schlenk procedures or in an MBraun glovebox under N_2 atmosphere. Reagents were purchased from commercial sources and used as received with the exception of *N*,*N*-(diisopropyl)ethylenediamine, which was distilled immediately before use. The asymmetric PDI ligand [(ArN=C(CH_3))C_2H_3N((CH_3)C=O] (Ar =2,6-^{i}Pr-C_6H_3) was synthesized according to a literature procedures.[39] All solvents used here were dried and deoxygenated with a PureSolv solvent purification system (CuO and alumina columns). Infrared spectra were recorded on a *Thermo Scientific Nicolet iS10* FT-IR spectrometer equipped with an ATR accessory. Gas infrared spectra were obtained on a *Thermo Scientific Nicolet 6700* spectrometer equipped with a deuterated triglysine sulfate (DTGS) detector using 10 mm NaCl windows. ^{1}H and ^{13}C NMR spectra were recorded on a Unity Inova 500 MHz FT-NMR and Bruker 500 MHz FT-NMR spectrometer. Unless otherwise noted, the data are reported in ppm, using the solvent resonance as the internal standard. The solution magnetic susceptibilities were calculated using Evan's method NMR measurements.[60] Solid-state magnetic susceptibilities were recorded on a Johnson Matthey MSB-1 magnetic susceptibility balance, calibrated with $HgCo(SCN)_4$. Diamagnetic correction factors were calculated from Pascal's constants.[105] Elemental analyses were performed by ALS in Tucson, AZ. UV-Vis absorbance spectra were obtained using a Jasco UV-Vis/NIR spectrometer in 1 cm quartz cuvette.

^{1}H NMR Titrations. In a typical experiment, a sample of Fe(^{15c5}PDI)$(CO)_2$ (45 mmol) in CD_3CN (600 μL) was added to a sealable NMR tube with an injectable screw cap. Either $NaPF_6$ or $LiPF_6$ in CD_3CN were titrated in the sealed NMR tube in varying aliquots. The resulting mixture was vigorously shaken for 15 s and inserted into the NMR probe where it was allowed to equilibrate at 298 K for 10 min before a spectrum was obtained. The process was repeated until the titration was complete.

^{1}H NMR titrations. In a typical experiment, a sample of either [Zn(Hdidpa)Cl_2][PF_6] or [Zn(Hdidpa)Br_2][PF_6] (14 mmol) in CD_2Cl_2 (600 μL) was added to a sealable NMR tube with an injectable screw cap. A hydrogen

bond acceptor such as DMF-d_7 was titrated in the sealed NMR tube in varying aliquots. The resulting mixture was vigorously shaken for 15 seconds and inserted into the NMR probe where it was allowed to equilibrate at 298 K for 10 minutes before a spectrum was obtained. The process was repeated until the titration was complete.

p*K*a Determination. p*K*a values in acetonitrile were determined by NMR spectroscopy and are the average of three self-consistent trials. In a typical experiment, 10.7 mg (0.0183 mmol) of $[Zn(Hdidpa)Cl_2][PF_6]$ (**6**) was combined with 1.61 mg (0.0159 mmol) of triethylamine (pK_a = 18.82) and dissolved with CD_3CN. The solution was transferred to an NMR tube and allowed to equilibrate for 60 min. before obtaining an NMR spectrum. The chemical shifts were measured using tetramethylsilane (TMS) as the internal standard. The equilibrium populations were determined by NMR, and the equilibrium concentration was determined from using the equation $\chi_A = (\delta_{eq} - \delta_B)/(\delta_A - \delta_B)$, where χ_A is the mole fraction of the conjugate acid, and δ refers to the measured chemical shift of a given peak at equilibrium (eq) and for pure samples of the conjugate acid (A) and base (B). Once the equilibrium concentrations were obtained, the p*K*a value was calculated utilizing Hess's law.

UV-Vis Titrations*.* In a glove box, $Zn(didpa)Cl_2$ stock solutions were diluted to the desired concentration and the solution was transferred to a septum-sealed cuvette and removed from the glove box. NBu_4OH stock solutions were prepared and were added to the septum-sealed cuvettes.

Mössbauer Spectra. Mössbauer spectra were recorded at room temperature with a constant-acceleration spectrometer (Wissel GMBH, Germany) in a horizontal transmission mode using a 50 mCi ^{57}Co source. Approximately 0.080 g of sample was crushed in a Mössbauer sample holder and a drop of Paratone-N was used to cover the sample to prevent oxidation. Data acquisition varied from 2 days to 7 days to get a statistically reasonable spectrum for each sample to analyze. The velocity scale was normalized with respect to metallic iron at room temperature; hence all isomer shifts were recorded relative to metallic iron. The Mössbauer spectra were fitted by assuming Lorentzian line shapes using the NORMOS (Wissel

GMBH) least-square fitting program. The isomer shifts and quadrupole splitting parameters were determined from the fitted spectra.

Electrochemistry. Cyclic voltammetry was carried out using a Pine Wavenow potentiostat with a standard three-electrode electrochemical cell consisting of a glassy carbon working electrode, a platinum auxiliary electrode, and a freshly prepared Ag/Ag^+ reference electrode with a vycor tip filled with acetonitrile. All potentials were internally referenced to the ferrocene redox couple. Unless otherwise noted, experiments were carried out under a dinitrogen atmosphere at room temperature using 0.001 M methylene chloride, THF, or acetonitrile solutions of the analyte and 0.100 M tetra(*n*-butyl)ammonium hexafluorophosphate ($TBAPF_6$) as the supporting electrolyte. All reversibility studies were carried out at 50, 100, 150, 200 and 250 mV/s.

Computational Methods

Molecular geometries were optimized and hydrogen bond strengths computed using density functional theory (DFT) within the Perdew–Burke–Ernzerhof (PBE) functional,[106] using the VASP package[107] and projector augmented wave (PAW) potentials.[108] DFT-PBE has been shown to capture hydrogen bond strengths with an error of about 1 kcal/mol.[109] A plane-wave cutoff of 400 eV was used throughout. In each of these calculations, an isolated molecule or ion was placed in a large cubic unit cell, surrounded by approximately 12 Å of vacuum space or more in all directions. Dipole corrections to the total energy were used to account for interactions introduced by periodic boundary conditions.

Crystallographic Data Collection and Structure Determination

Diffraction intensities for **3-10** were collected at 173(2) K, 200(2) K, and 223(2) K on a Bruker Apex CCD diffractometer using MoKα radiation λ = 0.71073 Å or CuKα radiation λ = 1.54178 Å. Space groups were determined based on systematic absences. Absorption corrections were applied by SADABS.[110] Structures were solved by direct methods and Fourier techniques and refined on F^2 using full matrix least-squares procedures. All non-H atoms were refined with anisotropic thermal parameters. All

H atoms in **7** and **9** and H atoms at the N atoms in **6** and **8** involved in N–H···Cl H-bonds were found in the residual density and refined with isotropic thermal parameters. All other H atoms in the investigated structures were refined in calculated positions in a rigid group model. Crystals of **3**, **6**, and **8** were very thin plates, and diffraction intensities at the high angles were very weak. Diffraction at high angles for **2** was weak as well. In all cases, diffraction data were collected up to $2\theta_{max} = 56°$, but only reflections with $2\theta_{max} = 48°$ (**6**) and 50° (**3**, **5**, and **8**) were involved in the final refinements. Diffraction data for **5** were collected up to $2\theta_{max} = 133°$, but only reflections with $2\theta_{max} = 120°$ were involved in the final refinements. Even with such restrictions, X-ray diffraction data provide an appropriate ratio of number of measured reflections per refined parameters. The refinement shows that a solvent pentane molecule in **8** and a solvent OEt_2 molecule in **7** are disordered around inversion centers. The solvent pentane molecule in **8** is partially occupied in its position; there is $0.25(C_5H_{12})$ per the main cation/anion pair. These disordered solvent molecules were treated by SQUEEZE.[111] The corrections of the X-ray data by SQUEEZE are 51 electron/cell vs the required value of 42 electron/cell in **10** and 85 electron/cell vs the required value of 84 electron/cell in **8**. The Flack parameter in **10** is 0.008(8). All calculations were performed by the Bruker SHELXTL (v. 6.10) package.[2]

Crystallographic Data Collection for ^{15c5}PDI complexes. Diffraction intensities for **12**, **13** and **14** were collected at 173 K on a Bruker Apex2 CCD diffractometer using MoKα radiation λ = 0.71073 Å. Space groups were determined based on systematic absences (**13** and **14**) and intensity statistics (**12**). Absorption corrections were applied by SADABS. Structures were solved by direct methods and Fourier techniques and refined on F^2 using full matrix least-squares procedures. All non-H atoms were refined with anisotropic thermal parameters. H atoms in all structures were refined in calculated positions in a rigid group model. Solvent Et_2O molecule in **14** highly disordered over inversion centers was treated by SQUEEZE[111]; corrections of the X-ray data by SQUEEZE (88 electron/cell) is close to the S5 required value of 84 electron/cell for two Et_2O solvent molecules in the full unit cell. Solvent CH_2Cl_2 molecule in **3** was

refined with restrictions; the value of 1.73 Å was used as a target in the refinement for corresponding C-Cl bonds. For all crystals diffraction at high angles relatively weak due to flexibility of the O_5-macrocycle in the crystal structures. All diffraction data were collected up to $2\vartheta max = 56.0°$, but only reflections with $2\vartheta max = 50.0°$ have been used in the refinement. As it can be expected in all the structures there are significant elongations for atom thermal parameters in the O_5-macro-cycle due to its flexibility. It was found that the compound $FeCl_2L(O_5(C_2H_4)_5)$ (**1**) has a structure similar that for **12**, but O_5-macrocycle in this structure is highly disordered and we could not find solution for this disorder. All calculations were performed by the Bruker SHELXL-2013 package.[112]

Didpa (2). The ligand $[(2,6\text{-}^{i}PrC_6H_3)N{=}CMe)(N(^{i}Pr)_2C_2H_4)N{=}CMe)C_5H_3N]$ (didpa) was synthesized with starting materials $[(2,6\text{-}^{i}PrC_6H_3)N{=}CMe)(O{=}CMe)C_5H_3N]$ (1.0 g, 3.10 mmol) and an excess of N,N-diispropylethylenediamine (4.14 g,28.70 mmol) in a 20-mL pressure vial. The vial was heated in silicon oil at 80 ˚C for 48 hours, yielding a dark yellow solution. The solution was transferred to a 50 mL round bottom flask where 10 mL of dry methanol was added and placed in the freezer for 6 hours. The resulting pale yellow solid was filtered in a Buchner funnel and washed with cold methanol. FTIR: 1640 cm^{-1} (C=N). ^1H NMR, 500 MHz (CD_2Cl_2)

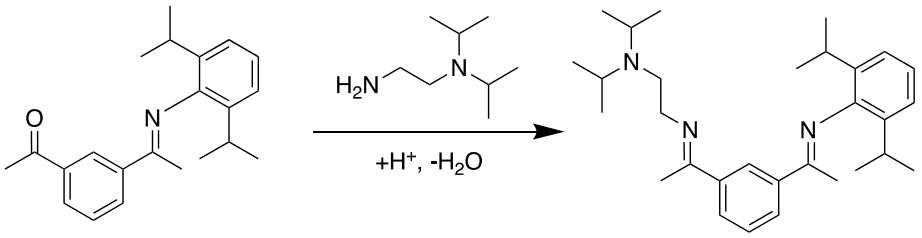

Zn(didpa)Cl_2 (3). The didpa ligand (0.50 g, 1.12mmol) was dissolved in approximately 10 mL of CH_2Cl_2. One equivalent of $ZnCl_2$ (0.15 mg, 1.12 mmol) and stir bar were added to the pale yellow solution. The solution was allowed to stirred overnight, yielding a cloudy yellow-orange solution. The solvent was removed by *in vacuo*, redissolved in CH_2Cl_2, and layered with diethyl ether. Yellow-orange crystals resulted in 95% yield (2.48 g, 4.24 mmol). FTIR (ATR): 1639, 1585 cm^{-1} (C=N). ^1H NMR (500 MHz, CD_2Cl_2)

δ 8.59 (t, 1H), 8.42 (d, 1H), 8.38 (d, 1H), 7.31 (m, 3H), 3.83 (t, 2H), 8.70 (m, 2H), 2.84 (m, 4H), 2.43 (s, 3H), 2.25 (s, 3H), 1.15 (t, 12 H), 1.06 (d, 12 H). ^{13}C NMR (500 MHz, CD_2Cl_2) δ 15.3, 18.7, 20.6, 22.5, 22.9, 24.1,

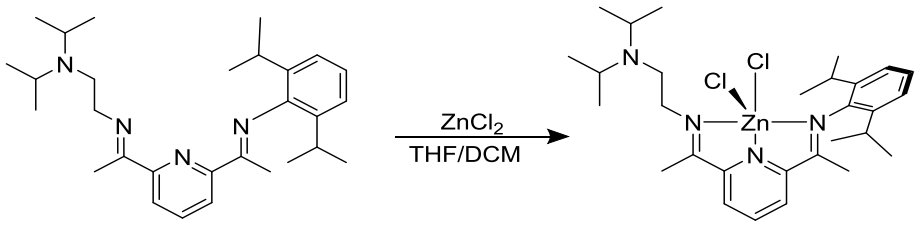

24.6, 28.21, 44.9, 122.9, 123.8, 125.3, 125.6, 126.1, 138.9, 142.3, 143.4, 148.3, 149.7, 164.3 (C=N). Anal. Calc'd for $C_{29}H_{44}Cl_2ZnN_4$: C, 59.54; H, 7.58, N, 9.58. Found: C, 59.79; H, 7.08; N, 9.55

Zn(didpa)Br$_2$ (4). A 20 mL scintillation vial was charged with **2** (0.50 g, 1.12 mmol), approximately 10 mL of CH_2Cl_2, $ZnBr_2$ (0.25 g, 1.12 mmol), and a stir bar. The resulting yellow-orange solution stirred overnight forming a yellow solution with a yellow/orange precipitate. The solvent was removed *in vacuo* and redissolved in 5 mL of CH_2Cl_2. The solution was layered with diethyl ether for 1 day resulting in yellow/orange crystals identified as **4** (88% yield) (0.53 g, 0.98 mmol). FTIR (ATR): 1636, 1584 cm^{-1} (C=N). ^{1}H NMR (500 MHz, CD_2Cl_2) δ 8.43 (t, 1H), 8.21 (d, 2H), 7.26 (s, 3H), 4.07 (t, 2H), 3.01 (m, 6H), 2.63 (s, 3H), 2.37 (s, 3H), 1.30 (t, 6 H), 1.03 (d, 18 H). ^{13}C NMR (500 MHz, CD_2Cl_2) δ 164.6 (C_1=N_1), 161.7 (C_2=N_2), 149.3147.9, 143.7, 142.4, 138.9, 126.1, 125.9, 125.7, 123.8, 52.2, 49.1, 45.4, 28.4, 24.6, 24.5, 20.7, 19.2, Anal. calcd for $C_{29}H_{44}Br_2ZnN_4$: C, 51.69; H, 6.58; N, 8.31. Found: C, 52.05; H, 7.08; N, 8.03.

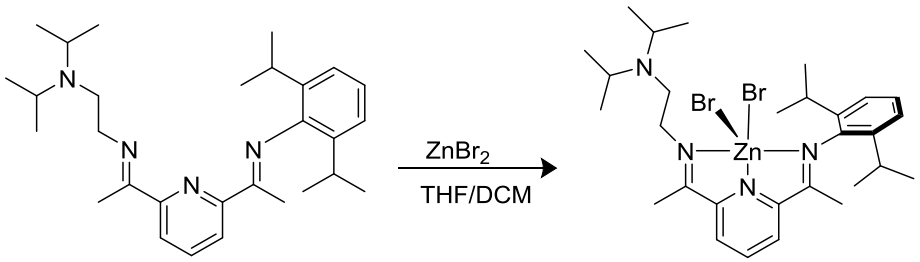

Fe(didpa)Cl_2 (5). In a 20 mL scintillation vial, the didpa ligand (0.400 g, 0.892 mmol) was dissolved in approximately 9 mL CH_2Cl_2. A solution of $FeCl_2$ (0.113 g, 0.892 mmol) in 1 mL THF and a stir bar were added to the vial. The resulting blue solution was stirred overnight. The solvents were removed *in vacuo* yielding a blue solid. The solid was redissolved with approximately 5 mL of CH_2Cl_2 and then filtered through a celite plug into a scintillation vial. The filtrate was carefully layered with pentane and set aside for one day, after which blue crystals of **5** were isolated in 78% yield (0.400 g, 0.696 mmol). FTIR (ATR): 1620, 1581 cm^{-1} (C=N). ^1H NMR (500 MHz, CD_2Cl_2) δ −23.51 (s, 2H), −15.35 (s, 2H), −3.70 (s, 9H), −2.49 (s, 5H), −1.35 (s, 1H), 1.81 (s, 6H), 17.64 (s, 1H), 41.62 (s, 1H), 78.53 (s, 1H), 83.44 (s, 1H), 157.27 (s, 1H). μ_{eff}: 5.8 μB (solid); 5.7 μB (solution). Anal. Calc'd for $C_{29}H_{44}Cl_2FeN_4$: C, 60.53; H, 7.71; N, 9.74. Found: C, 60.17; H, 7.77; N, 9.62μeff: 5.75 μ_B (solid); 5.68 μ_B (solution). Anal calcd for $C_{29}H_{44}Cl_2FeN_4$: C, 60.53; H, 7.71; N, 9.74 Found: C, 60.17; H, 7.77; N, 9.62.

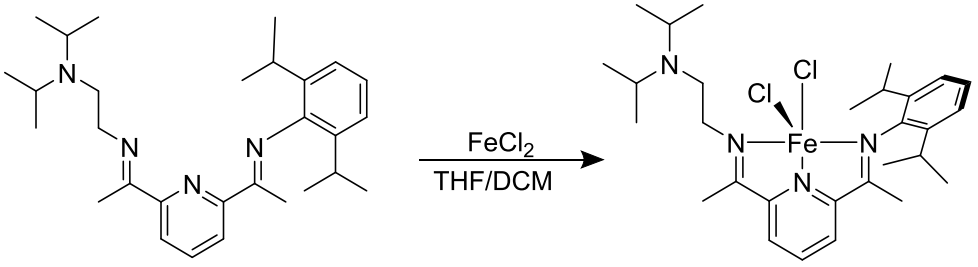

[Zn(Hdidpa)Cl_2][PF_6] (6). In a scintillation vial equipped with a stir bar, complex **3** (0.100 g, 0.137 mmol), was dissolved in approximately 5 mL CH_2Cl_2. In a separate 20 mL scintillation vial, NH_4PF_6 (56.8 mg, 0.342 mmol) was dissolved in approximately 3 mL dry CH_3OH and allowed to stir. After stirring for 10 min., the solution of NH_4PF_6 in CH_3OH was added to the scintillation vial containing **3**. The resulting yellow-orange solution was stirred overnight. The solvents were removed *in vacuo*, producing a yellowish orange solid. The solid was redissolved with approximately 5 mL of CH_2Cl_2 and then filtered through a celite plug. The filtrate was layered with diethyl ether and the vial was placed in freezer for 48 h to crystallize. The resulting yellowish orange crystals were identified as [Zn(Hdidpa)Cl_2][PF_6] **(6)** (89% yield) (0.089 g, 0.122 mmol). FTIR (ATR): 1642, 1586 cm−1 (C=N); 832 cm−1 ($PF6^-$). ^1H NMR (500 MHz,

CD2Cl2) δ 8.60 (t, 1H), 8.50 (s, 1H), 8.46 (d, 1H), 8.36 (d, 1H), 7.33 (m, 3H), 4.37 (t, 2H), 3.86 (sep, 2H), 3.74 (t, 2H), 2.90 (sep, 2H), 2.75 (s, 3H), 2.45 (s, 3H), 1.46 (m, 12 H), 1.30 (d, 6 H), 1.06 (d, 6 H). ^{13}C NMR (500 MHz, CD_3CN) expected: 20; reported, 19; δ 15.3, 18.7, 23.7, 24.26, 28.1, 46.8, 47.0, 55.9, 97.3, 124.1, 126.7, 127.4, 128.0, 139.5, 144.4, 147.8, 148.6, 167.7 (C_1=N_1), 167.9 (C_2=N_2). Anaytical. Calc'd for $C_{29}H_{45}Cl_2F_6ZnN_4P$: C, 47.65; H, 6.21; N, 7.67. Found: C, 47.25; H, 6.02; N, 7.64.

[Zn(Hdidpa)Br$_2$][PF$_6$] (7). A 20-mL scintillation vial was charged with **5** (0.100 g, 0.122 mmol), approximately 5 mL CH_2Cl_2, and stir bar. In a separate 20 mL scintillation vial, NH_4PF_6 (40.0 mg, 0.245 mmol) was dissolved in approximately 3 mL dry CH_3OH and stirred. After stirring for 10 min., the solution of NH_4PF_6 in CH_3OH was added to the vial of **4**. The resulting yellowish orange solution was stirred overnight. The solvents were removed *in vacuo*, producing a yellowish orange solid. The solid was redissolved with approximately 5 mL of CH_2Cl_2 and filtered through a celite plug. The filtrate was layered with diethyl ether and the vial was placed in freezer for 48 h to allow for crystallization. The yellow/orange crystals formed were identified as **7** (95% yield) (0.0950 g, 0.116 mmol). FTIR (ATR): 1644, 1591 cm^{-1} (C=N); 835 cm^{-1} (PF_6^-). ^{1}H NMR (500 MHz, CD_2Cl_2) δ 8.55 (t, 1H), 8.41 (d, 1H), 8.32 (d, 1H), 7.78 (s, 1H) 7.28 (m, 3H), 4.37 (t, 2H), 3.83 (t, 2H), 3.71 (m, 2H), 2.90 (sep, 2H), 2.72 (s, 3 H), 2.42 (s, 3H), 1.40 (d, 12H), 1.28(d, 6H), 1.03 (d, 6H). $_{13}$C NMR (500 MHz, CD_2Cl_2) expected: 20; reported, 19; δ 167.3 (C_1=N_1), 166.6 (C_2=N_2), 148.8, 147.7, 144.6, 141.1, 139.3, 127.3, 127.1, 126.9, 124.2, 56.3, 47.4, 46.8, 28.5, 24.6, 19.3, 18.5, 17.2, 16.3. Anal. calcd for $C_{29}H_{45}Br_2F_6ZnN_4P$: C, 42.49; H, 5.53; N, 6.83. Found: C, 42.25; H, 5.32; N, 6.97.

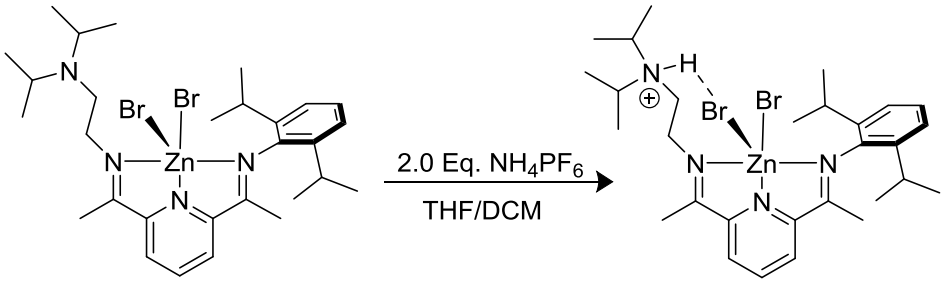

[Fe(Hdidpa)Cl_2][PF_6] (8). In a 20 mL scintillation vial, **5** (0.100 g, 0.174 mmol) was dissolved in approximately 5 mL CH_2Cl_2. With stirring, a solution of NH_4PF_6 (56.7 mg, 0.348 mmol) dissolved in 3 mL of CH_3OH was added to the solution of **5**. The solution was stirred overnight. The solvents were removed *in vacuo* and redissoved in approximately 5 mL of CH_2Cl_2. After being filtered through a celite plug into a clean 20 mL scintillation vial, the filtrate was layered with pentane and stored in the freezer for 24 h to crystallize **8** in 92% yield (0.115 g, 0.160 mmol). FTIR (ATR): 1623, 1582 cm^{-1} (C=N); 833 cm^{-1} (PF_6^-). ^{1}H NMR (500 MHz, CD_2Cl_2) δ -23.51 (s, 2 H), -15.35 (s, 2H), -3.70 (s, 9H), -2.49 (s, 5H), -1.35 (s, 1H), 1.81 (s, 6H), 17.64 (s, 1H), 41.62 (s, 1H), 78.53 (s, 1H), 83.44 (s, 1H), 157.27 (s, 1H). μ_{eff}: 4.77 μ_B (solid); 4.70 μ_B (solution). Anal calcd for $C_{29}H_{45}Cl_2F_6FeN_4P$: C, 48.28; H, 6.29; N, 7.77. Found: C, 47.03; H, 6.56; N, 7.47.

Fe(didpa)$(CO)_2$ (9). In a nitrogen filled MBraun glovebox, a Fisher Porter tube was charged with complex **5** (0.150 g, 0.261 mmol), sodium mercury amalgam (400 mg, 5%Na), a stir bar, and approximately 5 mL of CH_2Cl_2 to produce a blue color solution. The tube was closed with a pressure valve and charged with 20 psi of CO and left to stir vigorously overnight. The solvent was then removed *in vacuo*, redissolved with approximately 10 mL of Et_2O, and filtered through a glass wool, celite plug. Slow evaporation of Et_2O resulted in dark green crystals of **9** (65% yield) (0.0950 g, 0.170 mmol). FTIR (ATR): 1940, 1872 cm^{-1} (C=O). ^{1}H NMR (500 MHz, CD_2Cl_2) δ 8.07 (q, 3H), 7.51 (t, 1H), 7.25 (m, 2H), 4.25 (t, 2H), 3.10 (sep, 2H), 2.88 (t, 2H), 2.73 (s, 3H), 2.51 (sep, 2H), 2.36 (s, 3 H), 1.26 (d, 6 H), 1.05 (d, 18 H). ^{13}C NMR (500 MHz, CD_2Cl_2) δ 214.9 (C=O), 155.8 (C_1–N_1), 155.166 (C_2–N_2), 149.8, 145.8, 140.3, 126.0, 123.2, 120.8, 119.9, 117.2, 62.7, 48.9, 47.8, 27.2, 24.4, 20.0, 20.7, 16.3, 14.3. Anal. calcd for $C_{31}H_{44}O_2FeN_4$: C, 66.42; H, 7.91; N, 9.99. Found: C, 66.32; H, 8.01; N, 9.72.

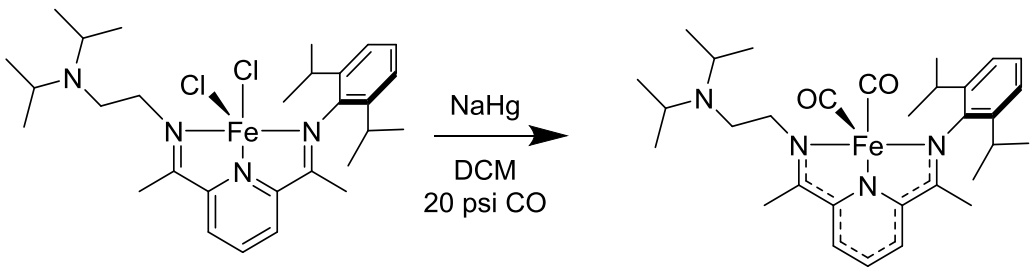

[FeH(didpa)(CO)$_2$][PF$_6$] (10). A 20 mL scintillation vial was charged with **9** (0.150 g, 0.231 mmol) and dissolved in approximately 5 mL of CH_2Cl_2. In a separate 20 mL scintillation vial, NH_4PF_6 (75.2 mg, 0.461 mmol) dissolved in 3 mL of dry CH_3OH was stirred for 10 min. Both solutions were then mixed together and stirred overnight. The solvents were removed *in vacuo* and the resulting solid was redissolved in CH_2Cl_2. The solution was filtered through celite into a clean scintillation vial, and then carefully layered with ether to allow for crystallization. The resulting dark green crystals were washed with ether and dried under vacuum. (80% yield) (0.130 g, 0.184 mmol). FTIR (ATR): 1946, 1879 cm^{-1} (C=O), 831 cm^{-1} (PF_6^-). ^{1}H NMR (500 MHz, CD_2Cl_2) δ 8.18 (m, 2H), 7.60 (m, 1H), 7.35 (t, 1H), 7.28 (d, 2H), 4.65 (m, 2H), 3.82 (m, 2H), 3.48 (m, 2H), 2.75 (s, 3H), 2.51 (m, 5H), 1.51 (d, 12H), 1.27 (m, 6 H), 1.06 (d, 6 H). ^{13}C NMR (500 MHz, CD_2Cl_2) δ 214.9 (C=O), 158.1 (C_1−N_1), 156.3 (C_2−N_2), 149.2, 145.5, 145.1, 140.1, 126.5, 123.6, 122.1, 121.5, 118.5, 48.4, 27.3, 24.4, 23.9, 16.6, 14.5. Anal. calcd for $C_{31}H_{45}F_6O_2FeN_4P$: C, 52.70; H, 6.42; N, 7.93. Found C, 52.01; H, 6.70; N, 7.53.

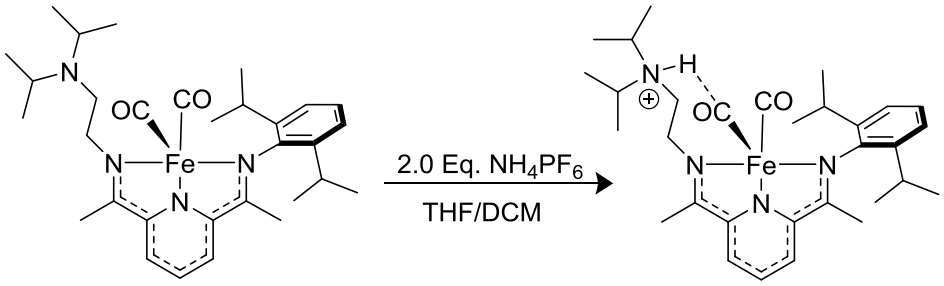

Fe(15c5PDI)Cl$_2$ (11). In an N_2 filled MBraun glovebox, a 100 mL Schelnk flask equipped with a stir bar was charged with the asymmetric PDI ligand [(ArN=C(CH_3))C_2H_3N((CH_3)C=O] (0.250 g, 0.775 mmol) and $FeCl_2$ (98.3 mg, 0.775 mmol). Approximately 20 mL of ethanol was added to the round bottom Schlenk flask. The solution was heated to 80 ˚C for 30 min under N_2 gas while stirring. A solution of 2-Aminomethyl-15-crown-5 (193 mg, 0.775 mmol) dissolved in approximately 10 mL of ethanol was slowly syringed into the flask and the solution was left to heat at 80 ˚C for 12 h under N2 gas. The solvent was removed *in vacuo*, yielding a dark blue solid. Back in the glovebox, the resulting solid was redissolved in 5 mL of CH_2Cl_2 and

filtered through a celite plug. The filtrate was carefully layered with pentane in order to obtain the dark blue crystals identified as Fe(^{15c5}PDI)Cl_2 (**11**) (90% yield). Anal Calc'd for $C_{32}H_{47}Cl_2FeN_3O_5$: C, 56.48; H; 6.96; N, 6.18. Found: C, 56.67; H; 7.13; N, 6.48.

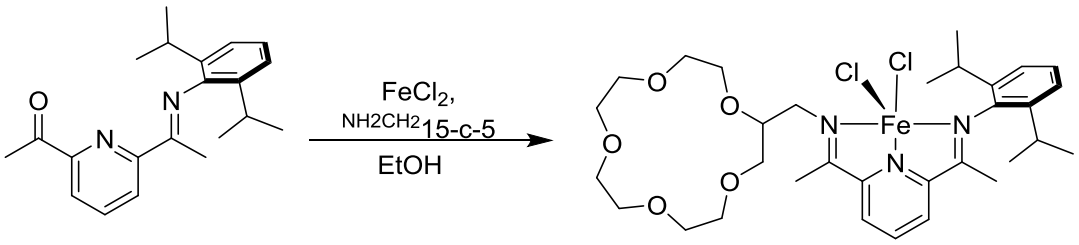

Fe(^{15c5}PDI)$(CO)_2$ (12). In a nitrogen filled MBraun glovebox, a Fisher Porter tube was charged with complex complex **11** (0.150 g, 0.225 mmol), sodium mercury amalgam (400 mg, 5%Na), a stir bar, and approximately 5 mL of CH_2Cl_2 to produce a blue color solution. The tube was closed with a pressure valve and charged with 20 psi of CO and left to stir vigorously overnight. The solvent was removed *in vacuo* and brought back into the glovebox. The resulting green solid was redissolved in 5 mL of diethyl ether and filtered through a celite plug. Slow evaporation of the diethyl ether solution resulted in dark green crystals identified as (**12**) in 90% yield (0.135 g, 0.203 mmol). FTIR (ATR): 1946, 1882 cm^{-1} (C=O). ^{1}H NMR (500 MHz, CD_3CN) δ 8.11 (q, 2H), 7.52 (t, 1H), 7.24 (m, 3H), 4.45(q, 2H), 4.15 (q, 2H), 4.05 (m, 1H),3.56 (m, 17H), 2.72 (s, 3H), 2.52 (sep, 1H), 2.28 (s, 3H), 1.20 (m, 6H), 1.0 (m, 6H). ^{13}C NMR (500 MHz, CD_3CN) δ 14.57, 15.79, 23.54, 23.62, 23.91, 27.24, 62.36, 71.40, 82.54, 118.02, 121.03, 121.87, 123.43, 126.21, 139.92, 140.39, 144.39, 145.97, 149.73, 155.51, 158.85, 212.99, 216.99. Anal Calc'd for $C_{34}H_{47}FeN_3O_7$: C, 61.35; H, 7.12; ; N, 6.31. Found: C, 61.05; H; 7.28; N, 6.57.

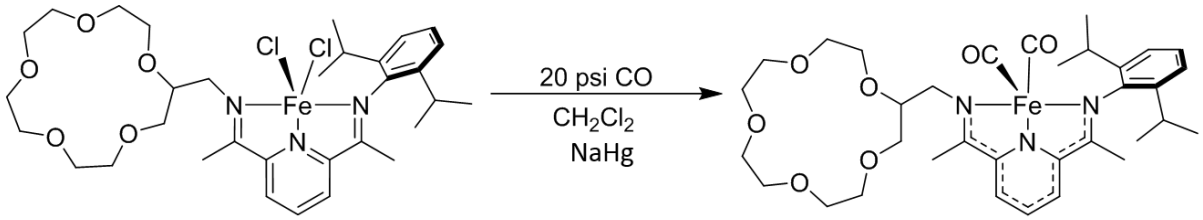

[Fe(^{15c5}PDI)(CO)$_2$ Li][PF$_6$] (13). A 20 mL scintillation vial was charged with compound (**12**) (0.100 g, 0.150 mmol), LiPF$_6$ (0.023 g, 0.150 mmol), a stir bar, and approximately 2 mL of CH$_3$CN were added to a 20 mL scintillation vial. The dark green solution was stirred overnight. The solvent was removed *in vacuo* and then redissolved in 5 mL of CH$_2$Cl$_2$ before being filtered through Celite. The solution was carefully layered with pentane and set aside for crystallization, yielding dark green crystals identified as [Fe(^{15c5}PDI)(CO)$_2$ Li][PF$_6$] (**14**) in 70% yield (0.070 g, 0.086 mmol). FTIR (ATR): 1931, 1866 cm^{-1} (C=O), 824 cm^{-1} (PF$_6^-$). ^{1}H NMR (500 MHz, CD$_3$CN) δ 8.17 (d, 2H), 7.58 (t, 1H), 7.27 (m, 3H), 4.50 (q, 2H), 4.29 (q, 2H), 4.25 (m, 1H), 3.61 (m, 17H), 2.72 (s, 3H), 2.54 (sep, 1H), 2.30 (s, 3H), 1.21 (d, 6H), 1.00 (d, 6H). ^{13}C NMR (500 MHz, CD$_3$CN) δ 14.33, 14.39, 23.39, 23.32, 23.53, 23.60, 23.69, 23.76, 24.07, 24.00, 27.18, 27.23, 27.29, 60.28, 68.02, 68.65, 68.79, 79.86, 122.12, 123.49, 126.39, 139.75, 139.82, 140.31, 140.37, 144.48, 149.53, 156.66, 158.19, 212.66, 217.16. Anal. Calcd for C$_{34}$H$_{47}$F$_6$FeN$_3$LiO$_7$P: C, 49.95; H, 5.80; N, 5.14. Found: C, 50.22; H, 5.97; N, 5.47.

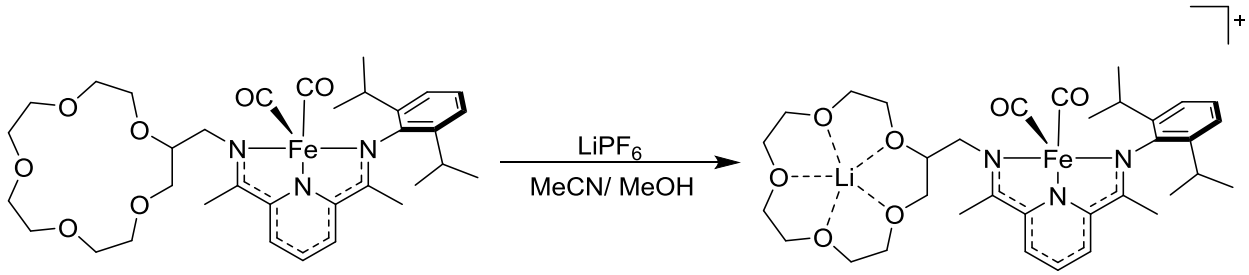

[Fe(^{15c5}PDI)(CO)$_2$ Na][PF$_6$] (14). Compound (**12**) (0.100 g, 0.150 mmol), NaPF$_6$ (0.025 g, 0.150 mmol), a stir bar, and approximately 2 mL of CH$_3$CN were added to a 20 mL scintillation vial. The dark green solution was stirred overnight. The solvent was removed *in vacuo* and then redissolved in 5 mL of CH$_2$Cl$_2$ before being filtered through a celite plug. The solution was carefully layered with pentane and set aside for crystallization, yielding dark green crystals identified as (**13**) 70% (0.070 g, 0.084 mmol) yield. FTIR (ATR): 1936, 1868 cm^{-1} (C=O), 835 cm^{-1} (PF$_6^-$). ^{1}H NMR (500 MHz, CD$_3$CN) δ 8.20 (d, 2H), 7.61 (t, 1H), 7.29 (m, 3H), 4.53 (q, 2H), 4.32 (q, 2H), 4.20 (m, 1H), 3.61(m, 17H), 2.75 (s, 3H), 2.54 (sep, 1H), 2.33 (s, 3H), 1.23

(m, 6H), 1.02 (m, 6H). ^{13}C NMR (500 MHz, CD_2Cl_2) δ 14.66, 16.18, 23.74, 24.35, 24.47, 27.29, 27.24, 59.96, 81.03, 117.97, 121.30, 121.37, 123.40, 123.45, 126.17, 139.81, 140.41, 144.89, 156.06, 158.01, 212.46, 217.28. Anal. Calcd for $C_{34}H_{47}F_6FeN_3NaO_7P$: C, 48.99; H, 5.68; N, 5.04. Found: C, 49.21; H, 5.46; N, 5.34.

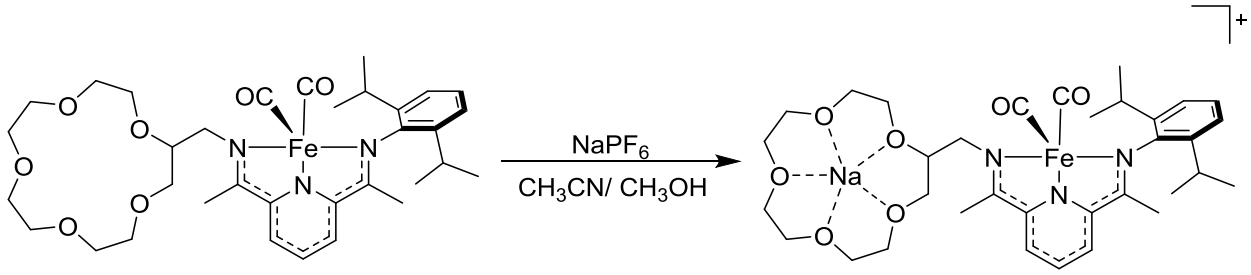

Synthesis of [Fe(Didpa)(NO)$_2$][PF$_6$] (15). Compound **10** (0.050 g, 0.071 mmol)) was dissolved in 8 mL THF and stirred for 30 min. A solution of $NaNO_2$ (0.005 g, 0.072 mmol) dissolved in 2 mL of CH_3OH was added dropwise to the green solution of **10**. The solution left to stir overnight. A color change from green to red brown is observed after stirring overnight. The solvent was removed *in vacuo*, yielding a red-brown solid. The red-brown solid was redissolved with approximately 5 mL of THF before being filtered through a pipette packed with glass wool and celite into a clean 20 mL scintillation vial. The filtrate was carefully layered with pentane placed in the glovebox freezer for 48 h resulting in dark brown crystal identified as **15** through X-ray crystallography. FTIR (ATR): 1789, 1716 cm^{-1} (NO); 837 cm^{-1} (PF_6^-). ^{57}Fe Mossbauer: δ = 0.348(5) mm/s; ΔE_Q = 0.791(7) mm/s.

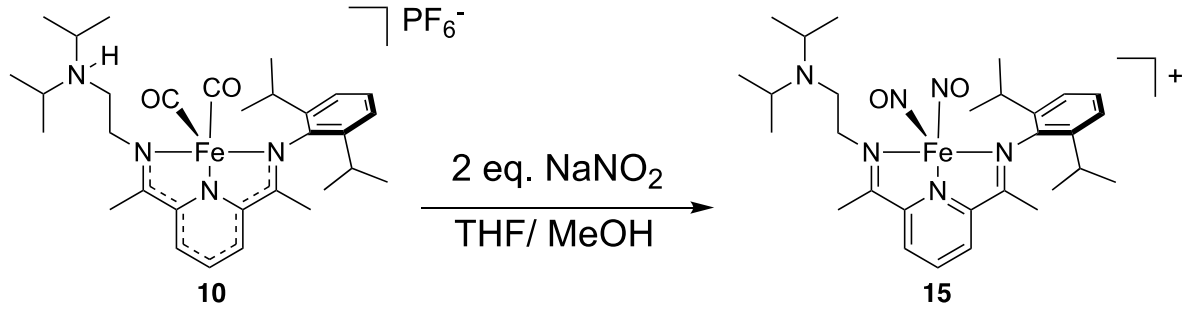

Reactivity of 10 with $Na^{15}NO_2$ to form [Fe(didpa)(^{15}NO)$_2$][PF_6] (15). Compound **10** (0.050 g, 0.071 mmol) was dissolved in 8 mL THF and stirred for 30 min. A solution of $Na^{15}NO_2$ (0.005 g, 0.072 mmol) dissolved in 2 mL of CH_3OH was added to the green solution of **10**. The solution was allowed to stir overnight. The solvents of the resulting red-brown solution was removed *in vacuo*, yielding a brown solid. The solid was redissolved with approximately 3 mL of THF and then filtered through a pipette packed with glass wool and celite. The filtrate was carefully layered with pentane for crystallization. FTIR (solid): 1755, 1684 cm^{-1} (NO); 831 cm^{-1} (PF_6^-).

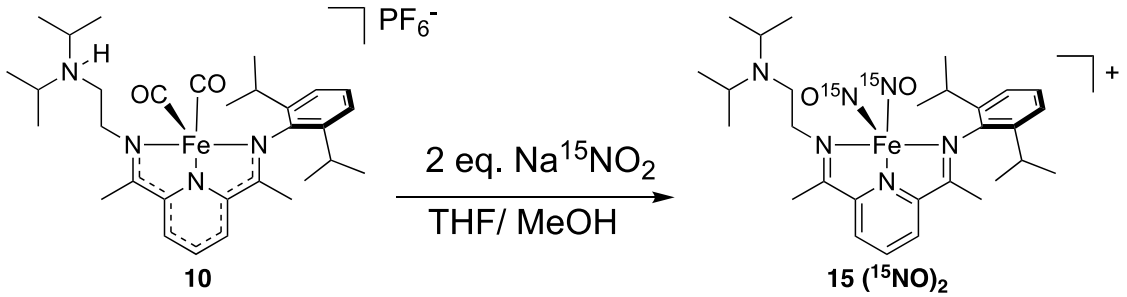

10 **15 (^{15}NO)$_2$**

Reactivity of 10 with $TBANO_3$ to form [Fe(didpa)(NO)$_2$][PF_6]. In an N_2 filled glovebox, a 20 mL pressure vial was charged with compound **10** (0.050 g, 0.071 mmol), $TBANO_3$ (0.022 g, 0.071 mmol), and 5 mL of THF. The vial was tightly closed, taken out of the glovebox, and placed in an 80 ˚C silicone-based oil bath. The solution was left for 12 hours before being brought back into the glovebox. A color change from dark green to dark brown was observed and a liquid IR of the solution was obtained. The remaining solution was transferred to a 20 mL scintillation vial and the solvents were removed *in vacuo*. The brown solids were redissolved in THF and filtered through Celite. The filtrate was layered with THF and placed in the glovebox freezer to allow for crystallization.

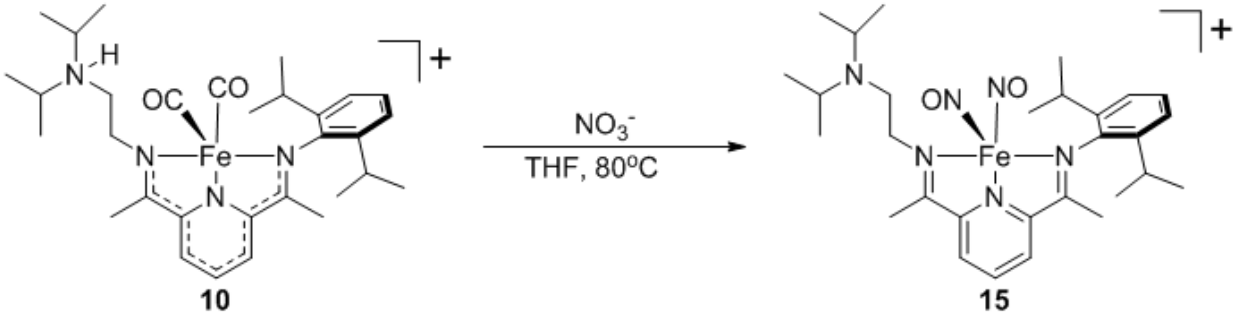

10 **15**

Reactivity of 10 with TBA$^{15}NO_3$ to form [Fe(didpa)(^{15}NO)$_2$][PF_6]. A 20 mL pressure vial was charged with compound **10** (0.050 g, 0.071 mmol), $TBANO_3$ (0.022 g, 0.071 mmol), and 5 mL of THF. The vial was placed in an 80 ˚C silicone-based oil bath overnight. A color change from dark green to dark brown was observed and a liquid IR of the solution was obtained. The remaining solution was transferred to a 20 mL scintillation vial and the solvents were removed *in vacuo*. The brown solids were redissolved in THF and filtered through Celite. The filtrate was layered with THF and placed in the glovebox freezer to allow for crystallization.

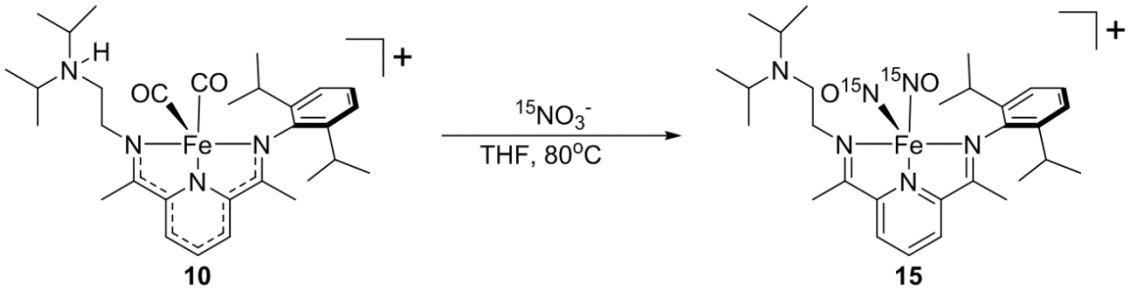

10 **15**

Reactivity of 10 with $TBANO_3$ for analysis of NO gas in the headspace. In an N_2 filled glovebox, compound **10** (0.050 g, 0.071 mmol) dissolved in approximately 5 mL of THF were added to a Fisher Porter tube. The tube was closed with a pressure valve, taken out of the box, and placed in an 80 ˚C silicone-based oil bath for 12 hours. The Fisher Porter tube and a gas IR cell (NaBr plates) were attached to a t-valve and hooked to a Schlenk line. Once the lines were evacuated and air-free, the headspace from the Fisher Porter tube was allowed to freely flow into the gas cell IR. The valve of the IR cell was closed off and a spectrum was obtained, inspecting for NO gas.

Reactivity of Fe(^{Meo}PDI)$(CO)_2$ with $TBANO_3$. The Fe(^{Meo}PDI)$(CO)_2$ complex was synthesized according to literature procedures.[12] A 20-mL pressure vial was charged with compound Fe(^{Meo}PDI)$(CO)_2$ (0.0500 g, 0.0900 mmol), $TBANO_3$ (0.0274 g, 0.0900 mmol), and 5 mL of THF. The vial was placed in an 80 ˚C silicone-based oil bath overnight. A color change from dark green to dark brown was observed and a liquid IR of the solution was obtained. The remaining solution was transferred to a 20-mL scintillation vial and the solvents were removed *in vacuo*. The brown solids were redissolved in THF and filtered through Celite.

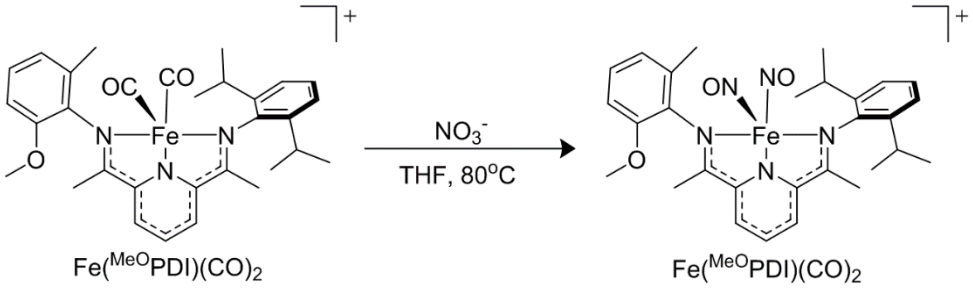

Fe(^{MeO}PDI)(CO)$_2$ Fe(^{MeO}PDI)(CO)$_2$

Crystallographic Data for **12**: $C_{34}H_{47}FeN_3O_7$, M = 665.59, 0.45 x 0.09 x 0.07 mm, T = 193(2) K, Triclinic, space group *P*-1, a = 8.6642(17) Å, b = 13.636(3) Å, c = 16.314(3) Å, α = 114.394(3)°, β = 103.191(4)°, γ = 90.234(4)°, V = 1698.6(6) Å^3, Z = 2, D_c = 1.301 Mg/m^3, μ(Mo) = 0.494 mm^{-1}, F(000) = 708, $2\vartheta_{max}$ = 50.0°, 33984 reflections, 5980 independent reflections [R_{int} = 0.0744], R1 = 0.0575, wR2 = 0.1331 and GOF = 1.006 for 5980 reflections (406 parameters) with I>2σ(I), R1 = 0.0962, wR2 = 0.1565 and GOF = 1.006 for all reflections, max/min residual electron density +1.147/-0.492 eÅ^3.

Crystallographic Data for **13**: $C_{36}H_{52}F_6FeLiN_3O_{7.5}P$, $C_{34}H_{47}F_6FeLiN_3O_7P$ 0.5($C_4H_{10}O$), M = 854.56, 0.29 x 0.17 x 0.13 mm, T = 173 K, Monoclinic, space group $P2_1/c$, a = 16.879(5) Å, b = 15.800(5) Å, c = 16.933(6) Å, β = 115.586(8)°, V = 4073(2) Å^3, Z = 4, D_c = 1.394 Mg/m^3, μ(Mo) = 0.487 mm^{-1}, F(000) = 1788, $2\vartheta_{max}$ = 50.0°, 29010 reflections, 7177 independent reflections [R_{int} = 0.0467], R1 = 0.0848, wR2 = 0.2366 and GOF = 1.023 for 7177 reflections (478 parameters) with I>2σ(I), R1 = 0.1111, wR2 = 0.2583 and GOF = 1.023 for all reflections, max/min residual electron density +1.347/-1.325 eÅ^3.

Crystallographic Data for **14**: $C_{35}H_{48}Cl_2F_6FeN_3NaO_7P$, M = 917.47, 0.26 x 0.23 x 0.21 mm, T = 173 K, Monoclinic, space group $P2_1/c$, a = 18.4136(13) Å, b = 13.6524(9) Å, c = 16.8854(12) Å, β = 91.165(2)°, V = 4243.9(5) Å^3, Z = 4, D_c = 1.436 Mg/m^3, μ(Mo) = 0.603 mm^{-1}, F(000) = 1900, $2\vartheta_{max}$ = 50.0°, 45328 reflections, 7473 independent reflections [R_{int} = 0.0484], R1 = 0.0653, wR2 = 0.1670 and GOF = 1.043 for 7473 reflections (505 parameters) with I>2σ(I), R1 = 0.1045, wR2 = 0.2048 and GOF = 1.043 for all reflections, max/min residual electron density +1.157/-0.561 eÅ^3.

Supporting Data

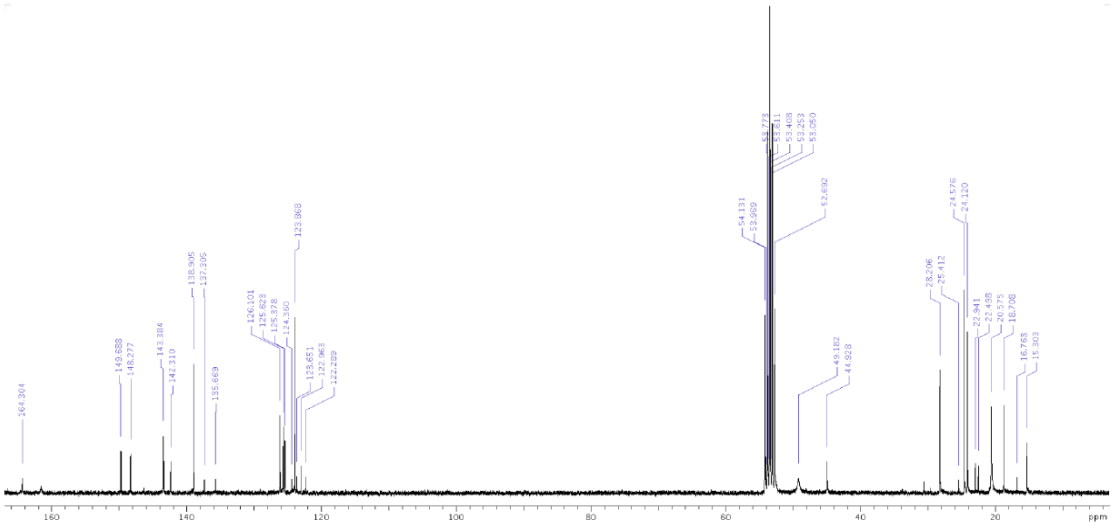

Figure S1. ^{13}C NMR of **3**, 500 MHz, CD_2Cl_2.

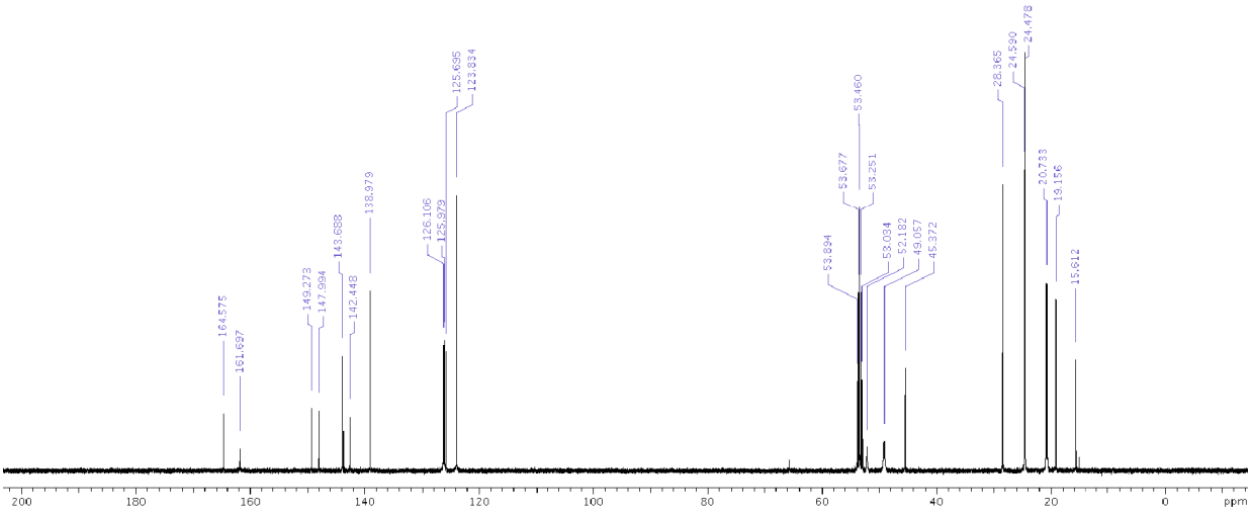

Figure S2. ^{13}C NMR of **4**, 500 MHz, CD_2Cl_2.

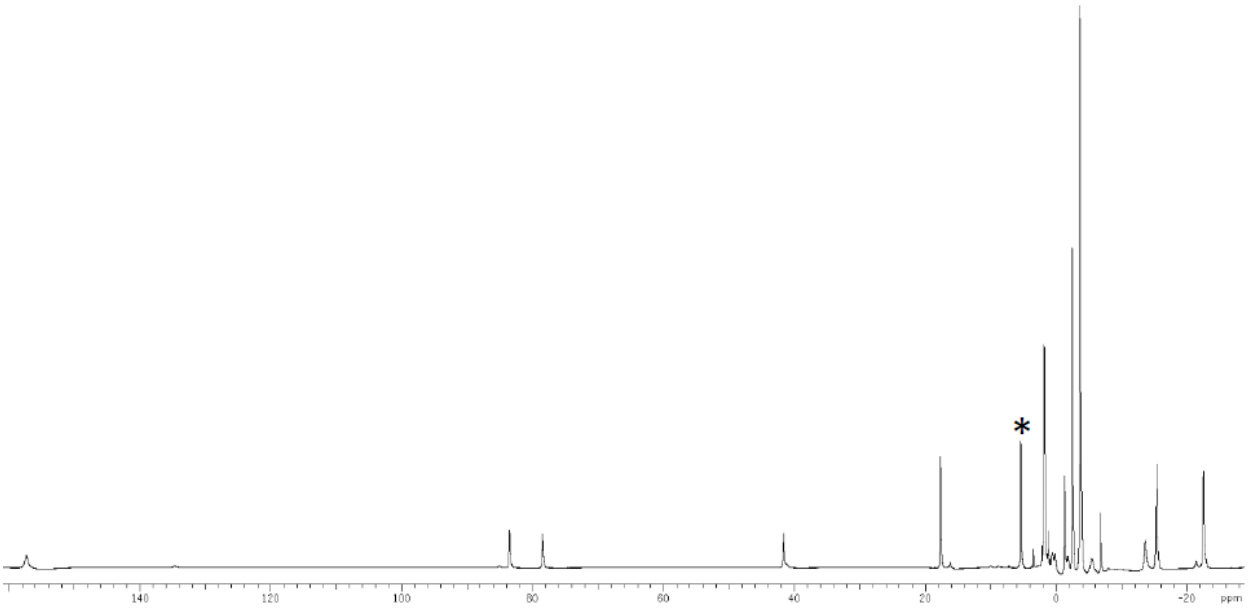

Figure S3. ^{1}H NMR of **5**, 500 MHz, CD_2Cl_2.

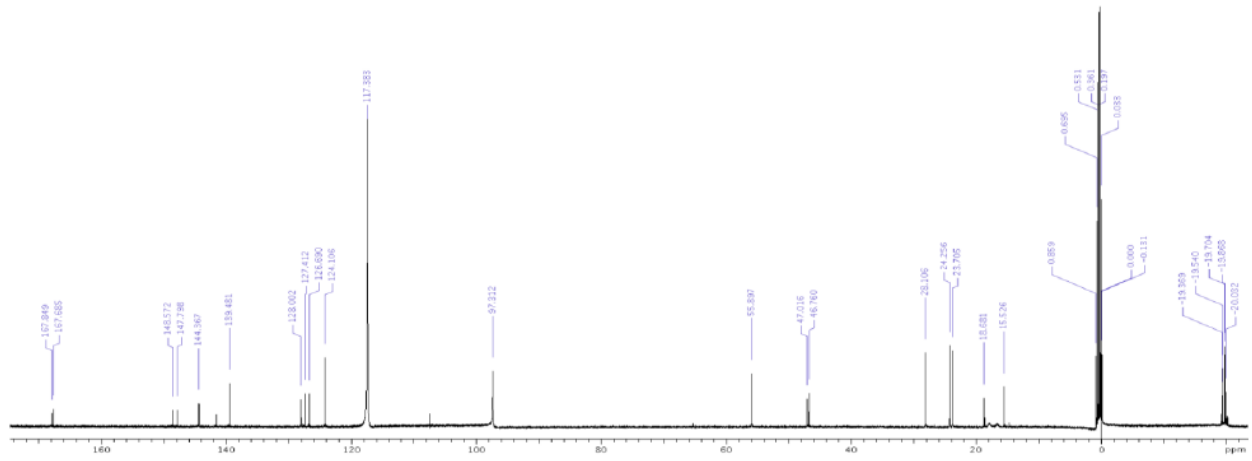

Figure S4. ^{13}C NMR of **6,** 500 MHz, CD_2Cl_2.

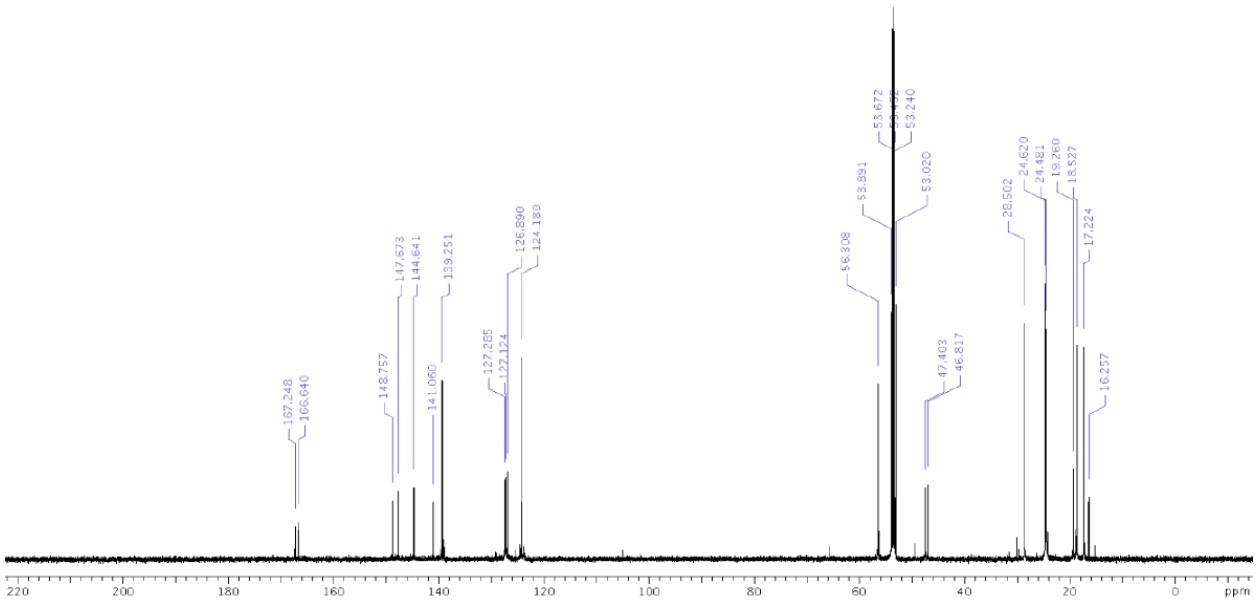

Figure S5. ^{13}C NMR of 7, 500 MHz, CD_2Cl_2.

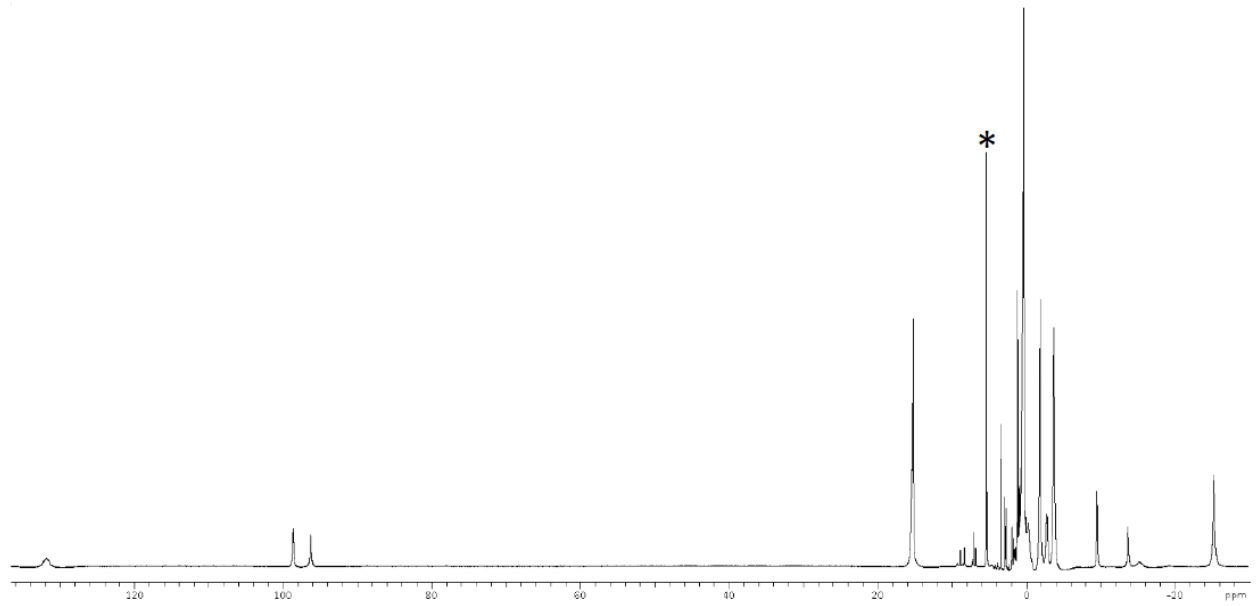

Figure S6. ^{1}H NMR of **8**, 500 MHz, CD_2Cl_2.

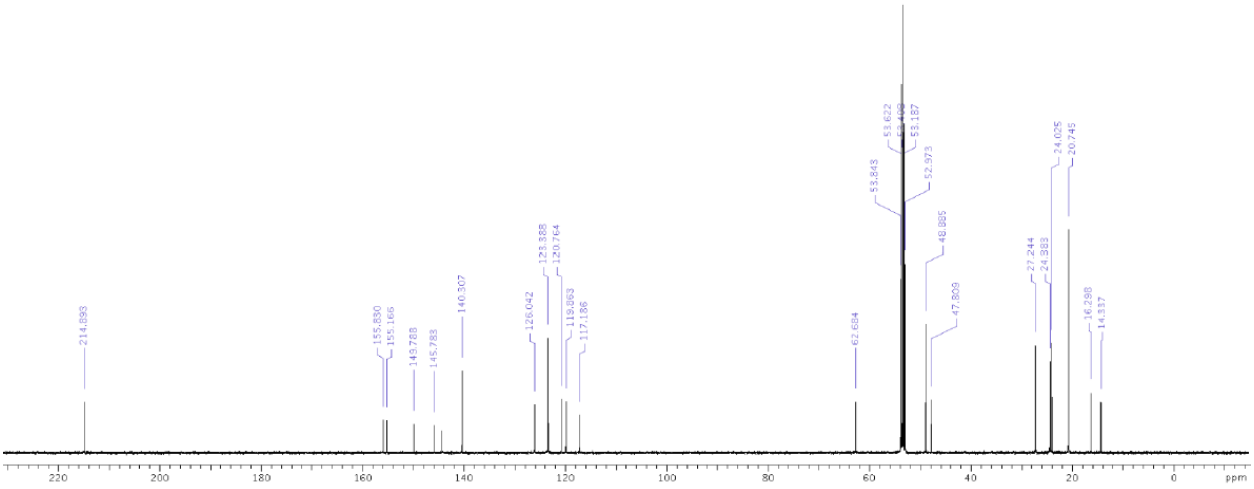

Figure S7. ^{13}C NMR of **9**, 500 MHz, CD_2Cl_2.

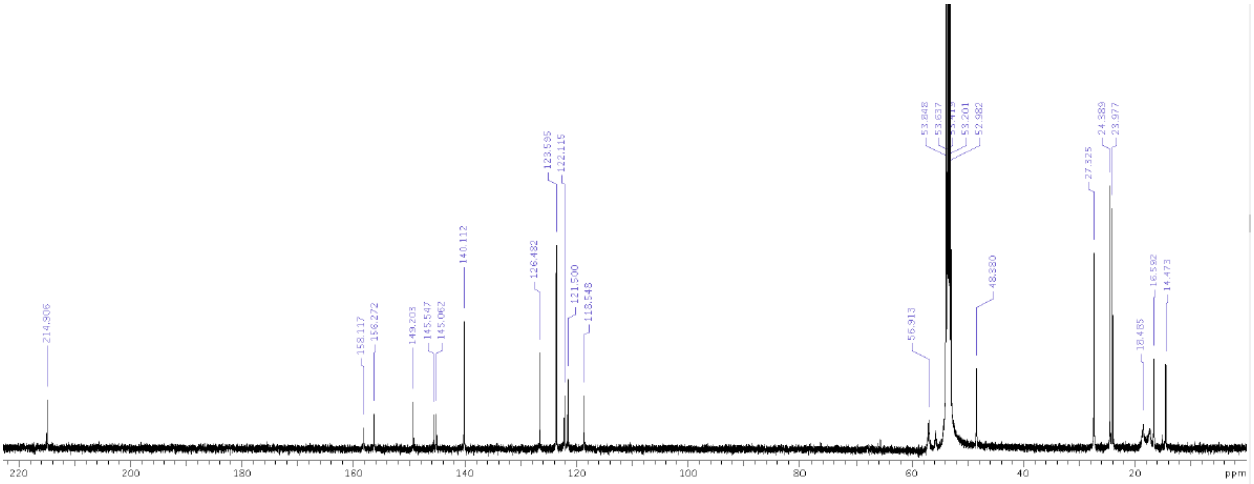

Figure S8. ^{13}C NMR of **9**, 500 MHz, CD_2Cl_2.

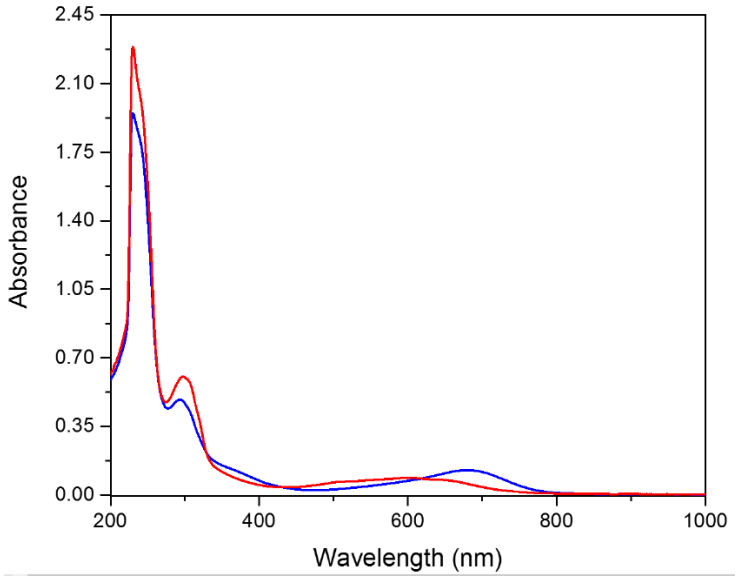

Figure S9. UV-visible spectra in CH_2Cl_2 of $Fe(didpa)Cl_2$ (**5**) (blue line, 7.125×10-5 M), and $[Fe(Hdidpa)Cl_2][PF_6]$ (**8**) (red line, 1.05×10-4 M).

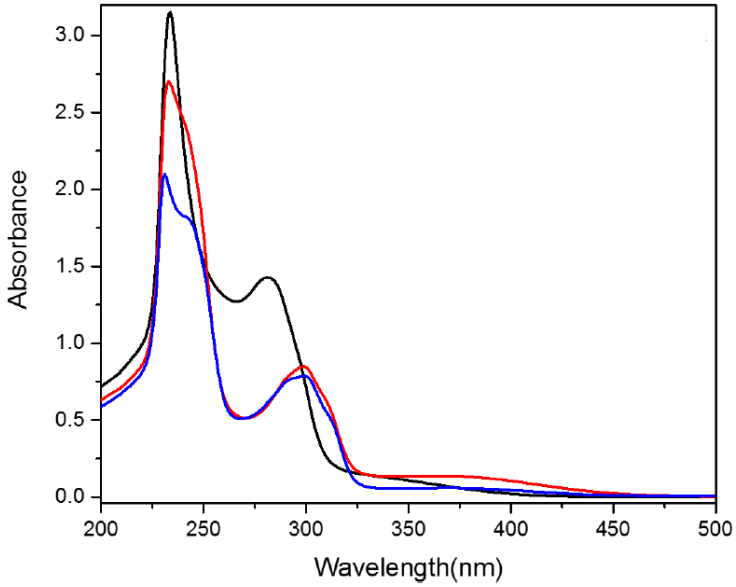

Figure S10. UV-visible spectra in CH_2Cl_2 of didpa (black line, 1.38×10-04 M), $Zn(didpa)Cl_2$ (**3**) (red line, 1.47×10-04 M), and $[Zn(Hdidpa)Cl_2][PF_6]$ (**6**) (blue line, 1.12×10-04 M).

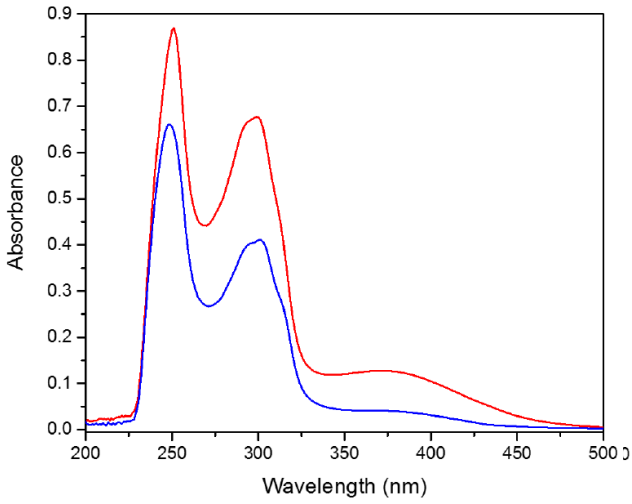

Figure S11. UV-visible spectra in CH_2Cl_2 of Zn(didpa)Br_2 (**4**) (red line, 1.28×10-04 M), and [Zn(Hdidpa)Br_2][PF_6] (**7**) (blue line, 8.54 ×10-05 M).

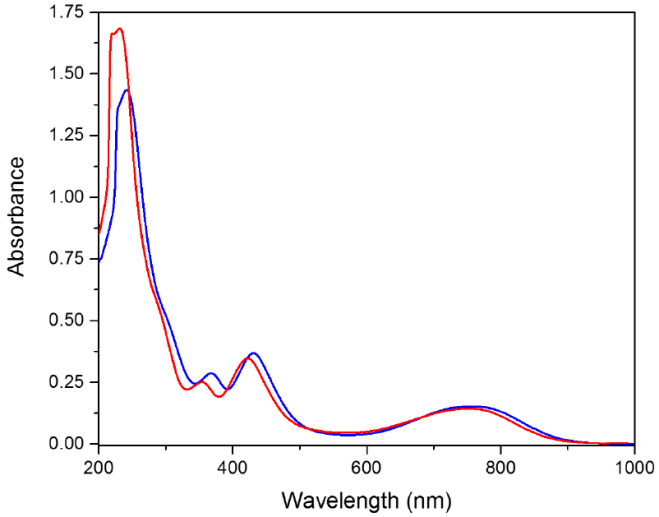

F**igure S12.** UV-visible spectra in CH_2Cl_2 of Fe(didpa)$(CO)_2$ (**9**) (blue line, 3.835×10-5 M), and [Fe(Hdidpa)$(CO)_2$][PF_6] (**10**) (red line, 5.595×10-5 M).

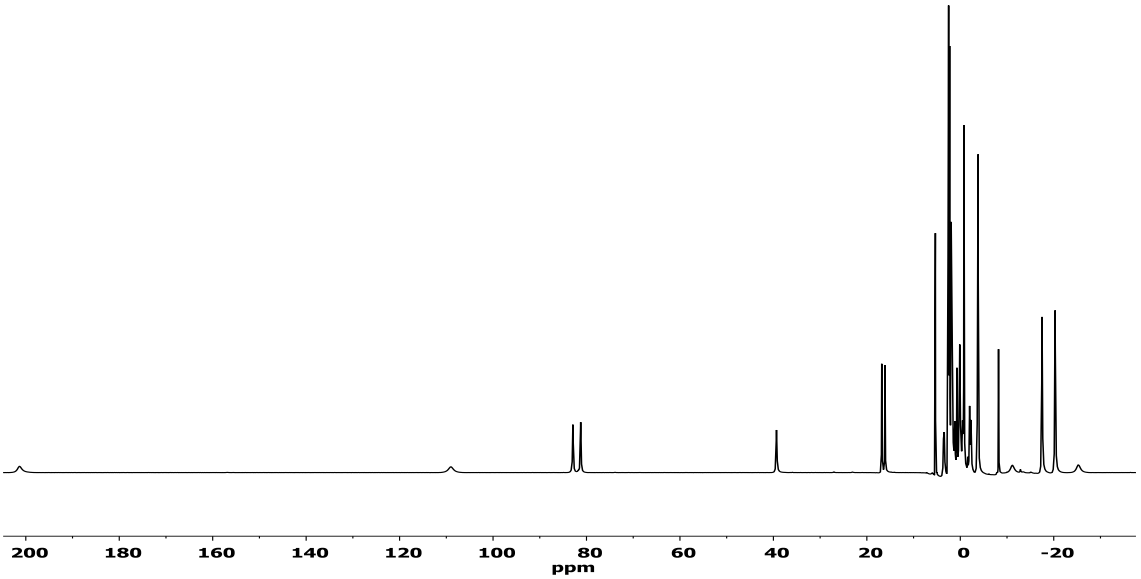

Figure S13. ^{1}H NMR of Fe(^{15c5}PDI)Cl_2 (**11**), 300 MHz, CD_2Cl_2.

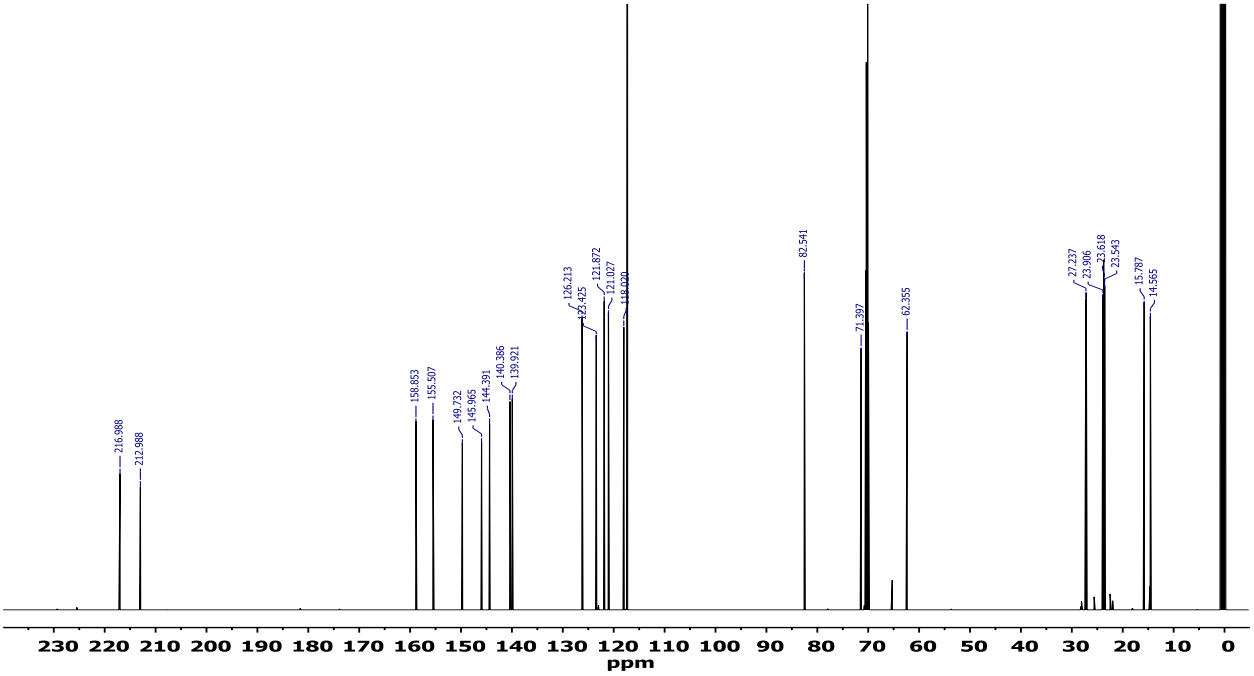

Figure S14. ^{13}C NMR of Fe(^{15c5}PDI)$(CO)_2$ (**12**) CD_3CN, 500 MHz, CD_2Cl_2.

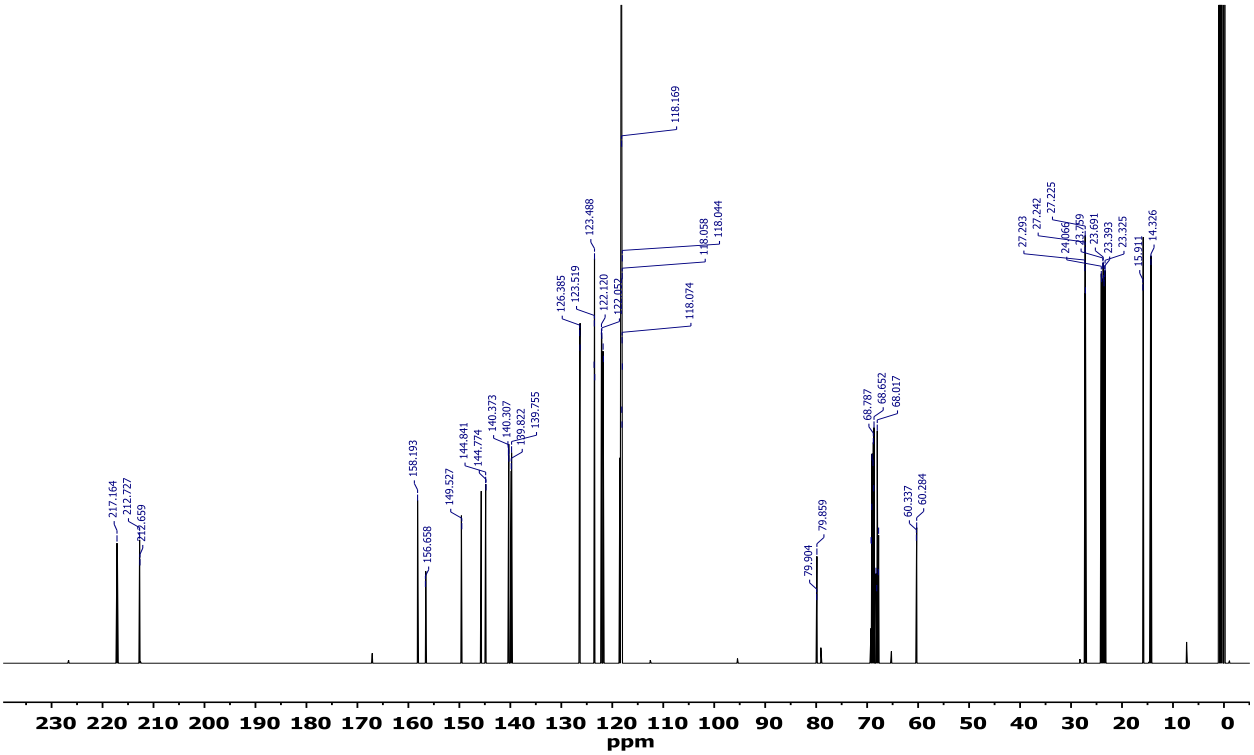

Figure S16. ^{13}C NMR of [Fe(^{15c5}PDI)(CO)$_2$ Li][PF$_6$] (**13**), 500 MHz, CD_3CN.

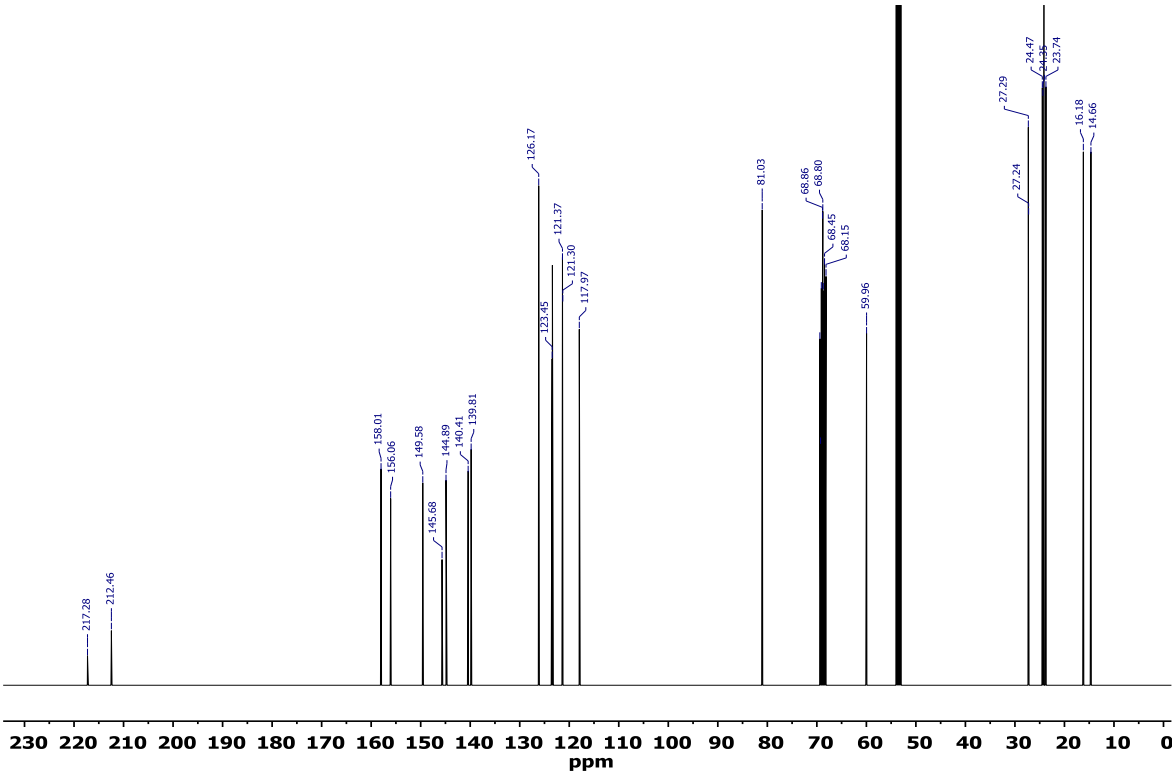

Figure S15. ^{13}C NMR of [Fe(^{15c5}PDI)(CO)$_2$ Na][PF$_6$] (**14**), 500 MHz, CD_2Cl_2.

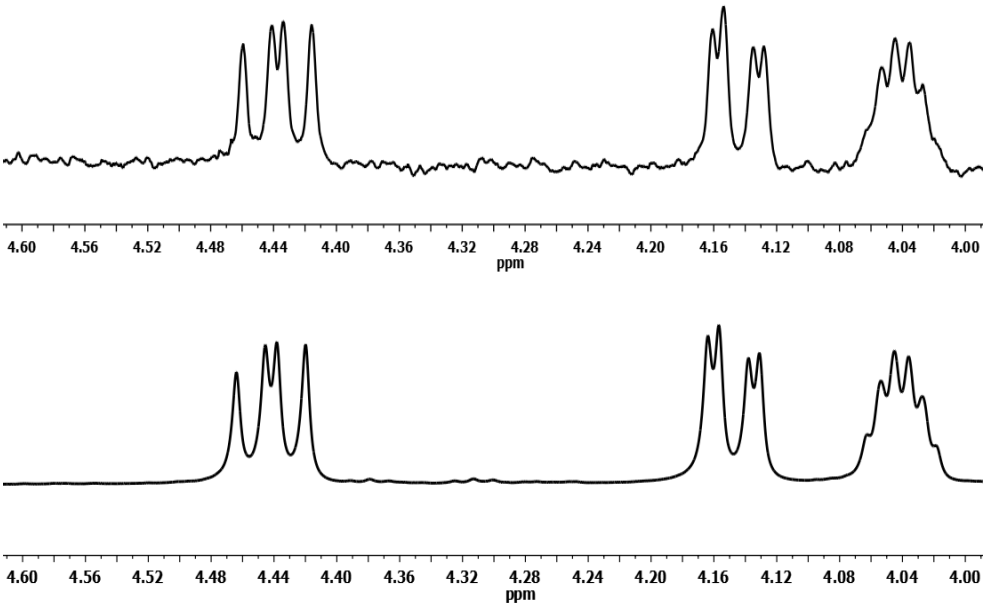

Figure S17. ^{1}H NMR spectrum of Fe(^{15c5}PDI)(CO)$_2$ [10 mM] +TBAP [1 M] (Top); Fe(^{15c5}PDI)(CO)$_2$ [40 mM](Bottom), CD_3CN.

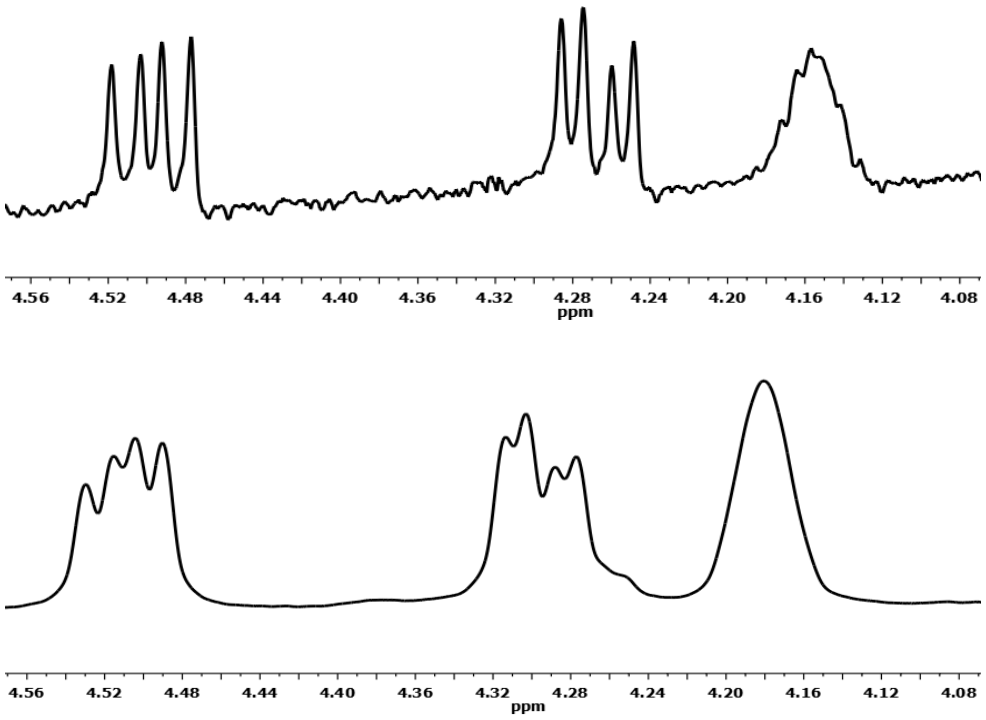

Figure S18. ^{1}H NMR of [Fe(^{15c5}PDI)(CO)$_2$ Na][PF_6] [10 mM] + TBAP [1 M] (Top); [Fe(^{15c5}PDI)(CO)$_2$ Na][PF_6][32 mM] (Bottom) in CD_3CN.

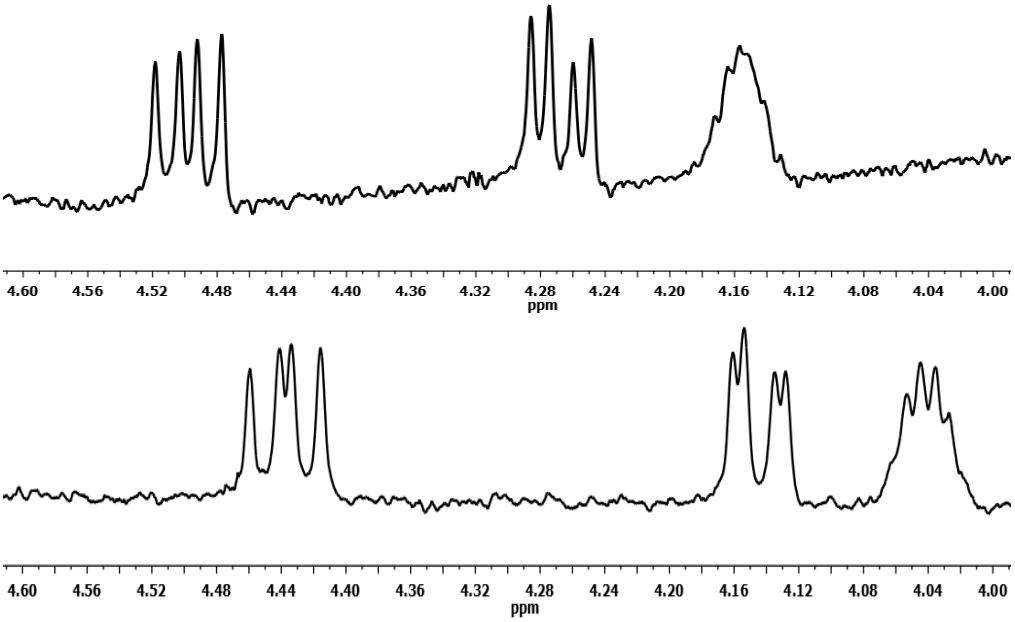

Figure S19. ^{1}H NMR of [Fe(^{15c5}PDI)(CO)$_2$ Na][PF$_6$] [10 mM]+ TBAP [1 M] (Top); Fe(^{15c5}PDI)(CO)$_2$ [10mM]+ TBAP [1 M] (Bottom) in CD_3CN.

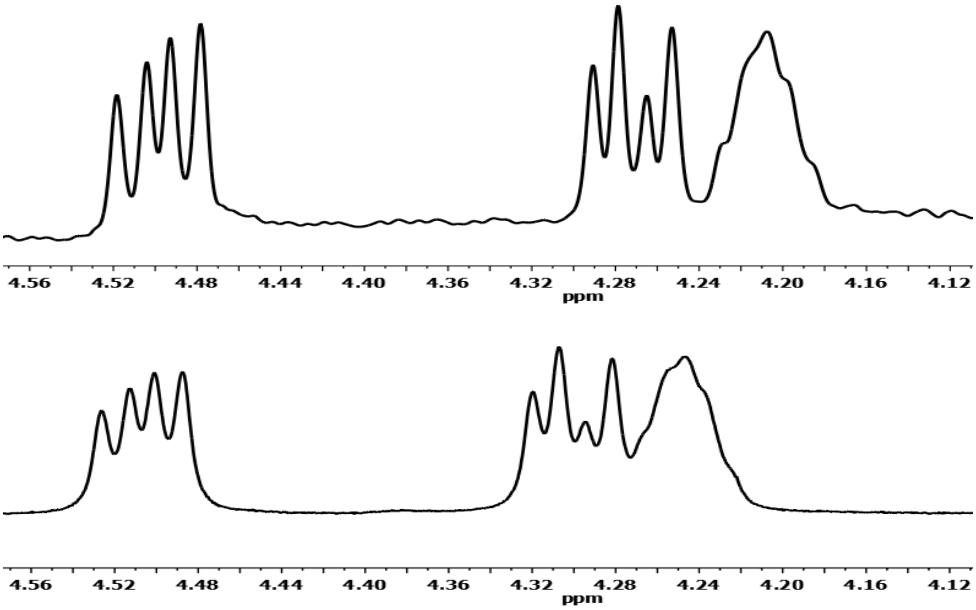

Figure S20. ^{1}H NMR of [Fe(^{15c5}PDI)(CO)$_2$ Li][PF$_6$] [10 mM]+ TBAP [1 M] (Top), [Fe(^{15c5}PDI)(CO)$_2$ Li][PF$_6$] [32 mM] [(Bottom), CD_3CN.

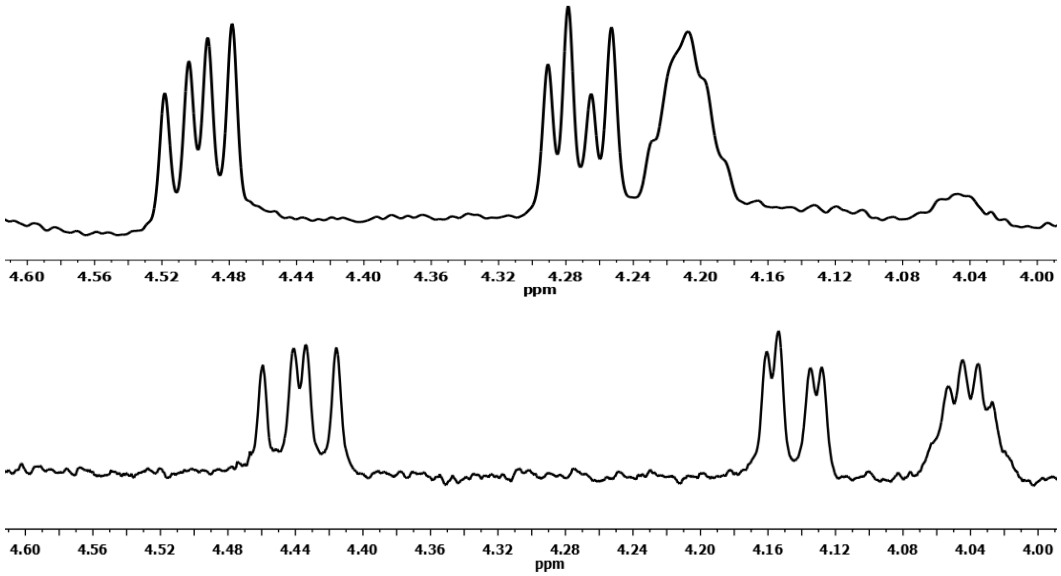

Figure S21. ^{1}H NMR of [Fe(^{15c5}PDI)(CO)$_2$Li][PF$_6$] [10 mM]+ TBAP [1 M] (Top), Fe(^{15c5}PDI)(CO)$_2$ [10 mM]+ TBAP [1 M] (Bottom), CD_3CN.

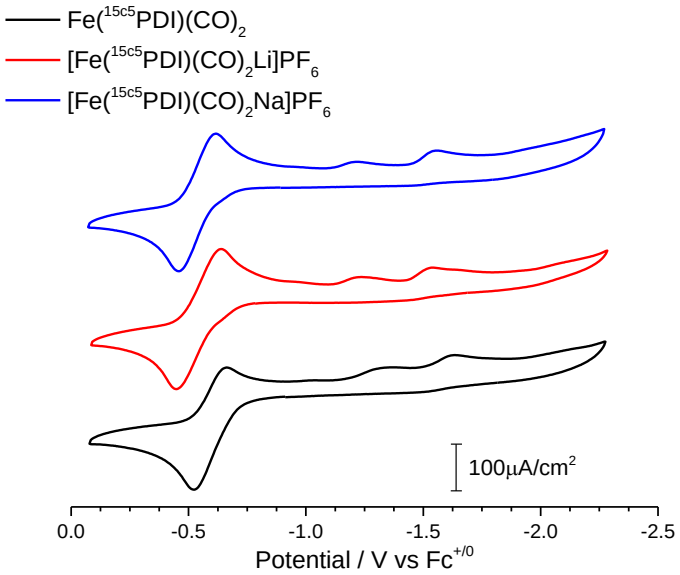

Figure S22. Cyclic Voltammograms of Fe(^{15c5}PDI)(CO)$_2$ (black), [Fe(^{15c5}PDI)(CO)$_2$Li][PF$_6$] (red), [Fe(^{15c5}PDI)(CO)$_2$Na][PF$_6$] (blue) in DCM.

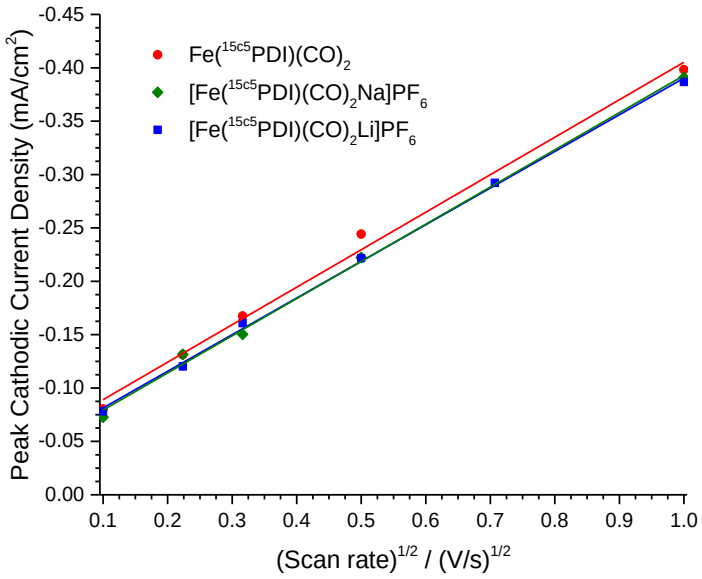

Figure S23. Plot of reductive event, $E_{cathodic}$ peak current versus square root of the scan rate for of $Fe(^{15c5}PDI)(CO)_2$ (**12**) (red), $[Fe(^{15c5}PDI)(CO)_2Li][PF_6]$ (**13**) (blue), $[Fe(^{15c5}PDI)(CO)_2Na][PF_6]$ (**14**) (green) in THF.

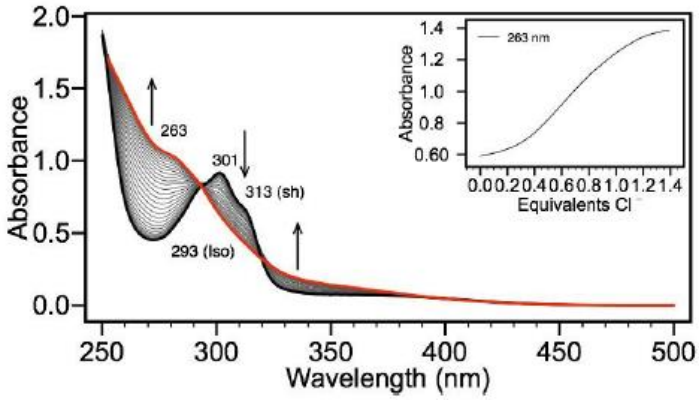

Figure S23. UV-Vis titration spectrum of **3** upon addition of NBu_4Cl in 0.1 equivalent increments up to 4 equivalents.

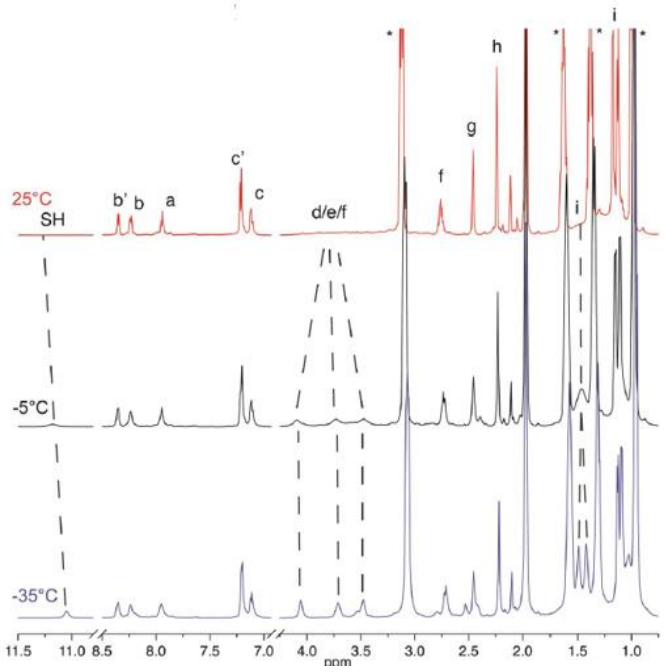

Figure S25. ^{1}H NMR spectra of 11.4 mM **3**, and 1.5 equiv. NBu_4SH in CD_3CN with varying temperatures.

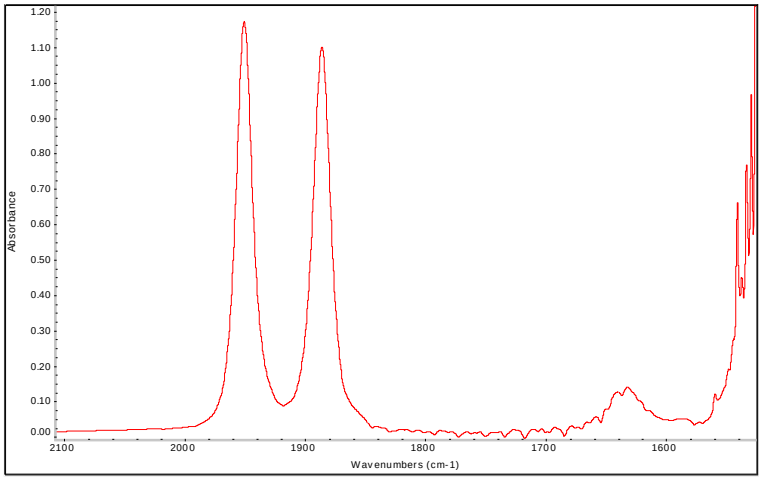

Figure S26. Liquid IR of reaction of complex **10** and $TBANO_3$ in THF at room temperature.

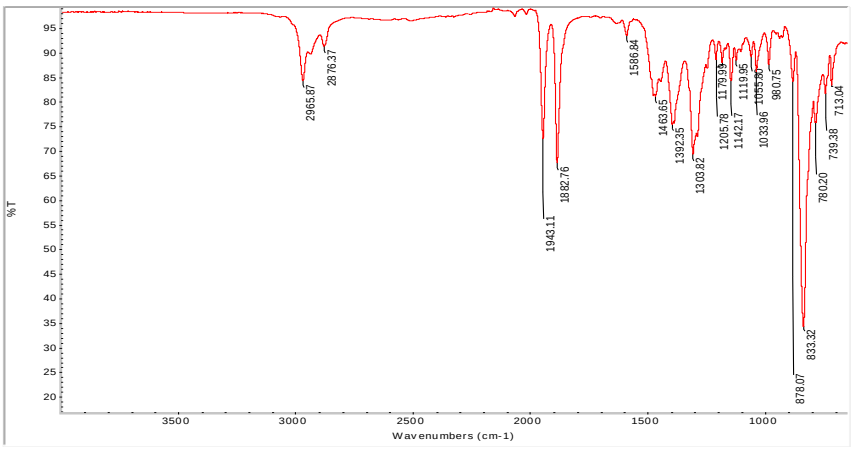

Figure S27. Solid-state FTIR spectrum of the reaction with complex **10** and $TBANO_3$ in THF at room temperature.

References

1. Drapier, J.; Hirling, H.; Wietzerbin, J.; Kaldy, P.; Kuhn, L.C.; *Embo Journal.* **1993**, 3643-3649.
2. Dawson, T. M.; Snyder, S. H. *J. Neuroscience.* **1994**, *14*, 5147-5159.
3. Foster, M.W.; Cowan, J.A. *J. Am. Chem. Soc.* **1999**, *121*, 4093-4100.
4. D. Reddy, J.R. Lancaster Jr., D.P. Cornforth, *Science*. **1983**, 769–770.
5. Filippov, G.; Bloch, D.B.; Bloch, K.D.; *J. Clin. Invest.* **1997**, 942-948.
6. Sanders, B.C.; Hassan, S.M.; Harrop, T.C. *J. Am. Chem. Soc.* **2014**, *136*, 10230-10233.
7. Meyer, F.; Tolman, W.B*. Inorg. Chem*. **2015**, *54*, 5039.
8. Taheri, A.; Berben, L. A. *Inorg. Chem*. **2016**, *55*, 378-385.
9. Taheri, A.; Berben, L. A. *Chem. Commun.* **2016**, *52*, 1768-1777.
10. Darensbourg, M. Y.; Llobet, A. *Inorg. Chem*. **2016**, *55*, 371-377.
11. Liu,K.; Lu, G.Q.; Yan, Z.; Beltramini. *Ind. Eng. Chem. Res.*, **2003**, *42*, 6518–6530.
12. Wang, S.; Lu, G.Q.; Millar, G.J. *Energy Fuels.* **1996,** *10,* 896-904.
13. Pakhare, D.; Spivey, J. *Chem. Soc. Rev.,* **2014**, *43*, 7813—7837.
14. Smith*, B. E. Science.* **2002**, *297*, 1654-1655.
15. Kandemir, K.; Schuster, M.E.; Behrens, M.; Schlogl, R. *Angew. Chem. Int. Ed*., **2013**, *52*, 12723–12726.
16. a) Valentine, A.M.; Lippard, S. J. *J. Chem. Soc*., *Dalton Trans*., **1997**, 3925–3931. b) Tolman, W.B. **2006**. Activation of small molecules: organometallic and bioinorganic perspectives. Wiley, New York.
17. Bertini, I. and Turano, P. **2008**. Inorganic Chemistry in Biology. Wiley Encyclopedia of Chemical Biology.
18. a) Mahon, B.P.; Pinard, M.A.; McKenna, R. *Molecules*. **2015**, *20*, 2323-2348.
19. Greco, C.; Fourmond, V.; Baffert, C.; Wang, P.; Dementin, S.; Bertrand, P.; Bruschi, M.; Blumberger, J.; Gioia, L.; Leger, C. *Energy Environ. Sci.,* **2014**, *7*, 3543–3573.
20. Ozaki, S.; Matsui, T.; Roach, M. P.; Watanabe, Y. *Coord. Chem. Rev.* **1999**, *198*, 39-59.
21. MacBeth, C.E.; Hammes, B.S.; Young Jr.; V.G.; Borovik, A.S. In*org. Chem.*, **2001**, *40*, 4733–4741.
22. a) Rios-Gonzalez, B.B.; Roman-Morales, E.M.; Pietri, R.; Lopez-Garriga, J. *J. Inorg. Biochem*. **2014**, *133*, 78–86. b) Banerjee, R.; Kabil, O. *J. Biol. Chem.* **2010**, *285*, 21903–21907. c) Galardon, E.; Roger, T.; Deschamps, P.; Roussel, P.; Tomas, A.; Artaud, I. *Inorg. Chem.* **2012**, *51*, 10068.
23. Nagy, P.; Pálinkás, Z.; Nagy, A.; Budai, B.; Tóth, I.; Vasa, A.. *Biochim. Biophys. Acta*. **2014**, *1840*, 876–891.
24. Snyder, S. H.; Dawson, T.M. J. *Neurosci*. **1994**, *9*, 5147-5159.
25. Wang, R. *Physiol Rev.* **2012**, *92*, 791–896.
26. Vahrenkamp, H. *Angew. Chem. Int. Ed.* **1975**, *14*, 322-329.
27. a) Rombah, M.; Vahrenkamp, H. *Inorg. Chem*., **2001**, *40*, 6144–6150. b) Ruf, M.; Vahrenkamp, H. *Inorg. Chem.*, **1996**, *35*, 6571–6578.
28. Fernandez-Alberti, S.; Bacelo, D.E.; Binning Jr., R.C.; Echave, J.; Chergui, M. Lopez-Garriga, J. *Biophys. J.* **2006**, *91*, 1698–1709.
29. Pietri, R.; Lewis, A.; León, R.G.; Casabona,G.; Kiger,L.; Yeh, S.; Fernandez-Alberti,S.; Marden, M.C.; Cadilla, C.L.; López-Garriga. *J. Biochem*. **2009**, *48*, 4881–4894.
30. a)Poole, R.K. *Biochem. Soc. Trans.* **2005**, *33*, 176. b) Butler, C.S.; Richardson, D.J. *Biochem. Soc. Trans.* **2005**, *33*, 113-118.

31. Leopoldini, M.; Russo, N.; Toscano, M.; Dulak, M.; Wesolowski, T. A. *Chem. Eur. J*. **2006**, *12*, 2532-2541.
32. a) Sparacino-Watkins, C.; Stolz, J.F.; Basu, P. *Chem. Soc. Rev.,* **2014**, *43*, 676-706. b) Stolz, J. F.; P. Basu. *Chembiochem,* **2002**, *3*, 198–206.
33. a) Averill, B. A. *Chem. Rev.*, **1996**, *96*, 2951–2964.
34. Moncada, S.; Higgs, E. A. B*r. J. Pharmacol.,* **2006,** *147*, 193-201.
35. Cutruzzola, F.; Brown, K.; Wilson, E.K.; Bellelli, A.; Arese, M.; Tegoni, M.; Camillau, C.; Brunori, M. Proc. Natl. Acad. Sci. **2001**, *98*, 2232-2237.
36. Barber, J. *Nat. Plants.* **2017**, *3*, 17041. b) Young, I.D., et. al. *Nature.* **2016**, *540*, 453-457. c) Zhang, C.; Chen, C.; Dong, H.; Shen, J.; Dau, H.; Zhao, J. *Science*. **2015**, *348*, 690-693. d) McEvoy, J.P.; Brudvig, G.W*.; Chem. Rev.,* **2006**, *106*, 4456-4478. e) Satadal, P.; Neese, F.; Pantazis, D. A.; *Green Chem.,* **2017**, *19*, 2309-2325.
37. a) Herbert, D. E. ; Lionetti, D.; Jonathan Rittle; Agapie, T. *J. Am. Chem. Soc.* **2013,** *135*, 19075-19078. b) Tsui, E. Y.; Tran, R.;Yano, J.; Agapie, T. *Nat. Chem*. **2013**, *5*, 293.
38. a) Shook, R. L.; Borovik, A. S. *Inorg. Chem.*, **2010**, *49*, 3646–3660. b) Moore, C. M.; Szymczak, N. K. *Dalton Trans.* **2012**, *41*, 7886-7889. c) Matson, E. M.; Bertke, J. A.; Fout, A. R. I*norg. Chem.*, **2014**, *53*, 4450–4458.
39. Kendall, A.J., Zakharov, L.N., Gilbertson, J.D*. Inorg. Chem.* **2010**, *49*, 8656–8658.
40. Bart, S. C.; Lobkovsky, E.; Bill, E.; Wieghardt, K.; Chirik, P. J. *Inorg. Chem.*, **2007**, *46*, 7055–7063.
41. a) Borovik, A. S. *Acc. Chem. Res.* **2005,** *38*, 54-61. b) Backes et al. *J. Am. Chem. Soc.,* **1991**, *113*, 2055-2064. c) Garner, D. K.; Fitch, S. B.; McAlexander, L. H.; Bezold, L. M.; Arif, A. M.; Berreau, L. M. *J. Am. Chem. Soc*. **2002**, *124*, 9970−9971. d) Thorp, H.H. *Chem. Biol.* **1996**, *5*, 125. e) R. H. Holm, P. Kennepohl and E. I. Solomon, *Chem. Rev.*, **1996**, *96*, 2239–2314. f) Schlichting, I.; Berendzen, J.; Chu, K.; Stock, A. M.; Maves, S. A.; Benson, D. E.; Sweet, ; Ringe, R. M. D.; Petsko, G. A.; Sligar, S. G. *Science*, **2000**, *287*, 1615–1622.
42. Cook, S.A.; Hill, E.A.; Borovik, A.S. *Biochemistry.* **2015**, *54*, 4167−4180.
43. Greeves, N. ChemTube3D. **2008-2017**, The University of Liverpool (accessed Jun 11, 2017).
44. Sickerman, N.S.; Park, Y.J.; Ng, G. K.; Bates, J.E.; Hilkert, M.; Ziller, J.W.; Furche, F.; Borovik, A.S. *Dalton Trans.* **2012**, *41*, 4358-4364.
45. Shook, R. L.; Borovik, A.S. *Chem. Commun.* **2008**, 6095–6107. Lucas, R.L.; Zart, M.K.; Murkerjee, J.; Sorrell, T.N.; Powell, D.R.; Borovik, A.S. *J. Am. Chem. Soc.* **2006**, *128,* 15476.
46. Mareque Rivas, J. C.; Hinchley, S. L.; Metteau, L.; Parsons, S., *Dalton Trans.* **2006**, 2316–2322.
47. Liu, C.T.; Chu. J.F.; Lin, C. K.; Hong, C.W. *Phys. Chem. Chem. Phys*., **2017**, *19*, 8300-8306.
48. Jacobsen, G. M.; Yang, J.Y.; Twamley, B.; Wilson, A.D.; Bullock, R.M.; DuBois, M.R.; DuBois, D.L. *Energy Environ. Sci.*, **2008**, *1*, 167-174.
49. Wu, A.; Masland, J.; Swartz, R.D.; Kaminsky, W.; Mayer, J.W. *Inorg. Chem.*, **2007**, *46*, 11190–11201.
50. M.R. DuBois, D.L. DuBois. *C. R. Chimie*, **2011**, *11*, 805-817.
51. Mareque Rivas, J. C.; Hinchley, S. L.; Metteau, L.; Parsons, S., *Dalton Trans*. **2006**, 2316–2322.
52. Brammer, L.; Bruton, E. A.; Sherwood, P. *Cryst. Growth Des*. **2001**, *1*, 277−290.
53. Warren, J.J.; Mayer, J.M. *J. Am. Chem. Soc***. 2008**, *130*, 2774-2776.
54. Borovik, A. S. *Acc. Chem. Res*. **2005**, *38*, 54−61.
55. DuBois, D. L.; Bullock, R. M. *Eur. J. Inorg. Chem*. **2011**, *7*, 1017−1027.

56. Tondreau, A. M.; Milsmann, C.; Lobkovsky, E.; Chirik, P. *J.Inorg. Chem*. **2011**, *50*, 9888−9895.
57. Thammavongsy, Z.; Seda, T.; Zakharov, L. N.; Kaminsky, W.; Gilbertson, J. D. *Inorg. Chem*. **2012**, *51*, 9168-9170.
58. Thammavongsy, Z.; LeDoux, M. E.; Breuhaus-Alvarez, A. G.; Seda, T.; Gilbertson, J. D. *Eur. J. Inorg. Chem*. **2013**, *22*, 4008−4015.
59. Addison, A.W.; Rao, T. N.; Rijn, J.; Verschoor, G.C. *J. Chem. Soc. Dalton Trans.*, **1984**, 1349-1356.
60. Sur, S. K. *J. Mag. Res*. **1988**, *82*, 169-173.
61. Bart, S. C.; Chlopek, K.; Bill, E.; Bouwkamp, M. W.; Lobkovsky, E.; Neese, F.; Wieghardt, K.; Chirik, P. J. *J. Am. Chem. Soc*. **2006**, *128*, 13901−13912.
62. Enright, D.; Gambarotta, S.; Yap, G. P. A.; Budzelaar, P. H. M. *Angew. Chem., Int. Ed.,* **2002**, *41*, 3873−3876.
63. Britovsek, G. J.; Clentsmith, G. K. B.; Gibson, V. C.; Goodgame, D. M. L.; McTavish, S. J.; Pankhurst, Q. A. *Catal. Commun.* **2002**, *3*, 207−211.
64. Small, B. L.; Brookhart, M.; Bennett, A. M. A. *J. Am. Chem. Soc.* **1998**, *120*, 4049−4050.
65. Delgado, M.; Sommer, S. K.; Swanson, S.P.; Berger, R. F.; Seda, T.; Zakharov, L. N.; Gilbertson, J. D. *Inorg. Chem.*, **2015**, *54*, 7239–7248.
66. Stieber, S.C.E.; Milsmann, C.; Hoyt, J. M.; Turner, Z. R.; Finkelstein, K. D.; Wieghardt, DeBeer, S.; Chirik, P. J. *Inorg. Chem*. **2012**, *51*, 3770−3785.
67. Steiner, T. *Angew. Chem., Int. Ed*. **2002**, *41*, 48−76.
68. Warren, J. J.; Tronic, T. A.; Mayer, J. M. *Chem. Rev.* **2010**, *110*, 6961-7001.
69. Weinberg, D. R.; Gagliardi, C. J.; Hull, J. F.; Murphy, C. F.; Kent, C. A.; Westlake, B. C.; Paul, A.; McCafferty, D. G.; Meyer, T. J. *Chem. Rev.* **2012**, *112*, 4016-4093.
70. a) Teets, T. S.; Labinger, J. A.; Bercaw, J. E. *Organometallics.* **2013**, *32*, 5530-5545. b) Karlin, K.D. *Science*, **1993**, *261*, 701-708.
71. Rivas, J. C. M.; Rosales, R. T. M.; Parsons, S. *Dalton Trans.* **2003***, 11*, 2156-2163*.*
72. Rivas, J. C. M.; Salvagni, E.; Rosales, R. T. M.; Parsons, S. *Dalton Trans.* **2003**, *17*, 3339-3349.
73. Berreau, L. M.; Makowska-Grzyska, M. M.; Arif, A. M. *Inorg. Chem.* **2001**, *40*, 2212-2213.
74. Kamlet, M. J.; Taft, R. W. *J. Am. Chem. Soc*. **1976**, *98*, 377-383.
75. Marcus, Y. *Chem. Soc. Rev.* **1993**, *22*, 409-416.
76. Hartle, M.D.; Delgado, M.; Gilbertson, J.D.; Pluth, M.D. *Chem. Commun.*, **2016**, *52*, 7680-7682.
77. Park, Y.J.; Ziller, J.W.; Borovik, A.S. *J. Am. Chem. Soc.* **2011**, *133*, 9258–9261. b) Choe, C., Yang, L., Lv, Z., Mo, W., Chem, Z., Li, G., Yin, G., *Dalton Trans.,* **2015**, *44*, 9182-9192. c) Morimoto, Y.; Kotani, H.; Park, J.; Lee, Y. M.; Nam, W.; Fukuzumi, S. *J. Am. Chem. Soc*. **2011**, *133*, 403.
78. Siegbahn, P. E. & Crabtree, R. H. *J. Am. Chem. Soc*. **1999**, *121*, 117–127.
79. Lin, P.; Takase, M.K.; Agapie, T. *Inorg. Chem.*, **2015**, *54*, 59–64.
80. Risch, M; Klingan, K.; Ringleb, F.; Chernev, P.; Zaharieva, I.; Fischer, A.; Dau, H. *ChemSusChem*. **2012**, *5*, 542 – 549 .
81. Kanan, M.W.; Nocera, D. G. *Science.* **2008**, *321*, 1072-1075.
82. Wiechen, M.; Zaharieva, I.; Dau, H.; Kurz, P. *Chem. Sci.*, **2012**, *3*, 2330-2339.
83. Kanan, M.W.; Yano, J.; Surendranath, Y.; Dinca, M.; Yachandra, V.K.; Nocera, D.G. *J. Am. Chem. Soc.*, **2010**, *132*, 13692–13701.
84. Park, Y.J.; Cook. S.A.; Sickerman, N.S.; Sano. Y.; Ziller, J.W.; Borovik, A.S. *Chem. Sci.* **2013**, *4*, 717.

85. Lee, Y.M; Bang, S.; Kim,Y.M.; Cho, J.; Hong, S.; Nomura, T.; Ogura, T.; Troppner, O.; Burmazovic, I.; Sarangi, R.; Fukuzumi, S.; Nam, W.*Chem. Sci.* **2013**, *4*, 3917-3923.
86. Kita, M.R.; Miller, A.J. *J.Am.Soc.* **2014**, *136*, 14519-14529.
87. (a) Miller, C. G.; Wylie, S.W.; Horwitz, C.P.; Strazisar, S.A.; Peraino, D.K.; Clark, G.R.; Weintraub, S.T.; Collins, T.J. *J. Am. Chem. Soc.*, **1998**, *120*, 11540–11541. (b) Leeladee, P.; Baglia, R.A.; Prokop, K.A.; Latifi, R.; Visser, S.P.; Goldberg, D.P. *J. Am. Chem. Soc.*, **2012**, *134*, 10397–10400.
88. Yiu S-M, Man W-L, Lau T-C. *J. Am. Chem. Soc.* **2008**, *130*, 10821–10827.
89. Cook, S.A.; Ziller, J.W.; Borovik, A.S. *Inorg. Chem*. **2014**, *53*, 11029−11035.
90. Grajeda, J.; Kita, M.R.; Gregor, L. C.; White, P. S.; Miller, A. J. M. *Organometallics*, **2016**, *35*, 306–316.
91. Delgado, M.; Ziegler, J.M.; Seda, T.; Zakharov, L.N.; Gilbertson, J.D. *Inorg. Chem.*, **2016**, *55*, 555.
92. a) Bart, S. C.; Chlopek, K.; Bill, E.; Bouwkamp, M. W.; Lobkovsky, E.; Neese, F.; Wieghardt, K.; Chirik, P.J. *J. Am. Chem. Soc.*, **2006**, *128*, 13901–13912. b) Wan, Y.; Hancock, F. E.; Hutchings, G. J. *Catal. Comm*. **2002**, *3*, 145-148.
93. Addison, A. W.; Rao, T. N.; Reedijk, J.; Rijn, J.; Verschoor, G. C. *J. Chem. Soc., Dalton Trans.* **1984**, 1349.
94. (a) Gordon, Z., Drummond, M.J., Matson, E. M., Bogart, J. A., Schelter, E.J., Lord, R.L., Fout, A. R. *Inorg. Chem.*, **2017**, *56*, 4852–4863. (b) Shook, R. L.; Borovik, A.S. *Inorg. Chem.* **2010**, 49, 3646-3660. (c) Hosseinzadeh, P.; Lu, Y. *Biochimica et Biophysica Acta*. **2016**, *1857*, 557–581.
95. Darmon, J. M.; Turner, Z. R.; Lobkovsky, E.; Chirik, P. J. *Organometallics*. **2012**, *31*, 2275-2285.
96. Cotton, F. A. *Progress in Inorganic Chemistry*, John Wiley & Sons, Inc. **2009**, *7*, 277-351.
97. Tingerg, C.E.; Tonzetich, Z.J.; Wang, H.; Do, L.H.; Yoda, Y.; Cramer, S.P.; Lippard, S. J. *J. Am. Chem. Soc*. **2010**, *132*, 18168–18176.
98. Tran, N. G.; Kalyvas, H.; Skodje, K. M.; Hayashi, T.; Moenne-Loccoz, P.; Callan, P. E.; Shearer, J.; Kirschenbaum, L.J.; Kim, E. *J. Am Chem Soc*. **2011**, *133*, 1184–1187.
99. Yi, J.; Thomas, L. M.; Richter-Addo, G. B.; *Angew*. Chem. **2012**, *124*, 3685 –3687.
100. Enemark, J. H.; Feltham, R. D. *Coord. Chem. Rev.* **1974**, *13*, 339-406.
101. Vanysek, P. In *CRC Handbook of Chemistry and Physics*, 87th ed.; Lide, D. R., Ed.; CRC Press: Boca Raton, FL, **2006.**
102. (a) Britovesk, G. J. P.; Bruce, M.; Gibson, V. C.; Kimberly, B. S.; Maddox, P.J.; Mastoianni, S.; McTavish, S. J.; Redshaw, c.; Solan, G. A.; Stromberg, S.; White, A. J. P.; Williams, D.J. *J. Am. Chem. Soc.*,**1999**, *121*, 8728–8740. (b) Kwon, Y. M.; Delgado, M.; Zakharov, L. N.; Seda, T.; Gilbertson, J. D. *Chem. Commun.*, **2016**, *52*, 11016-11019.
103. Shih, W.; Lu, T.; Tsai, F.; Chiang, M.; Lee, J.; Chiang, Y.; Liaw, W. *J. Inorg. Biochem,* **2012**, 113, 83–93, (b) Speelman, A. L.; Zhang, B.; Silakov, A.; Skodje, K. M.; Alp, E. E.; Zhao, J.; Hu, M. Y.; Kim, E.; Krebs, C.; Lehnert, N. *Inorg. Chem*., **2016**, *55*, 5485–5501.
104. Hess, J.L.; Hsieh, C.; Reibenspies, J. H.; Darensbourg, M. Y. *Inorg. Chem.,* **2011**, *50*, 8541–8552.
105. G. A. Bain and J. F. Berry, *J. Chem. Educ.,* **2008**, *85*, 532– 536.
106. Perdew, J. P.; Burke, K.; Ernzerhof, M. *Phys. Rev. Lett.* **1996**, *77*, 3865– 3868.
107. Kresse, G.; Furthmüller, J. *Phys. Rev. B: Condens. Matter Mater. Phys.* **1996**, *54*, 11169– 11186.
108. Kresse, G.; Joubert, D. *Phys. Rev. B: Condens. Matter Mater. Phys.* **1999**, *59*, 1758– 1775.
109. Ireta, J.; Neugebauer, J.; Scheffler, M. *J. Phys. Chem. A* **2004**, *108*, 5692– 5698.

110. Makov, G.; Payne, M. C. *Phys. Rev. B: Condens. Matter Mater. Phys.* **1995**, *51*, 4014– 4022.
111. Sheldrick, G. M. *Bruker/Siemens Area Detector Absorption Correction Program*; Bruker AXS: Madison, WI, **1998**.
112. SHELXTL-6.10, Program for Structure Solution, Refinement and Presentation; BRUKER AXS Inc.:Madison, WI.